https://doi.org/10.3847/1538-4365/abc6a1

The NANOGrav 12.5 yr Data Set: Wideband Timing of 47 Millisecond Pulsars

Md F. Alam[1], Zaven Arzoumanian[2], Paul T. Baker[3], Harsha Blumer[4,5], Keith E. Bohler[6], Adam Brazier[7], Paul R. Brook[4,5], Sarah Burke-Spolaor[4,5], Keeisi Caballero[6], Richard S. Camuccio[6], Rachel L. Chamberlain[1], Shami Chatterjee[7], James M. Cordes[7], Neil J. Cornish[8], Fronefield Crawford[1], H. Thankful Cromartie[7], Megan E. DeCesar[9,10,40], Paul B. Demorest[11], Timothy Dolch[12], Justin A. Ellis[13], Robert D. Ferdman[14], Elizabeth C. Ferrara[15], William Fiore[4,5,16], Emmanuel Fonseca[17], Yhamil Garcia[6], Nathan Garver-Daniels[4,5], Peter A. Gentile[4,5], Deborah C. Good[18], Jordan A. Gusdorff[9], Daniel Halmrast[12,19], Jeffrey S. Hazboun[20], Kristina Islo[16], Ross J. Jennings[7], Cody Jessup[8,12], Megan L. Jones[16], Andrew R. Kaiser[4,5], David L. Kaplan[16], Luke Zoltan Kelley[21], Joey Shapiro Key[20], Michael T. Lam[22,23], T. Joseph W. Lazio[24], Duncan R. Lorimer[4,5], Jing Luo[25], Ryan S. Lynch[26], Dustin R. Madison[4,5,41], Kaleb Maraccini[16], Maura A. McLaughlin[4,5], Chiara M. F. Mingarelli[27,28], Cherry Ng[29], Benjamin M. X. Nguyen[1], David J. Nice[9], Timothy T. Pennucci[30,31,41], Nihan S. Pol[4,5], Joshua Ramette[12,32], Scott M. Ransom[30], Paul S. Ray[33], Brent J. Shapiro-Albert[4,5], Xavier Siemens[16,34], Joseph Simon[24], Renée Spiewak[35], Ingrid H. Stairs[18], Daniel R. Stinebring[36], Kevin Stovall[11], Joseph K. Swiggum[9,41], Stephen R. Taylor[37], Michael Tripepi[12,38], Michele Vallisneri[24], Sarah J. Vigeland[16], Caitlin A. Witt[4,5], and Weiwei Zhu[39]

The NANOGrav Collaboration

[1] Department of Physics and Astronomy, Franklin & Marshall College, P.O. Box 3003, Lancaster, PA 17604, USA
[2] X-Ray Astrophysics Laboratory, NASA Goddard Space Flight Center, Code 662, Greenbelt, MD 20771, USA
[3] Department of Physics and Astronomy, Widener University, One University Place, Chester, PA 19013, USA
[4] Department of Physics and Astronomy, West Virginia University, P.O. Box 6315, Morgantown, WV 26506, USA
[5] Center for Gravitational Waves and Cosmology, West Virginia University, Chestnut Ridge Research Building, Morgantown, WV 26505, USA
[6] Center for Advanced Radio Astronomy, University of Texas-Rio Grande Valley, Brownsville, TX 78520, USA
[7] Cornell Center for Astrophysics and Planetary Science and Department of Astronomy, Cornell University, Ithaca, NY 14853, USA
[8] Department of Physics, Montana State University, Bozeman, MT 59717, USA
[9] Department of Physics, Lafayette College, Easton, PA 18042, USA
[10] George Mason University, Fairfax, VA 22030, USA
[11] National Radio Astronomy Observatory, 1003 Lopezville Road, Socorro, NM 87801, USA
[12] Department of Physics, Hillsdale College, 33 E. College Street, Hillsdale, MI 49242, USA
[13] Infinia ML, 202 Rigsbee Avenue, Durham, NC 27701, USA
[14] School of Chemistry, University of East Anglia, Norwich, NR4 7TJ, UK
[15] NASA Goddard Space Flight Center, Greenbelt, MD 20771, USA
[16] Center for Gravitation, Cosmology and Astrophysics, Department of Physics, University of Wisconsin-Milwaukee, P.O. Box 413, Milwaukee, WI 53201, USA
[17] Department of Physics, McGill University, 3600 University Street, Montreal, QC H3A 2T8, Canada
[18] Department of Physics and Astronomy, University of British Columbia, 6224 Agricultural Road, Vancouver, BC V6T 1Z1, Canada
[19] Department of Mathematics, University of California, Santa Barbara, CA 93106, USA
[20] University of Washington Bothell, 18115 Campus Way NE, Bothell, WA 98011, USA
[21] Center for Interdisciplinary Exploration and Research in Astrophysics (CIERA), Northwestern University, Evanston, IL 60208, USA
[22] School of Physics and Astronomy, Rochester Institute of Technology, Rochester, NY 14623, USA
[23] Laboratory for Multiwavelength Astrophysics, Rochester Institute of Technology, Rochester, NY 14623, USA
[24] Jet Propulsion Laboratory, California Institute of Technology, 4800 Oak Grove Drive, Pasadena, CA 91109, USA
[25] Department of Astronomy & Astrophysics, University of Toronto, 50 St. George Street, Toronto, ON M5S 3H4, Canada
[26] Green Bank Observatory, P.O. Box 2, Green Bank, WV 24944, USA
[27] Center for Computational Astrophysics, Flatiron Institute, 162 5th Avenue, New York, NY 10010, USA
[28] Department of Physics, University of Connecticut, 196 Auditorium Road, U-3046, Storrs, CT 06269-3046, USA
[29] Dunlap Institute for Astronomy and Astrophysics, University of Toronto, 50 St. George Street, Toronto, ON M5S 3H4, Canada
[30] National Radio Astronomy Observatory, 520 Edgemont Road, Charlottesville, VA 22903, USA; tim.pennucci@nanograv.org
[31] Institute of Physics, Eötvös Loránd University, Pázmány P.s. 1/A, 1117 Budapest, Hungary
[32] Department of Physics, Massachusetts Institute of Technology, 77 Massachusetts Avenue, Cambridge, MA 02139-4307, USA
[33] Space Science Division, Naval Research Laboratory, Washington, DC 20375-5352, USA
[34] Department of Physics, Oregon State University, Corvallis, OR 97331, USA
[35] Centre for Astrophysics and Supercomputing, Swinburne University of Technology, P.O. Box 218, Hawthorn, Victoria 3122, Australia
[36] Department of Physics and Astronomy, Oberlin College, Oberlin, OH 44074, USA
[37] Department of Physics and Astronomy, Vanderbilt University, 2301 Vanderbilt Place, Nashville, TN 37235, USA
[38] Department of Physics, The Ohio State University, Columbus, OH 43210, USA
[39] National Astronomical Observatories, Chinese Academy of Sciences, 20A Datun Road, Chaoyang District, Beijing 100012, People's Republic of China

Abstract

We present a new analysis of the profile data from the 47 millisecond pulsars comprising the 12.5 yr data set of the North American Nanohertz Observatory for Gravitational Waves, which is presented in a parallel paper (Alam et al., hereafter NG12.5). Our reprocessing is performed using "wideband" timing methods, which use

[40] Resident at US Naval Research Laboratory, Washington, DC 20375, USA.
[41] NANOGrav Physics Frontiers Center Postdoctoral Fellow.

frequency-dependent template profiles, simultaneous time-of-arrival (TOA) and dispersion measure (DM) measurements from broadband observations, and novel analysis techniques. In particular, the wideband DM measurements are used to constrain the DM portion of the timing model. We compare the ensemble timing results to those in NG12.5 by examining the timing residuals, timing models, and noise-model components. There is a remarkable level of agreement across all metrics considered. Our best-timed pulsars produce encouragingly similar results to those from NG12.5. In certain cases, such as high-DM pulsars with profile broadening or sources that are weak and scintillating, wideband timing techniques prove to be beneficial, leading to more precise timing model parameters by 10%–15%. The high-precision, multiband measurements of several pulsars indicate frequency-dependent DMs. Compared to the narrowband analysis in NG12.5, the TOA volume is reduced by a factor of 33, which may ultimately facilitate computational speed-ups for complex pulsar timing array analyses. This first wideband pulsar timing data set is a stepping stone, and its consistent results with NG12.5 assure us that such data sets are appropriate for gravitational wave analyses.

Unified Astronomy Thesaurus concepts: Millisecond pulsars (1062); Pulsar timing method (1305); Rotation powered pulsars (1408); Binary pulsars (153); Radio pulsars (1353); Pulsars (1306); Gravitational waves (678); Astronomy data analysis (1858); Interstellar medium (847)

1. Introduction

Pulsar timing arrays (PTAs) are poised to make the first detection of nanohertz gravitational waves (GWs) through the decades-long monitoring of dozens of millisecond pulsars (MSPs; Rosado et al. 2015; Taylor et al. 2016). Current PTA experiments include the North American Nanohertz Observatory for Gravitational Waves (NANOGrav;[42] Alam et al. 2020, hereafter NG12.5; Cordes et al. 2019; Ransom et al. 2019), the Parkes Pulsar Timing Array in Australia (PPTA; Hobbs 2013; Kerr et al. 2020), the European Pulsar Timing Array (EPTA; Kramer & Champion 2013; Desvignes et al. 2016), and newly established PTA efforts in India (Joshi et al. 2018; Susobhanan et al. 2020) and China (Lee 2016; Hobbs et al. 2019). Together, the PTA collaborations work together under the umbrella venture called the International Pulsar Timing Array (IPTA; Manchester & IPTA 2013; Perera et al. 2019). Several other key science projects on premier radio telescopes, such as the MeerTime project with the MeerKAT telescope (Bailes et al. 2018) and the CHIME/Pulsar collaboration with the eponymous CHIME telescope (Ng 2018), will soon contribute to the ensemble PTA effort. Furthermore, planned telescopes like the DSA-2000 (Hallinan et al. 2019) and the ngVLA (McKinnon et al. 2019) will significantly broaden the impacts of PTA science.

The raw data collected by the PTA observations in all of the above often take the form of light curves, called pulse profiles, which map the average radio flux density to the rotational phase of the neutron star as a function of time, frequency, and polarization. Pulsar timing methods in general obtain pulse times of arrival (TOAs) by cross-correlating these data profiles with a template profile (e.g., Lommen & Demorest 2013). A timing model of the neutron star's rotation is fit to the observed TOAs and predicts future rotations of the neutron star (e.g., see chapter 8 of Lorimer & Kramer 2005). TOA measurements have historically been and will continue to be the fundamental timing quantities of interest until other methods become more commonly implemented, such as those that produce timing model solutions by examining the profile data directly (Lentati et al. 2015, 2017b).

Along with the anticipation of GW detection are the expectations that the number of MSPs that comprise the array and the bandwidth of PTA observations will increase. In particular, for NANOGrav, we project to have >100 MSPs timed by the middle of the decade and to be using an ultrawideband receiver (between ∼0.7 and 4.0 GHz) at at least one of our facilities in the near future (see Ransom et al. 2019). Indeed, large-fractional-bandwidth receivers have already been deployed by the PPTA (Hobbs et al. 2020) and the EPTA[43] for high-precision pulsar timing, and large-fractional-bandwidth or multiband subarraying capabilities are either planned or are implemented in all of the aforementioned efforts.

The PTA detection of low-frequency GWs requires both high-cadence pulsar timing in addition to as many long pulsar data sets as possible (Burt et al. 2011; Siemens et al. 2013; Lam 2018; Burke-Spolaor et al. 2019). The combination of more MSPs and increased bandwidth presents PTAs with an ever-increasing, and perhaps intractable, number of TOAs that need to be analyzed. This problem is compounded not just by the long-term nature of PTAs, but also by the increasing rate of observation, as is the case for the roughly daily cadence of observations by CHIME/Pulsar, which will later be integrated into NANOGrav data sets. As demonstrative examples, there are almost two-and-a-half times the number of TOAs for a single NANOGrav pulsar in our most recent data set than there are in the entire first NANOGrav data set, and, depending on the exact observations and processing protocol, CHIME/Pulsar by itself may double our current TOA volume after a single year of collecting data. The absolute number of TOAs, as well as the number of timing model parameters (including parameterizations of the noise), plays a determining role in the time it takes to perform GW analyses of PTA data (Ellis et al. 2013; Lentati et al. 2013b; van Haasteren & Vallisneri 2014, 2015). Advanced data analysis techniques to handle this deluge of TOAs will need to be significantly improved if we want to avoid delays on the numerous science deliverables offered by PTAs (Cordes et al. 2019; Fonseca et al. 2019; Goulding et al. 2019; Kelley et al. 2019; Lynch et al. 2019; Mingarelli 2019; Siemens et al. 2019; Stinebring et al. 2019; Taylor et al. 2019).

A naive suggestion is to frequency-average the profiles, which would reduce the number of TOAs by factors of dozens. However, maintaining frequency resolution in MSP timing observations is required when observing with even moderate fractional bandwidths for at least three reasons: (1) inter-observational changes in the dispersive delay due to the homogeneous, ionized interstellar medium (ISM) may be measurable and need to be modeled as part of the timing model, (2) the profile shape may change as a function of

frequency, which will blunt the timing accuracy and precision if unmodeled, and (3) the effects of diffractive scintillation, particularly in combination with (2), may need to be accounted for. The dispersive delay is proportional to the column density of free electrons along the line of sight, which is called the dispersion measure (DM), and the measurement and accommodation of DM changes are outstanding problems in high-precision pulsar timing (Keith et al. 2013; Lentati et al. 2013a; Lee et al. 2014; Lam et al. 2016a; Jones et al. 2017). Additionally, as bandwidths grow, more subtle effects arising from the inhomogeneity in the ISM become more prominent in pulsar timing; these effects include profile broadening (Geyer & Karastergiou 2016; Levin et al. 2016; Geyer et al. 2017; Lentati et al. 2017a), nondispersive delays (Foster & Cordes 1990; Lam et al. 2018a), and frequency-dependent DMs (Cordes et al. 2016; Donner et al. 2019; Lam et al. 2020).

Current methods to handle these issues grew mostly out of historical practices and do not address the TOA volume issue. For instance, in the NANOGrav 5 yr data set (Demorest et al. 2013, hereafter NG5), we used individual phase offset parameters between frequency channels (called "JUMP" parameters) to account for frequency-dependent profile shapes that were evident even in the data from our narrower bandwidth data acquisition back ends, ASP and GASP. A simpler model was employed in the three subsequent data sets, the 9, 11, and 12.5 yr data sets (hereafter referred to as NG9 (Arzoumanian et al. 2015), NG11 (Arzoumanian et al. 2018b), and NG12.5, respectively), in which a polynomial is fit to the average frequency-dependent TOAs as a function of log frequency. This model, parameterized by "FD" (frequency-dependent) parameters, was necessitated by the adoption of the PUPPI and GUPPI back ends, which are capable of processing bandwidths that are wider by more than an order of magnitude. However, no direct modeling of the evolving pulse profile shapes is performed to make those data sets.

Pennucci et al. (2014) and Liu et al. (2014) contemporaneously provided the beginnings of a new solution, which conveniently addresses profile evolution, ISM variations, and the TOA volume problem in one framework, referred to as "wideband timing." The basic idea is to use a combination of a frequency-dependent profile model with an augmented TOA measurement algorithm to produce two measurements irrespective of the frequency resolution of the profile data: one TOA and one DM. The use of wideband TOAs and their associated DM measurements requires special attention and new techniques, which are detailed later. For this reason, up until now, there has been no published, large-scale application of wideband timing for PTAs or other projects, although early, proof-of-concept demonstrations on NG9 can be found in Pennucci (2015).

In NG12.5, we presented our 12.5 yr data set, the creation and timing analyses of which use subbanded (i.e., per frequency channel) TOAs; we refer to that data set and its analysis with the moniker "narrowband" (NB). Here we present new analyses of the same pulse profile data for the same 47 MSPs, reduced into the form of wideband TOAs with DM measurements and associated timing models, and refer to it as the "wideband" (WB) data set. As we demonstrate, this first-ever wideband data set yields consistent timing results and is publicly available in parallel with the narrowband data set.[44]

The structure of this paper is as follows. In Section 2, we briefly summarize the observations but refer the reader to NG12.5 for the full description. In Section 3, we detail the generation of the wideband data set, including frequency-dependent template profile modeling, TOA measurement, and data set curation. In Section 4, we present the ensemble results, which are largely consistent with those from NG12.5, in a concise, comparative format; we also examine particular results from several individual pulsars. In Section 5, we summarize the discussion and comment on the future and ongoing development of wideband timing for NANOGrav and other purposes. Appendix A contains an analysis of wideband TOAs in the low-signal-to-noise-ratio (S/N) limit. Appendix B describes the revised pulsar timing likelihood with which we analyze each pulsar's data set. Appendix C contains the timing residuals and DM variations for all pulsars from both data sets for ease of comparison. We direct the reader to NG12.5 for discussions on new astrophysical results arising from the 12.5 yr data set. Furthermore, the results from searching the 12.5-year narrowband data set for a stochastic background of GWs have been reported in Arzoumanian et al. (2020), and a similar analysis of the wideband data set will be presented elsewhere.

2. Observations

The observations comprising the NANOGrav 12.5 yr data set were collected between 2004 July and 2017 June, with timing baselines for individual pulsars in the range of 2.3–12.9 yr. Of the 47 MSPs presented here, 17 of them have been observed since the original NG5 data set, we added 20 more in NG9, 9 more in NG11 (with one NG9 source, J1949 +3106, removed), and 2 MSPs have been added for the present data set: J1946+3417, and J2322+2057.

All data were collected either at the 305 m Arecibo Observatory (AO) or the 100 m Robert C. Byrd Green Bank Telescope (GBT). Any pulsar that is visible with the more sensitive AO dish is observed there; otherwise, we observe it with the GBT. Arecibo was used to observe 26 sources, while 23 sources have data from the GBT. We regularly observe J1713+0747 and B1937+21 (a.k. a. J1939+2134) with both facilities.

Most pulsars are observed once every 3–4 weeks, with six sources being observed weekly: J0030+0451, J1640+2224, J1713 +0747, J2043+1711, and J2317+1439 at AO since 2015, and J1713+0747 and J1909−3744 with the GBT since 2013.

All pulsars are observed with receivers in two widely separated frequency bands during each epoch in order to measure propagation effects from the ISM, including variations in the DM. At Arecibo, these frequency bands are two of three possible receivers centered around 430 MHz (∼70 cm), 1.4 GHz (∼20 cm, "L band"), and 2.1 GHz (∼15 cm, "S band"); the use of the 327 MHz (∼90 cm) receiver for one source, J2317+1439, has been discontinued since the end of 2013. At the GBT, all sources are observed with the 820 MHz (∼35 cm) and 1.4 GHz receivers. The receiver turret at Arecibo accommodates back-to-back observations on the same day, defining one observational epoch, whereas mechanical and logistical factors demand that the two observations comprising a single epoch be separated by a few (∼3) days at the GBT.

Between approximately 2010 and 2012, we transitioned from the 64 MHz-bandwidth-capable ASP and GASP data acquisition back-end instruments at Arecibo and the GBT, respectively (Demorest 2007), to the 800 MHz-bandwidth-capable PUPPI and GUPPI instruments (DuPlain et al. 2008; Ford et al. 2010). Details of these instruments, their coverage of

---

Table 1
Observing Frequencies and Bandwidths[a]

		Back Ends						
		ASP/GASP				PUPPI/GUPPI		
Telescope Receiver	Data Span[b]	Frequency Range[c] (MHz)	Usable Bandwidth[d] (MHz)	ΔDM Delay[e] (μs)	Data Span[b]	Frequency Range[c] (MHz)	Usable Bandwidth[d] (MHz)	ΔDM Delay[e] (μs)
Arecibo								
327	2005.0–2012.0	315–339	34	2.86	2012.2–2017.5	302–352	50	6.00
430	2005.0–2012.3	422–442	20	1.03	2012.2–2017.5	421–445	24	1.23
L-wide	2004.9–2012.3	1380–1444	64	0.09	2012.2–2017.5	1147–1765	603	0.91
S-wide	2004.9–2012.6	2316–2380	64	0.02	2012.2–2017.5	1700–2404[f]	460	0.36
GBT								
Rcvr_800	2004.6–2011.0	822–866	64	0.30	2010.2–2017.5	722–919	186	1.52
Rcvr1_2	2004.6–2010.8	1386–1434	48	0.07	2010.2–2017.5	1151–1885	642	0.98

Notes.
[a] Table reproduced and modified from NG9.
[b] Dates of instrument use. Observation dates of individual pulsars vary; see Figure 1.
[c] Typical values; some observations differed. Some frequencies unusable due to radio frequency interference.
[d] Nominal values after excluding narrow subbands with radio frequency interference.
[e] Representative dispersive delay between profiles at the extrema frequencies listed in the Frequency Range column induced by a $\Delta DM = 5 \times 10^{-4}$ cm^{-3} pc, which is approximately the median uncertainty across all wideband DM measurements in the data set; for scale, 1 μs $\sim$ 1 phase bin for a 2 ms pulsar with our configuration of $n_{bin} = 2048$.
[f] Noncontiguous usable bands at 1700–1880 and 2050–2404 MHz.

the receivers' bandwidth, and the transition can be found in NG9. However, because the observed frequency ranges are of relevance to this work, we list them in Table 1, adopted from Table 1 of NG9.

Our procedures for flux and polarization calibration, as well as for excision of radio frequency interference (RFI), are unchanged from NG11. Although dual polarization measurements are made, only the total intensity information is used in the timing analyses of either data set.

The profile data used to measure TOAs in both the narrowband and wideband data sets have $n_{bin} = 2048$ rotational phase bins and are time-averaged to have subintegration times up to 30 minutes or 2.5% of the orbital period for binary pulsars, whichever is shorter. The ASP and GASP data are left at their native 4 MHz frequency channel resolution, whereas the PUPPI and GUPPI data are frequency-averaged to have channel bandwidths in the range 1.5–12.5 MHz, depending on the frequency range observed.

These final, folded, calibrated, and reduced profile data sets represent the same starting place for both the narrowband and wideband analyses. Further details about the observations, their calibration, and data reduction can be found in NG12.5 and the earlier data set papers.

However, one new development in the preparation of these profiles that is important to highlight in the context of Section 3.3 is the correction of artifact images due to imperfect sampling of the pulsar signal. To summarize the details found in NG12.5, PUPPI and GUPPI use interleaved analog-to-digital converters (ADCs) that have slightly unbalanced gains and that do not sample exactly out of phase with one another. If uncorrected, a very low-amplitude band-flipped copy of the signal remains in the data, which corrupts the modeling of the profile evolution for pulsars with certain combinations of spin period, DM, and S/N. Following Kurosawa et al. (2001), the PUPPI and GUPPI profile data for each receiver were corrected

for these artifact images using a routine implemented in the pulsar data reduction package PSRCHIVE (Hotan et al. 2004) as part of NG12.5. Some of the profiles for certain PUPPI observations could not be corrected; the TOAs obtained from these observations come with an additional metadata flag (see Table 2).

The timing baselines and observational coverage in the form of multifrequency epochs for each pulsar are shown in Figure 1. An analogous figure is presented in NG12.5, but there are small differences in the exact epochs, as will be detailed in Section 3.4.

3. Construction of the Wideband Data Set

3.1. Overview

The measurement of TOAs from pulsar data with a large instantaneous bandwidth was first developed in Liu et al. (2014) and Pennucci et al. (2014), and further explored in Pennucci (2015, 2019). We refer the reader to those works for details and here briefly summarize the important points.

A single narrowband TOA corresponds to the time of arrival of a pulse profile observed in a single frequency channel[45] (sometimes referred to as a "subband"); in contrast, a single wideband measurement is composed of both the TOA of a pulse at some reference frequency and an estimate of the DM at the time of observation. The difference can be conceptualized thusly: narrowband TOAs from a single subintegration are like the individual, scattered measurements around a linear relationship, whereas the fitted intercept and slope to this relationship are like the wideband TOA and DM, respectively. The log-likelihood function for the wideband measurements is reproduced in Section 3.2.

___

[45] Another similar protocol used in the pulsar timing community is to produce band-averaged TOAs, in which the detected profiles are summed over the observing bandwidth, creating a single profile from which to extract the TOA.

Table 2
Wideband TOA Flags
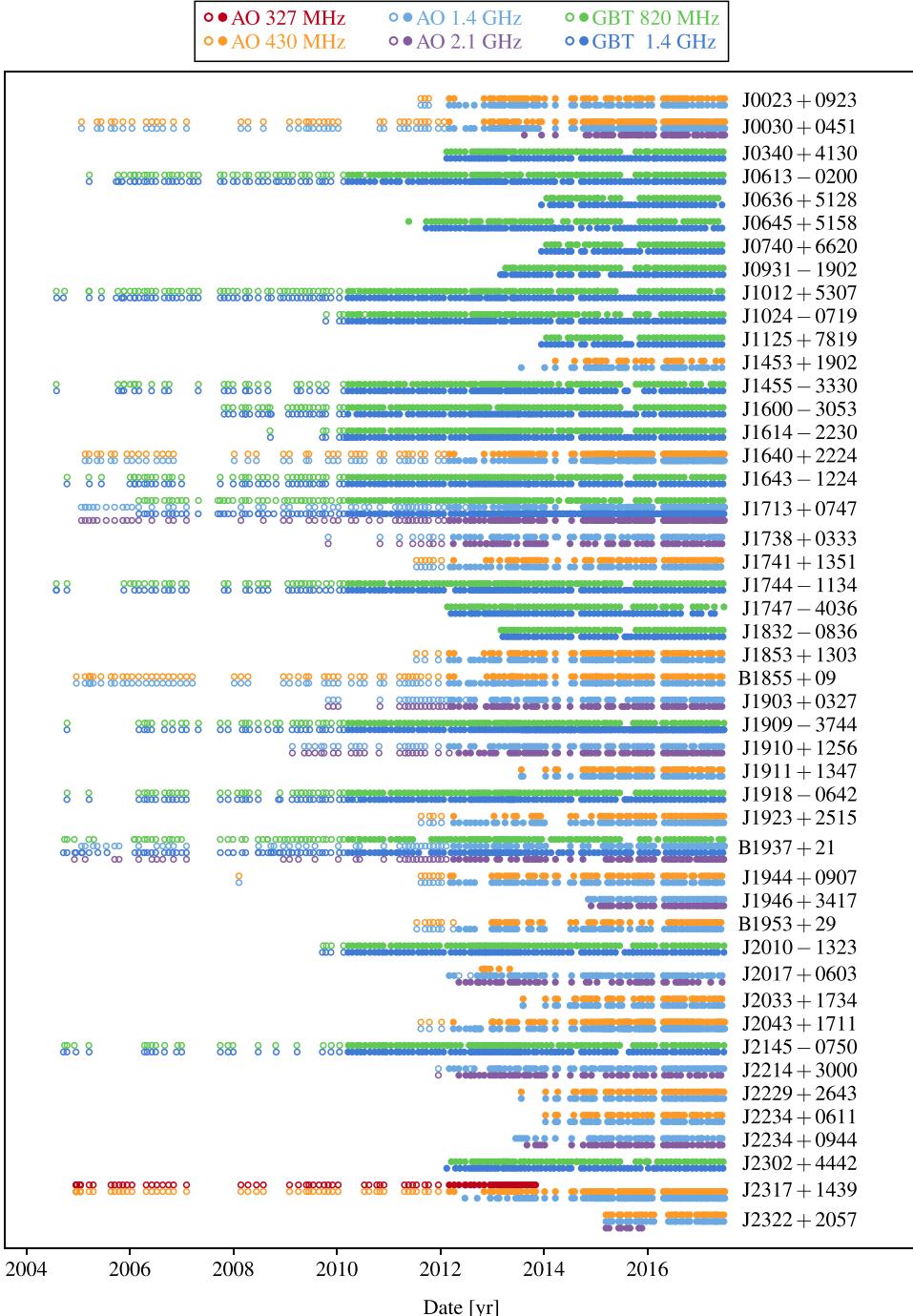
Flag	Meaning	Notes
-pp_dm *value*	Dispersion Measure [cm^{-3} pc]	*value* is the wideband DM estimate from Equation (2) associated with the TOA.
-pp_dme *value*	Dispersion Measure Uncertainty [cm^{-3} pc]	*value* is the estimated 1σ uncertainty on the DM estimate.
-nch *value*	Number of Channels	*value* is the integer number of frequency channels (n_{chan}); this in contrast to the -nch flag in the narrowband data set, which is the number of channels averaged together from the original, raw data.
-nchx *value*	Number of Channels Used	*value* is the integer number of non-zero-weighted frequency channels in the associated subintegration used in the wideband TOA fit.
-chbw *value*	Channel Bandwidth [MHz]	$value = \text{bandwidth}/n_{chan}$. The total bandwidth can be recovered from this number and n_{chan}.
-bw *value*	Effective Bandwidth [MHz]	*value* is the difference between the highest and lowest channels' center frequencies used in the wideband TOA fit; this is in contrast to the -bw flag in the narrowband data set, which is the bandwidth for each TOA, i.e., the channel bandwidth provided here by the -chbw flag.
-fratio *value*	Frequency Ratio	*value* is the ratio of the highest and lowest channels' center frequencies; in combination with the effective bandwidth, this value can be used to recover the two frequencies.
-snr *value*	TOA Signal-to-Noise Ratio (S/N)	Similar to the conventional TOA flag, but calculated using Equation (A3).
-gof *value*	TOA Goodness of Fit ($\chi^2_{reduced}$)	Similar to the conventional TOA flag, but calculated using Equation (2) and the relevant number of degrees of freedom.
-flux *value*	Flux Density [mJy]	Analogous to the -flux flag in the narrowband data set, *value* is the estimated mean flux density for the subintegration (see Section 4.1).
-fluxe *value*	Flux Density Uncertainty [mJy]	Analogous to the -fluxe flag in the narrowband data set, *value* is the estimated 1σ uncertainty on the flux density.
-flux_ref_freq *value*	Flux Density Reference Frequency [MHz]	*value* is the reference frequency for the mean flux density estimate.
-img uncorr	Incomplete Artifact Image Correction	Some of the profiles in this subintegration did not undergo removal of the ADC artifact image (see Section 2 and NG12.5).
Flags Indicating a Removed TOA		
-cut dmx	The ratio of maximum to minimum frequencies observed in a DMX epoch $\nu_{max}/\nu_{min} < 1.1$.	ν_{max} and ν_{min} are calculated from the -bw and -fratio flags here, but correspond to individual TOA reference frequencies in the narrowband data set. This cut is based on the minimum and maximum frequencies across all TOAs in a DMX bin. (968)
-cut simul	Identifies an ASP/GASP TOA acquired at the same time as a PUPPI/GUPPI TOA.	These TOAs represent duplicate information and were removed at the very last stage of analysis. (576)
-cut snr	The TOA does not meet a signal-to-noise ratio threshold.	TOAs for which -snr has *value* < 25; for the narrowband TOAs, the threshold is 8 (see Appendix A). (500)
-cut epochdrop	Entire epoch removed based on an epoch-by-epoch removal analysis.	Epochs identified by this analysis in the narrowband data set are removed also in the wideband data set; see NG12.5 for details. (68)
-cut one	The subintegration only has one frequency channel.	TOAs for which -nchx has a value of 1; a DM cannot be estimated from this observation. (33)
-cut manual	An outlier determined by manual inspection.	In most cases, the TOA's corresponding profile data is corrupted by instrumentation or RFI. These were identified independently from the narrowband TOAs that have the same flag. (29)
-cut cull	The TOA had a large residual in the initial timing analysis.	We used the Tempo utility program cull to identify TOAs that had a residual >100 μs. These outliers were confirmed by human inspection to have an issue. (6)

Note. The -cut flags are ordered here by how many such wideband TOAs were removed from the analyses (numbers in parentheses). All cut TOAs are provided as commented-out TOAs in the ASCII-text TOA files; excluding these, there are 12,598 wideband TOAs in the data set. See NG12.5 for additional information on TOA flags. Other flags and the TOA format we use ("IPTA") are conventional and are neither listed nor explained here.

The second important difference in the new wideband data set is not fundamental to the measurement of the TOA. Heretofore we have used a single, frequency-independent template profile for each receiver band to generate narrowband TOAs and have used FD parameters (Arzoumanian et al. 2015) to account for constant phase offsets originating from the mismatch between the template and the evolving shape of the profiles. For the measurement of wideband TOAs, we explicitly account for pulse profile evolution by using a high-fidelity, noise-free, frequency-dependent model for each receiver band. See Section 3.3 for a brief description of how these models are created.

Although the narrowband and wideband data sets were developed in parallel, the established techniques in preparing the former allowed us to use some information from its final products to facilitate the production of the latter. In particular, some of the curating performed, including flagging bad epochs, as well as the initial timing, was borrowed from the narrowband analysis. In this way, the wideband data set is not completely independent, as is detailed in Sections 3.4 and 3.5.

It is important to underscore that the wideband data set for each pulsar is composed of TOAs that are paired with estimates of the instantaneous DM. What makes the analysis of the

Figure 1. Epochs of all observations in the data set. The color of each marker indicates the radio frequency band and observatory, as listed in the legend at the top; these colors are also used in Figures 2, 5, and 8, and in the pulsar-specific plots of Appendix C. The back-end data acquisition system is indicated by marker type: open circles are ASP or GASP, whereas filled circles are PUPPI or GUPPI.

wideband data set truly unique is that these DM estimates inform the portion of the timing model that accounts for DM variability (for our analyses, this is "DMX"; see Section 3.5). In Section 3.5, we describe our approach, with greater detail in Appendix B; the results are examined in Section 4.

Publicly available code[46] is used for both the generation of frequency-dependent templates and the measurement of the wideband TOAs (Pennucci et al. 2016).

3.2. Wideband TOA Log-likelihood Function

All of our narrowband and wideband TOAs are measured using what is now referred to as the "Fourier phase-gradient shift algorithm" (Taylor 1992, historically known as "FFTFIT"), which makes use of the Fourier shift theorem to achieve a phase offset precision much better than a single rotational phase bin and which is computationally efficient by virtue of avoiding the time-domain cross-correlation calculation between the data and template pulse profiles. We use a similar notation to Appendix B of NG9, but see also

---

[46] https://github.com/pennucci/PulsePortraiture

Demorest (2007) and Pennucci et al. (2014) for details of what follows. The time-domain model has the assumed form

$$D(\nu, \varphi) = B(\nu) + a(\nu)T(\nu, \varphi - \phi(\nu)) + N(\nu). \quad (1)$$

That is, for each subintegration in an observation, we assume that the data profiles D as a function of rotational phase φ and frequency ν can be described by a template T that is shifted in phase by ϕ and scaled in amplitude by a, with added Gaussian-distributed phase-independent noise N; the term B represents the bandpass shape. After discretizing these quantities, taking the discrete Fourier transform (DFT), making use of the Fourier shift theorem, and rearranging terms, we can reformulate Equation (1) into our TOA log-likelihood,

$$\chi^2 = \sum_{n,k} \frac{|d_{nk} - a_n t_{nk} e^{-2\pi i k \phi_n}|^2}{\sigma_n^2}. \quad (2)$$

In Equation (2), the integer index k is the Fourier frequency (conjugate to rotational phase or time), t_{nk} is the DFT of the template profile for the frequency channel indexed by n (with frequency center ν_n), a_n is the scaling amplitude parameter for the template, ϕ_n is the phase offset for the template, and d_{nk} is the DFT of the data profile for frequency channel n, which has the corresponding Fourier-domain noise level σ_n^2.[47]

For conventional TOAs, the optimization of this function takes place on an individual channel basis, in which case there is no index n in Equation (2) over which a summation occurs. Moreover, for our narrowband TOAs, t_{nk} is not a function of n; that is, profile evolution is not accounted for by changing the shape of the template across a single receiver's frequency band. Instead, in NG12.5, a single template profile is used for each receiver band and constant phase offsets arising from the mismatch between the template shape and the evolving pulse shape are accounted for via FD parameters in the narrowband timing models.

The crucial difference in wideband TOAs is that the phase offsets ϕ_n in Equation (2) are constrained to follow the cold-plasma dispersion law, proportional to ν^{-2}:

$$\phi_n(\nu_n) = \phi_\circ + \frac{K \times \mathrm{DM}}{P_s}(\nu_n^{-2} - \nu_{\phi_\circ}^{-2}), \quad (3)$$

where P_s is the instantaneous spin period of the pulsar, K is the dispersion constant (a combination of fundamental physical constants approximately equal to 4.148808×10^3 MHz^2 cm^3 pc^{-1} s), DM is the dispersion measure, and $\phi_\circ$ is the phase offset at reference frequency $\nu_{\phi_\circ}$. Equation (2) can be recast using the maximum-likelihood values of a_n and rewritten as a function of only the two parameters $\phi_\circ$ and DM (see Pennucci et al. 2014), which can then be readily optimized numerically. We calculate the parameter uncertainties using the Fisher matrix and choose $\nu_{\phi_\circ}$ such that there is zero covariance between the DM and $\phi_\circ$, the latter of which is directly related to the TOA.

Additional terms to the wideband TOA log-likelihood are currently being explored (T. T. Pennucci et al. 2020, in preparation), which include accounting for pulse broadening from multipath propagation through the turbulent ISM (i.e., "scattering") in a similar fashion to Lentati et al. (2017a), as

well incorporating a higher-order delay term besides ν^{-2}, the motivation for which are discrete ISM "events" (Lam et al. 2018a). The low-frequency, high-cadence capabilities offered by CHIME/Pulsar will make tracking the interstellar weather in this way an exciting endeavor, following in the footsteps of studies like Ramachandran et al. (2006) and Driessen et al. (2019; long-term ISM tracking of B1937+21 and the Crab pulsar, respectively).

3.3. Frequency-dependent Template Profiles

The evolving template t_{nk} in Equation (2) can be freely chosen, and in this work, we employ the modeling method from Pennucci (2019), which describes a generalized, frequency-dependent version of our usual protocol for making template profiles. In contrast, to make the conventional noise-free templates used in NG12.5 for narrowband TOA measurement, all profiles for each combination of pulsar and receiver are averaged together to build a single, high-S/N mean profile, which is then smoothed. We direct the reader to Pennucci (2019) for details, but we summarize its novel procedure as follows.

An analogous averaging of the data for each combination of pulsar and receiver is performed, but frequency resolution is maintained to arrive at a high-S/N mean "portrait" (a collection of nominally aligned mean pulse profiles across a contiguous frequency band); only the PUPPI and GUPPI data were averaged for this purpose. A principal component analysis is performed on the average portrait, and the most significant, highest-S/N eigenvectors (and mean profile) are smoothed to become noise-free basis functions ("eigenprofiles"). The mean-profile-subtracted profiles from the average portrait are projected onto each of the eigenprofiles, producing a set of coefficients for each. These coefficients are simultaneously fit to a slowly varying spline function that is parameterized by frequency and encapsulates the evolution of the pulse profile shape.

In this manner, a template profile T at any frequency ν can be constructed by evaluating the n_{eig} coefficient spline functions B_i at ν, linearly combining the eigenprofiles $\hat{e}_i$ using these coefficients, and adding the result to the mean profile $\widetilde{p}$,

$$T(\nu) = \sum_{i=1}^{n_{\mathrm{eig}}} B_i(\nu)\, \hat{e}_i\, +\, \widetilde{p}. \quad (4)$$

In summary, a single model for generating high-fidelity, noise-free template profiles is composed of the smoothed mean profile, the smoothed basis eigenprofiles, and a function to describe the profile evolution curve in that basis.

These models were made for each combination of pulsar and receiver, and then used to measure wideband TOAs according to Equation (2). The modeling procedure attempts to guess the true, unknown profile alignment by starting with the same Occam assumption used in the narrowband analysis: there is no profile evolution, neither in the shape nor alignment of the profiles. This assumption is used to initially align and average the profile data by using the fixed, mean profile shape as a reference for the alignment. After iteratively aligning and averaging the profile data and then creating a model, it should not come as a surprise that the absolute, average DM measured in each receiver band will differ slightly. We minimize this difference by measuring the weighted-mean DM offset relative to the DM measured in the lowest frequency band. The DM offset was then applied as a rotation proportional to ν^{-2} to the

---

[47] σ_n^2 is the noise for either the real or imaginary part and is larger than its (real) time-domain counterpart by a factor of $n_{\mathrm{bin}}/2$.

average portrait, the profile evolution model was recreated, and the TOAs were remeasured; this process was iterated a total of three times. The reference DM choice was made relative to the lowest frequency band because, except in the cases of Arecibo pulsars observed only at the L and S bands, this will be a frequency band with a lower fractional bandwidth than the L band, but from which reasonably precise DM measurements are made. This choice gave better modeling results than rotating the averaged low-frequency data relative to the L-band alignment, which may be ambiguous due to profile evolution. For the other sources, the S band generally does not give precise DM measurements, and so the L band is used as the reference. See Section 4.2 for more discussion on this topic.

The initial set of wideband TOAs used in the timing and noise analyses were measured with these DM-aligned models, and instrumental time offsets were applied to TOAs from ASP and GASP profiles, as detailed in Appendix A of NG9. Metadata in the TOA files take the form of "flags," which get appended to each TOA line in the files. A number of new TOA flags have been added to aid wideband timing analyses, and a few of the usual TOA flags have different meanings from their narrowband TOA counterparts; these are listed in the top portion of Table 2.

The choice of DM alignment in wideband profile models is analogous to the ambiguity of absolute phase between TOAs measured with different template profiles in the narrowband analysis. Those constant phase offsets are modeled in the timing model with so-called "JUMP" parameters and are also present in the wideband analysis. Our fiducial DM alignment is an attempt at getting the simplest profile evolution models, but a new, analogous timing model parameter is necessary when using multiband DM measurements as data for the timing model. To this end, we implemented "DMJUMP" parameters for wideband timing in the extended likelihood introduced in Section 3.5. Appendix B contains details about how these parameters influence the timing model.

3.4. Cleaning and Curating the Wideband Data Set

The narrowband data set was prepared in advance of the wideband data set, and as a part of its creation we kept track of bad observations that were corrupted by instrumentation or calibration issues, or were so affected by RFI that we excised them outright (250 of 11,178 observations). These observations (which are included in the narrowband data set as commented TOAs with the flag `-cut badepoch`) were simply not introduced into the wideband pipeline. There are also a small number of observations (36) for which data were taken on a pulsar using a different receiver than usual, often for testing purposes (these are included in the narrowband data set as commented TOAs with the flag `-cut orphaned`). These data are generally not sufficient to create good profile evolution models and would add very few degrees of freedom; we similarly excluded them from the wideband analysis at the start.

There was one other additional step in curating the profile data set used to make wideband TOAs. Upon finishing the modeling procedure described in Section 3.3, we calculated goodness-of-fit statistics for each profile in the data set based on its predicted pulse shape from the corresponding model. Profiles in a given subintegration were zero-weighted if their goodness of fit exceeded a threshold ($\chi^2_{\mathrm{reduced}} > 1.25$), which was empirically determined after examining the distributions for each combination of pulsar and receiver.

For most combinations, the number of discarded profiles in this manner was of order a few percent. After zero-weighting these profiles, the data were reaveraged and the profile evolution models were recreated. This step was necessary because, as with the ADC artifact mentioned in Section 2, unmitigated RFI can corrupt the modeling procedure. More general RFI-flagging techniques based on template matching using the wideband profile models are in development within NANOGrav and elsewhere (MeerTime collaboration 2020, private communication). Such techniques could potentially identify irregularities in the profiles, be it from RFI or other sources, earlier in the reduction pipeline.

The remainder of the cleaning of the wideband data set was performed on the measured TOAs; any TOAs "cut" from further analysis were given one of the flags listed in Table 2, but are included as commented TOAs in the publicly available text files. Most of the cuts described in the table have counterparts in the preparation of the narrowband data set, and we refer the reader to NG12.5 for details beyond those offered in the table and those that follow.

The S/N threshold used for the wideband TOAs was set at 25, compared to the value of 8 used for narrowband TOAs. The main reason for this was empirical and related to the fact that the estimated S/N for wideband TOAs is subject to significant bias in the low-S/N regime, favoring a higher threshold than is naively derived. We justify this choice in Appendix A.

Note that in NG11 and NG12.5 a numerical TOA outlier analysis is performed (Vallisneri & van Haasteren 2017). Some of the narrowband TOAs identified in this way are from profiles corrupted by RFI or instrumental problems that were not otherwise identified. Our goodness-of-fit filter of the profile data described earlier served a similar purpose, and no separate outlier TOA analysis was performed. We found that after filtering the profiles in this way and thresholding the TOAs based on the S/N cutoff of 25, the initial timing results were remarkably clean; there were only a handful of additional TOAs that were culled based on a large timing residual ($>100\,\mu s$) or were otherwise identified by eye (see Table 2).

Overall, despite the procedural differences in preparing the two data sets, the quality control for the wideband data set resulted in $\sim16\%$ more profiles used for TOA measurement, as can be seen in Table 3. This difference is largely due to the inclusion of low-S/N ratio profiles that are discarded in the narrowband data set (see Appendix A); as such, it is unsurprising that these additional data in general do not carry a proportionally large impact on the timing results, as will be shown. However, see Section 4.5 for specific examples.

After curation, the resulting wideband data set has 12,598 TOAs, corresponding to 480,474 profiles; this is compared to the 415,122 TOAs in the narrowband data set, a factor of ~33 larger in TOA volume, which will only grow as the ASP and GASP TOAs become a fractionally smaller subset of the entire data set and as new wideband facilities and receivers come into use. Note, however, that the overall wideband data set volume is only a factor of $33/2 \sim 16$ smaller, after including the DM measurements in the analysis.

A summary of the TOA uncertainties are presented in two forms. First, the median uncertainties are listed, along with other basic pulsar parameters, in Table 4. There is an analogous table in NG12.5 for the narrowband TOAs; in both cases, the uncertainties have been scaled to estimate the median TOA uncertainty from a 1800 s observation of the pulsar with

Table 3
Data Volume Comparison

Source	# TOAs (WB)	# Prof. (WB)	# TOAs (NB)	Diff. (%)
J0023+0923	589	17846	12516	43
J0030+0451	488	12607	12543	1
J0340+4130	164	9092	8069	13
J0613−0200	360	13683	13201	4
J0636+5128	711	38309	21374	79
J0645+5158	217	11800	7893	50
J0740+6620	86	4679	3328	41
J0931−1902	123	6712	3712	81
J1012+5307	554	21334	19307	11
J1024−0719	230	12206	9792	25
J1125+7819	108	5853	4821	21
J1453+1902	68	2148	1555	38
J1455−3330	282	11996	8408	43
J1600−3053	313	14345	14374	0
J1614−2230	275	13433	12775	5
J1640+2224	418	10078	9256	9
J1643−1224	319	12786	12798	0
J1713+0747	1012	36501	37698	−3
J1738+0333	269	9542	6977	37
J1741+1351	147	4255	3845	11
J1744−1134	347	14106	13380	5
J1747−4036	151	8096	7572	7
J1832−0836	120	6630	5364	24
J1853+1303	134	3968	3544	12
B1855+09	313	6340	6464	−2
J1903+0327	156	4893	4854	1
J1909−3744	550	24329	22633	8
J1910+1256	172	5392	5012	8
J1911+1347	88	2621	2625	0
J1918−0642	379	15000	13675	10
J1923+2515	119	3588	3009	19
B1937+21	525	16067	17024	−6
J1944+0907	138	3923	3931	0
J1946+3417	78	3013	3016	0
B1953+29	119	3395	3421	−1
J2010−1323	278	14360	13306	8
J2017+0603	127	4856	2986	63
J2033+1734	90	2720	2691	1
J2043+1711	316	9505	5624	69
J2145−0750	313	14332	13961	3
J2214+3000	233	9143	6269	46
J2229+2643	97	2853	2442	17
J2234+0611	88	2720	2475	10
J2234+0944	175	6584	5892	12
J2302+4442	174	9602	7833	23
J2317+1439	505	10733	9784	10
J2322+2057	80	2500	2093	19
Total	12598	480474	415122	16

Note. The last column shows the difference between the number of profiles used in measuring all wideband TOAs (third and second columns, respectively) and the number of TOAs in the narrowband data set (fourth column), expressed as an integer-rounded percentage of the latter value. If the two data sets contained identical profiles, there would be an exact one-to-one correspondence between columns three and four. Note that the wideband data set has an equal number of DM measurements as wideband TOAs. The TOA numbers shown here do not include those with a -cut flag, which are included as part of the data release.

100 MHz of bandwidth. Overall, the values are comparable to their narrowband counterparts, but differences may be attributable to any of the following: unmodeled profile evolution in the narrowband data set, the inclusion of very low-S/N profiles in the wideband data set, the additional fit parameter (DM) in the wideband measurement, or other subtle discrepancies. Second, in Figure 2, we graphically present the "raw" median TOA and DM uncertainties with central intervals covering the central 68% of the distribution, ranking pulsars by their median PUPPI or GUPPI L-band TOA uncertainty. We use "raw" to mean that these are the formal, estimated uncertainties from the template-matching procedure, which do not include any other sources of uncertainty and are not scaled in any way. It is obvious from this plot that, depending on the pulsar, the improvement in raw TOA precision after moving from ASP and GASP to PUPPI and GUPPI is a factor of 2–3 or more in many cases, but the DM precision improves by an order of magnitude or more in all receiver bands except 327 and 430 MHz. This improvement is due to the increase in bandwidth covered by PUPPI and GUPPI (see Table 1).

3.5. Obtaining Timing Solutions

We used the 12.5 yr data set results from NG12.5 as initial timing solutions instead of deriving completely new timing results from the extended baselines of the 11 yr data set. This was done in part to facilitate comparisons and in part to reduce the need for redundant analyses. Specifically, any new spin, astrometric, or binary timing model parameters found to be significant in NG12.5 were retained, but FD parameters were removed, as were the parameters that describe the DM model, called DMX.

DMX is a piecewise-constant characterization of DM variability that is part of the timing model. Simpler models of DM variability, such as low-order polynomials, do not describe the data well, but more advanced models, such as those that use a stochastic description of variability (e.g., as a Gaussian process, Lentati et al. 2013a), are currently being investigated. The criteria for dividing up the TOAs into DMX epochs defined by Modified Julian Dates (MJDs) can be found in NG12.5. For each DMX epoch, a DM is measured based on the ν^{-2} dependence of the TOAs that fall within the epoch, and all of these DMX model parameters are measured simultaneously with the fit for the rest of the timing model.

If we were to ignore the wideband DM measurements, the wideband TOA data set would be significantly hampered in the following ways. There are a large number of DMX epochs that contain data from a single receiver. In the cases where such an epoch has a single wideband TOA (instead of the dozens of analogous narrowband TOAs), the corresponding single DMX parameter removes the single degree of freedom, artificially zeroing out the timing residual for this epoch. If there are a few wideband TOAs from the same receiver band in such an epoch, they will have similar reference frequencies, and so the DMX parameter will be poorly constrained and perhaps biased. Finally, even for the majority of DMX epochs for which there are multifrequency wideband TOAs from dual receiver observations, DMX only has access to the TOAs, their uncertainties, and reference frequencies. That is, the information about the dispersive delays across the individual receiver bands (captured by the wideband DM measurements, or, equivalently, the multifrequency TOAs in the narrowband data set) is lost, and DMX only sees the dispersive delay between the bands. As can be seen in most pulsars' DM and DMX time series (see Appendix C), the wideband TOAs and their interband dispersive delay carry more weight in the DMX model than do the intraband delays characterized by their

Table 4
Basic Pulsar Parameters and TOA Statistics

Source	P (ms)	dP/dt (10^{-20})	DM (pc cm^{-3})	P_b (days)	327 MHz		430 MHz		820 MHz		1.4 GHz		2.1 GHz		Span (yr)
J0023+0923	3.05	1.14	14.3	0.1	⋯		0.041	58	⋯		0.550	65	⋯		5.9
J0030+0451	4.87	1.02	4.3	⋯	⋯		0.193	174	⋯		0.368	187	0.998	70	12.4
J0340+4130	3.30	0.70	49.6	⋯	⋯		⋯		0.799	69	1.992	71	⋯		5.3
J0613−0200	3.06	0.96	38.8	1.2	⋯		⋯		0.100	134	0.432	135	⋯		12.2
J0636+5128	2.87	0.34	11.1	0.1	⋯		⋯		0.264	39	0.650	42	⋯		3.5
J0645+5158	8.85	0.49	18.2	⋯	⋯		⋯		0.388	66	1.050	74	⋯		6.1
J0740+6620	2.89	1.22	15.0	4.8	⋯		⋯		0.545	38	0.583	41	⋯		3.5
J0931−1902	4.64	0.36	41.5	⋯	⋯		⋯		0.940	51	2.065	51	⋯		4.3
J1012+5307	5.26	1.71	9.0	0.6	⋯		⋯		0.343	135	0.538	142	⋯		12.9
J1024−0719	5.16	1.86	6.5	⋯	⋯		⋯		0.564	89	0.851	94	⋯		7.7
J1125+7819	4.20	0.69	12.0	15.4	⋯		⋯		0.663	40	1.713	42	⋯		3.5
J1453+1902	5.79	1.17	14.1	⋯	⋯		0.988	28	⋯		2.494	40	⋯		3.9
J1455−3330	7.99	2.43	13.6	76.2	⋯		⋯		1.126	113	1.886	113	⋯		12.9
J1600−3053	3.60	0.95	52.3	14.3	⋯		⋯		0.253	113	0.200	115	⋯		9.6
J1614−2230	3.15	0.96	34.5	8.7	⋯		⋯		0.332	96	0.482	107	⋯		8.8
J1640+2224	3.16	0.28	18.5	175.5	⋯		0.033	177	⋯		0.260	186	⋯		12.3
J1643−1224	4.62	1.85	62.3	147.0	⋯		⋯		0.270	130	0.460	129	⋯		12.7
J1713+0747	4.57	0.85	15.9	67.8	⋯		⋯		0.097	129	0.043	450	0.041	185	12.4
J1738+0333	5.85	2.41	33.8	0.4	⋯		⋯		⋯		0.374	70	1.119	64	7.6
J1741+1351	3.75	3.02	24.2	16.3	⋯		0.100	63	⋯		0.233	73	⋯		5.9
J1744−1134	4.07	0.89	3.1	⋯	⋯		⋯		0.107	128	0.198	126	⋯		12.9
J1747−4036	1.65	1.31	153.0	⋯	⋯		⋯		0.983	62	1.155	65	⋯		5.3
J1832−0836	2.72	0.83	28.2	⋯	⋯		⋯		0.608	53	0.450	53	⋯		4.3
J1853+1303	4.09	0.87	30.6	115.7	⋯		0.278	64	⋯		0.378	70	⋯		5.9
B1855+09	5.36	1.78	13.3	12.3	⋯		0.195	116	⋯		0.128	123	⋯		12.5
J1903+0327	2.15	1.88	297.5	95.2	⋯		⋯		⋯		0.400	75	0.470	78	7.6
J1909−3744	2.95	1.40	10.4	1.5	⋯		⋯		0.040	125	0.086	267	⋯		12.7
J1910+1256	4.98	0.97	38.1	58.5	⋯		⋯		⋯		0.251	83	0.555	84	8.3
J1911+1347	4.63	1.69	31.0	⋯	⋯		0.586	42	⋯		0.109	46	⋯		3.9
J1918−0642	7.65	2.57	26.5	10.9	⋯		⋯		0.358	126	0.605	128	⋯		12.7
J1923+2515	3.79	0.96	18.9	⋯	⋯		0.184	53	⋯		0.665	66	⋯		5.8
B1937+21	1.56	10.51	71.1	⋯	⋯		⋯		0.006	125	0.010	228	0.011	85	12.8
J1944+0907	5.19	1.73	24.4	⋯	⋯		0.242	62	⋯		0.495	72	⋯		9.3
J1946+3417	3.17	0.32	110.2	27.0	⋯		⋯		⋯		0.365	40	0.510	38	2.6
B1953+29	6.13	2.97	104.5	117.3	⋯		0.251	54	⋯		0.753	65	⋯		5.9
J2010−1323	5.22	0.48	22.2	⋯	⋯		⋯		0.344	94	0.685	96	⋯		7.8
J2017+0603	2.90	0.80	23.9	2.2	⋯		0.199	6	⋯		0.327	67	0.765	46	5.3
J2033+1734	5.95	1.11	25.1	56.3	⋯		0.189	40	⋯		0.901	46	⋯		3.8
J2043+1711	2.38	0.52	20.8	1.5	⋯		0.058	132	⋯		0.385	148	⋯		5.9
J2145−0750	16.05	2.98	9.0	6.8	⋯		⋯		0.190	111	0.485	115	⋯		12.8
J2214+3000	3.12	1.47	22.5	0.4	⋯		⋯		⋯		0.560	71	1.491	50	5.5
J2229+2643	2.98	0.15	22.7	93.0	⋯		0.229	46	⋯		0.750	48	⋯		3.9
J2234+0611	3.58	1.20	10.8	32.0	⋯		0.342	39	⋯		0.189	44	⋯		3.4
J2234+0944	3.63	2.01	17.8	0.4	⋯		⋯		⋯		0.214	45	0.617	44	4.0
J2302+4442	5.19	1.39	13.8	125.9	⋯		⋯		0.967	69	1.996	68	⋯		5.3
J2317+1439	3.45	0.24	21.9	2.5	0.081	78	0.056	186	⋯		0.409	141	⋯		12.5
J2322+2057	4.81	0.97	13.4	⋯	⋯		0.217	33	⋯		0.952	33	1.717	8	2.3
Nominal scaling factor[b] (ASP/GASP)					0.6		0.4		0.8		0.8		0.8		
Nominal scaling factor[b] (GUPPI/PUPPI)					0.7		0.5		1.4		2.5		2.1		

Notes.
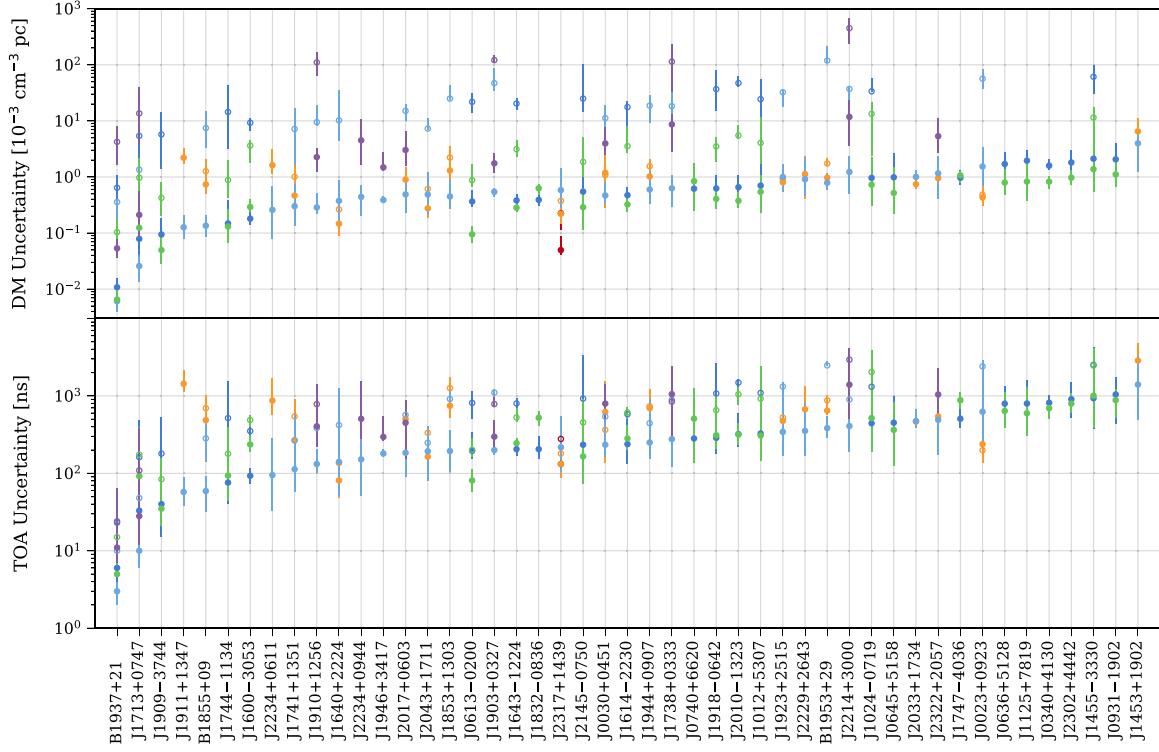
[a] For this table, the original TOA uncertainties were scaled by their bandwidth-time product $\left(\dfrac{\Delta\nu}{100\,\mathrm{MHz}}\dfrac{\tau}{1800\,\mathrm{s}}\right)^{1/2}$ to remove variation due to different instrument bandwidths and integration time.

[b] TOA uncertainties can be rescaled to the nominal full instrumental bandwidth listed in Table 1 by dividing by these scaling factors.

corresponding wideband DM measurements. How much more so depends on the pulsar and receiver bands in question, but it is important to highlight that disregarding the DM data is not a viable option for analyzing this data set. Indeed, we attempted several such analyses, which yielded significantly worse results in many pulsars.

Therefore, not only was it appropriate, but it was also necessary to expand the likelihood used to fit our timing

Figure 2. The median raw wideband TOA and DM measurement uncertainties with central 68% intervals. Pulsars are ordered by their median PUPPI or GUPPI *L*-band (1.4 GHz) TOA uncertainties. The dramatic increase in DM precision after moving from the ASP and GASP back ends (open circles) to the PUPPI and GUPPI back ends (filled circles) is evident. The colors indicate the receiver as in Figure 1: 327 MHz (red), 430 MHz (orange), 820 MHz (green), 1.4 GHz (lighter blue for AO, darker blue for the GBT), and 2.1 GHz (purple).

models so that the wideband DM measurements inform the DM model. In effect, in the new likelihood, the wideband DM measurements influence the timing model as prior information on the DMX values. Each of the TOAs falling within a DMX epoch have a corresponding DM measurement; the weighted average of these measurements is used as the mean of a Gaussian prior on the DMX value for that epoch, while the standard error of the weighted average is the prior distribution's standard deviation. The details of this new likelihood and its implementation in the pulsar timing software packages Tempo (Nice et al. 2015) and ENTERPRISE (Ellis et al. 2019) can be found in Appendix B.

The timing models from NG12.5 were first refit with Tempo using the wideband TOAs only, omitting the DM measurements, to set up the DMX epochs and to get initial DMX values. Including the DM measurements at this point sometimes resulted in poor timing results because there is currently no way to fit the DMJUMP parameters simultaneously with the timing model within Tempo. It is at this stage that TOAs were excluded from further analysis if they did not meet the frequency ratio criterion described in Table 2 or if the entire epoch was removed based on a new analysis performed in NG12.5 (also mentioned in Table 2).

The wideband TOAs, DMs, and timing models were then subject to a Bayesian analysis with ENTERPRISE using the new wideband likelihood. This analysis optimizes the probability of the observed data by characterizing the noise in the timing residuals, which has both white and red components, much in the same way as in NG12.5, NG11, and NG9, with a few important differences:

No ECORR—There is one parameter in the standard white-noise model that is not used in the wideband analyses. This parameter, called ECORR, accounts for the (assumed 100%)

correlation between multifrequency TOAs taken at the same time and is used in the narrowband analyses of NG9, NG11, and NG12.5 (Arzoumanian et al. 2014, 2015). Because wideband TOAs effectively consolidate the many narrowband TOAs into one, any physical effects contributing to this parameter (such as pulse jitter or ISM effects; see Section 4.4.3) would be absorbed by the standard EQUAD noise parameter, which is added in quadrature to the measured TOA uncertainty (Edwards et al. 2006; Lentati et al. 2014). Alternatively, any effects contributing to ECORR in the narrowband analysis may be modeled by a larger and shallower red-noise process in the wideband analysis. A comparison of the detected excess white noise in the two data sets is presented in Section 4.4.3.

DMEFAC and DMJUMP—Two additional parameters are needed in the new wideband likelihood. The first, which we call "DMEFAC," is analogous to the standard TOA EFAC: it is a factor that scales the estimated wideband DM measurement uncertainty. In a similar fashion to the other white-noise parameters, a DMEFAC is assigned for each combination of receiver and back end in each pulsar's noise model. The second was introduced in Section 3.3, which we call "DMJUMP." This parameter is analogous to standard JUMP parameters, but instead of modeling an achromatic phase offset between TOAs measured in different receiver bands, DMJUMP is a DM offset between wideband DMs measured in different bands. These parameters account for the differences in alignment between profile evolution models in disparate bands and amount to making a choice for the absolute DM. It is important to stress that this ambiguity in absolute DM, as well as the offsets in DMs measured in disparate bands, exists also in the narrowband analyses; in NG12.5, the choice of having fixed templates in each band, coupled with using FD parameters to

account for constant TOA biases as a function of frequency, amounts to addressing the analogous problems. We assign one DMJUMP parameter per receiver in each pulsar's timing model, as the profile evolution models are independent of the back end. It may seem that we should use one fewer DMJUMP parameter than there are receivers in each pulsar's analysis, as is done for standard phase JUMP parameters. However, because the DMX model is separately informed by the TOAs, it is not an overdetermined problem. This fact is borne out by examining the posterior chains; although we see that the DMJUMP parameters are often highly covariant, they are not completely degenerate. We used a uniform prior distribution on DMJUMP parameters in the range $[-0.01, 0.01]$ cm^{-3} pc; virtually all of the values are |DMJUMP| < 0.004 cm^{-3} pc.

White-noise priors—In the analyses of all of our other data sets, we have used large, uniform priors on EFAC between 0.1 and 10.0. EFAC was originally implemented to account for instances when the profile data poorly matched the template profile in the TOA fit, which would underestimate the TOA uncertainty. In the present analysis, we expect EFAC to be near 1.0 because we are using evolving profile templates and have carefully excised RFI at a number of stages in the pipeline. We have found that allowing extreme EFAC values can inadvertently over or downweight subsets of the data when it is not justified. One reason for this is that there is a larger amount of covariance between EFAC and EQUAD parameters in the wideband analysis because the formal TOA uncertainties (of which there are far fewer) are more homoscedastic; EFAC and EQUAD parameters can only be differentiated if there is variance in the uncertainties. Equation (B3) describes how the EFAC and EQUAD parameters are related and affect the TOA measurement uncertainty. Therefore, we used a Gaussian prior on all EFAC parameters with a mean of 1.0 and standard deviation of 0.25; for similar reasons, we applied the same prior to DMEFAC parameters. This choice is further justified in Appendix A, where we show that the estimated TOA and DM uncertainties based on calculating the Fisher matrix of Equation (2) are accurate down to very low S/N. It should also be noted that these uncertainties, being based on the Fisher information matrix, are equal to the Cramér-Rao lower bound, which motivates the continued use of EFAC parameters. We use the same prior on EQUAD parameters as is used for both EQUAD and ECORR in NG12.5, which is a uniform distribution on $\log_{10}(\text{EQUAD [s]}) \in [-8.5, -5.0]$. Due to our use of nonuniform priors for EFAC and DMEFAC parameters, we refer to all point estimates from the noise modeling as maximum a posteriori (MAP) values, instead of maximum-likelihood values.

Red-noise priors—We use the exact same red-noise model and priors as in NG12.5, but because the determination of red-noise significance differs slightly from NG11 and NG9, and because it will be relevant in the discussion of results, we summarize it here. The red noise is assumed to be a stationary Gaussian process, which we parameterize with a power-law power spectral density P of the form

$$P(f_m) = A_{\text{red}}^2 \left(\frac{f_m}{1 \text{ yr}^{-1}} \right)^{\gamma_{\text{red}}}, \tag{5}$$

where A_{red} is the amplitude of the red noise at a frequency of 1 yr^{-1} in units of μs yr$^{1/2}$, and γ_{red} is the spectral index. The spectrum is evaluated at 30 linearly spaced frequencies f_m indexed by m, incremented by $1/T_{\text{span}}$, where T_{span} is the span

of the pulsar's data set. The prior on the red-noise amplitude is uniform on $\log_{10}(A_{\text{red}} \text{ [yr}^{3/2}]) \in [-20, -12]$, whereas the prior on the red-noise index has been constrained in both 12.5 yr analyses to be uniform on $\gamma \in [-7, -1.2]$. A pulsar is deemed to have "significant red noise" in these analyses if the Savage–Dickey density ratio (a proxy for the Bayes factor; Dickey 1971) estimated from the posterior distribution of $\log_{10}(A_{\text{red}})$ is greater than 100. Very low-index red noise is thought to primarily arise from imperfect modeling of various effects from the ISM (Shannon & Cordes 2017) and will be covariant with the white-noise parameters. Including shallow red noise instead of modeling it with only white-noise parameters will not significantly change the timing model. The analyses here and in NG12.5 are only indicative of the presence of red noise, which may or may not be wholly intrinsic to the pulsar; a comparison of the red-noise models is presented in Section 4.4.5. Advanced noise modeling of the 11 and 12.5 yr data sets, in which we explore bespoke models for each pulsar specifically in the context of GW analyses, is underway and will be presented elsewhere (J. Simon et al. 2020, in preparation).

Upon completion of the noise analysis, following the same protocol as in NG12.5, the MAP noise model is included as fixed parameters in the timing model, which is reoptimized using the generalized least-squares implementation of Tempo, now using the augmented, wideband likelihood. The large majority of the reduced chi-squared (goodness of fit) values fall between 0.9 and 1.1, with a few larger values. Some of these are to be expected because the additional DM data may not be particularly informative, or they may not be modeled well by DMX (e.g., see Section 4.3). As in NG12.5, we examined the significance of adding and removing various timing model parameters, but after finding no strong evidence favoring change, we kept the identical set of timing model parameters for ease of comparison. The differences with respect to crossing the significance threshold for including or excluding parameters are marginal and in several cases are a function of the difference in red-noise model (see Section 4.4.5).

The timing models are summarized in Table 5, which also lists the Bayes factor, B, indicating the significance of red noise. There is an analogous table in NG12.5 containing the results from the analyses of the narrowband data set. As mentioned in Table 2, we removed ASP and GASP TOAs that were taken simultaneously with concurrent PUPPI or GUPPI observations from the final TOA data sets. The final timing models with noise parameters, curated wideband TOAs, and related auxiliary files are the furnished products comprising this data release. We present the timing residuals and DM time series for these data in Appendix C, which includes visual comparisons with the counterpart averaged residuals and DMX models from NG12.5.

4. Results and Discussion

4.1. Average Portraits and Flux Density Measurements

A byproduct of the profile evolution modeling procedure is a calibrated high-S/N average portrait with a nominal profile alignment and full polarization information. The polarization portraits contain a wealth of information and are of interest to model in their own right; their models could potentially be used to improve the TOA measurement in cases of significant

Table 5
Summary of Timing Model Fits

Source	# of TOAs	# of Fit Parameters[a]					Rms[b] (μs)		Red Noise[c]			Figures
		S	A	B	DM	J	Full	White	A_{red}	γ_{red}	$\log_{10}B$	
J0023+0923	589	3	5	9	64	1	0.288	⋯	⋯	⋯	>2[d]	9
J0030+0451	488	3	5	0	190	2	2.868	0.200	0.006	−5.3	>2	10
J0340+4130	164	3	5	0	75	1	0.449	⋯	⋯	⋯	−0.20	11
J0613−0200	360	3	5	8	139	1	0.188	⋯	⋯	⋯	1.19[e]	12
J0636+5128	711	3	5	6	44	1	0.596	⋯	⋯	⋯	−0.07	13
J0645+5158	217	3	5	0	79	1	0.196	⋯	⋯	⋯	−0.17	14
J0740+6620	86	3	5	7	44	1	0.106	⋯	⋯	⋯	−0.15	15
J0931−1902	123	3	5	0	57	1	0.424	⋯	⋯	⋯	−0.16	16
J1012+5307	554	3	5	6	142	1	0.891	0.209	0.472	−1.3	>2	17
J1024−0719	230	4	5	0	100	1	0.240	⋯	⋯	⋯	0.36	18
J1125+7819	108	3	5	5	43	1	0.614	⋯	⋯	⋯	−0.09	19
J1453+1902	68	3	5	0	39	1	0.798	⋯	⋯	⋯	−0.10	20
J1455−3330	282	3	5	6	120	1	0.544	⋯	⋯	⋯	−0.13	21
J1600−3053	313	3	5	8	128	1	0.213	⋯	⋯	⋯	−0.09	22
J1614−2230	275	3	5	8	114	1	0.175	⋯	⋯	⋯	−0.23	23
J1640+2224	418	3	5	8	185	1	0.142	⋯	⋯	⋯	−0.16	24
J1643−1224	319	3	5	6	140	1	2.385	0.292	1.815	−1.2	>2	25
J1713+0747	1012	3	5	8	362	3	0.097	0.081	0.022	−1.6	>2	26
J1738+0333	269	3	5	5	77	1	0.272	⋯	⋯	⋯	−0.18	27
J1741+1351	147	3	5	8	73	1	0.148	⋯	⋯	⋯	−0.10	28
J1744−1134	347	3	5	0	134	1	0.721	0.278	0.220	−1.7	>2	29
J1747−4036	151	3	5	0	71	1	6.722	0.767	0.518	−3.8	>2	30
J1832−0836	120	3	5	0	58	1	0.195	⋯	⋯	⋯	−0.04	31
J1853+1303	134	3	5	8	70	1	0.322	0.092	0.139	−1.9	>2	32
B1855+09	313	3	5	7	123	1	1.387	0.322	0.045	−3.4	>2	33
J1903+0327	156	3	5	8	82	1	2.962	0.394	1.238	−2.2	>2	34
J1909−3744	550	3	5	9	221	1	0.337	0.058	0.025	−2.8	>2	35
J1910+1256	172	3	5	6	89	1	0.399	⋯	⋯	⋯	−0.16	36
J1911+1347	88	3	5	0	46	1	0.115	⋯	⋯	⋯	0.12	37
J1918−0642	379	3	5	7	133	1	0.296	⋯	⋯	⋯	−0.15	38
J1923+2515	119	3	5	0	66	1	0.237	⋯	⋯	⋯	−0.16	39
B1937+21	525	3	5	0	207	3	2.243	0.099	0.087	−3.5	>2	40
J1944+0907	138	3	5	0	72	1	0.375	⋯	⋯	⋯	−0.12	41
J1946+3417	78	3	5	8	41	1	0.143	⋯	⋯	⋯	−0.10	42
B1953+29	119	3	5	6	65	1	0.394	⋯	⋯	⋯	0.83	43
J2010−1323	278	3	5	0	108	1	0.250	⋯	⋯	⋯	−0.22	44
J2017+0603	127	3	5	7	74	2	0.097	⋯	⋯	⋯	−0.20	45
J2033+1734	90	3	5	5	46	1	0.520	⋯	⋯	⋯	−0.12	46
J2043+1711	316	3	5	7	148	1	0.122	⋯	⋯	⋯	1.70	47
J2145−0750	313	3	5	7	123	1	0.812	0.274	0.438	−1.6	>2	48
J2214+3000	233	3	5	5	77	1	0.419	⋯	⋯	⋯	0.21	49
J2229+2643	97	3	5	6	48	1	0.196	⋯	⋯	⋯	−0.16	50
J2234+0611	88	3	5	7	44	1	0.035	⋯	⋯	⋯	−0.15	51
J2234+0944	175	3	5	5	51	1	0.165	⋯	⋯	⋯	>2[d]	52
J2302+4442	174	3	5	7	75	1	0.693	⋯	⋯	⋯	−0.13	53
J2317+1439	505	3	5	6	209	2	5.416	0.204	0.001	−6.0	>2	54
J2322+2057	80	3	5	0	33	2	0.237	⋯	⋯	⋯	−0.10	55

Notes.
[a] Fit parameters: S = spin; B = binary; A = astrometry; DM = dispersion measure; J = phase jump (and an equal number of DM jumps).
[b] Weighted rms of postfit timing residuals. For sources with red noise, the "Full" rms value includes the red-noise contribution, while the "White" rms does not.
[c] Maximum-likelihood red-noise parameters: A_{red} = amplitude of red-noise power spectral density at $f = 1 \text{ yr}^{-1}$ with units μs yr$^{1/2}$; γ_{red} = spectral index; B = Bayes factor (">2" indicates a Bayes factor larger than our threshold $\log_{10}B > 2$, but which could not be estimated using the Savage–Dickey ratio).
[d] See text for additional details on this source.
[e] This source has significant red noise in the analysis of the narrowband data set.

polarization. For sufficiently polarized, large-bandwidth, high-S/N data, the rotation measure (RM) could be measured as part of the wideband TOA measurement. Such a development would combine the techniques summarized in Section 3.3 with those from van Straten (2006, 2013) and Osłowski et al. (2013), and is an active field of research.

We also estimated the phase- and frequency-averaged flux density for each of our PUPPI and GUPPI TOA measurements; ASP and GASP data were excluded because the profile data from which TOA measurements were made had been rescaled from their original flux calibration (see NG9 for details). The two main assumptions that go into the estimate and its formal,

statistical uncertainty are that the profile evolution model sufficiently describes the data (i.e., no model error) and that it has a correct baseline of zero flux density; all phases contribute to the measurement. The frequency-averaged flux density and uncertainty are calculated from the weighted mean of the phase-averaged flux densities. Because the scaling parameters a_n enter the calculation in the same way as for the S/N estimate, the flux density estimates may contain similar biases (see Appendix A). The relevant flags for these measurements are listed in Table 2, including a reference frequency for the flux density estimate. No additional sources of uncertainties are considered, and the interpretation of these measurements should be treated with caution.

4.2. Profile Evolution Models

We find that for the majority of our pulsars, the profile evolution model for a given receiver band requires a single eigenprofile (62 of 102 pulsar–receiver combinations), which can be thought of as the gradient of the mean profile. Most of the remainder required two (20 of 102) or zero (13 of 102; i.e., those data are consistent with a constant, nonevolving profile). The few cases in which more than three basis eigenprofiles are used to describe profile evolution arising in two very high-S/N pulsars (3 of 102 have three; the remaining four cases have more). B1937+21 shows spectral leakage from the overlapping, finite-attenuation filters used to subband the data,[48] which results in the increased number of eigenprofiles in three of its models, and the imperfect correction of the ADC artifact image described in Section 2 has the same consequence for one model for J1713+0747. Removing the perhaps spurious eigenprofiles for these pulsars does not appear to significantly change the timing results in Section 4, so we leave them for completeness. Furthermore, these two pulsars are observed with both observatories at the L band, and we find that the first two eigenprofiles (which contribute the most to profile evolution) are qualitatively the same between the models from each receiver.

Profile broadening from scattering in the ISM or other drastic, intrinsic profile evolution may be responsible for second and third eigenprofiles in the cases where either of those are detected. However, "incorrect" profile alignment with respect to a constant rotation proportional to ν^{-2} (corresponding to a small, constant DM offset, generally not larger than, but at most a few times, $\sim 10^{-3}$ cm^{-3} pc) may also be the culprit for additional eigenprofiles.

It is important to highlight that this subtle issue exists in the narrowband analysis as well; the implicit assumption there is perhaps the most parsimonious one, that the profile shape does not evolve with frequency, and that the profiles are aligned in phase. The choice of profile alignment sets the value of the absolute DMs measured and will not have an effect on the timing analyses, though a detailed study of this question is beyond the scope of this paper. More interesting questions about disentangling the profile evolution from ISM variations and possible magnetospheric effects are still open (Hassall et al. 2012). A possible future development in the context of the present work is to take a similarly parsimonious approach and simultaneously model profile evolution across all observed bands while minimizing the number of significant eigenprofiles

as a function of dispersive rotation. Furthermore, the underlying physical description of the observed profile evolution also warrants its own investigation.

One might expect a correlation between the total number of eigenprofiles for each pulsar and the number of FD parameters in the timing models from NG12.5. We see a rough correspondence between these two numbers, but its interpretation is dubious. For example, the FD parameters for B1855+09 (a.k.a. J1857+0943) from NG12.5 account for an approximate 20 μs delay across the profiles in its 430 MHz band, purportedly from unmodeled frequency evolution of the profile shape. Careful inspection reveals that its 430 MHz profiles show no evidence for profile evolution, neither in the number of significant eigenprofiles (zero) nor in the profile residuals after subtracting the model, nor by direct comparison of the profiles, whereas there is prominent profile evolution across the L-wide bandwidth. Even though the 430 MHz band is a factor of 3 lower in frequency than L-wide, the latter's narrowband TOAs will be more influential in DM estimation. This can be understood by the much larger fractional bandwidth of the L-wide receiver (see Table 1): although the dispersive delay across both receiver bands is comparable, the median raw wideband TOA uncertainty from L-wide is an order of magnitude more precise, and its median raw wideband DM uncertainty is $\sim$5 times smaller (see Figure 2). The spurious FD prediction may arise from the interplay between the relative weighting of the L-band and 430 MHz data in the DMX model, the covariance between FD parameters and DMX values, or perhaps something more interesting; most likely, the FD parameters are filling in for the role of DMJUMP, as mentioned in Section 3.5. The details are beyond the scope of this paper and are under investigation elsewhere.

4.3. Frequency-dependent DMs

For a handful of our highest-DM pulsars, the DM time series from each frequency band appear significantly different from one another. These trends are apparent in the panels second from the top in Appendix C for pulsars J1600−3053, J1643−1224, J1747−4036, and J1903+0327 (Figures 22, 25, 30, and 34, with DMs $\sim$ 52.3, 62.3, 153.0, and 297.5 cm^{-3} pc, respectively). It is also readily apparent in these panels, and in many other pulsars' DM time series, that the DM measurements are only significant after the switch over from the older generation of back-end instruments (ASP and GASP) to the newer ones (PUPPI and GUPPI) due to their ability to process a larger bandwidth in real time (see Table 1).

All four of these pulsars have clear pulse broadening in the form of frequency-dependent tails on the trailing edges of their profile components. To estimate the amount of scattering present in these pulsars, we decomposed their concatenated average portraits into a small number of fixed Gaussian components and an evolving one-sided exponential function (Pennucci et al. 2014). In this way, we estimated the scattering timescale τ at 1400 MHz for each of these four pulsars to be $\tau_{1400} \sim 26$, 52, 22, and 130 μs, respectively.

If the scattering timescale is changing with time and is not accounted for in the TOA measurement, the wideband DM measurements will be biased similarly as a function of time. As mentioned in Section 3.2, a forthcoming publication will present extensions to the wideband TOA measurement that will be better able to segregate time-variable profile broadening from classical DM variations (T. T. Pennucci et al. 2020, in

---

[48] We note that a better choice of filter appears to drastically improve this situation (Bailes et al. 2020).

preparation). The scattering timescale scales more steeply with frequency than does the dispersive delay (approximately, $\tau \propto \nu^{-4}$), and therefore the wideband DMs measured at lower frequencies will incur a greater bias, because the centroids of scattered pulse components shift by a greater amount. However, one expects that these biases, even if they are different in magnitude, will be correlated in time. Conditioned on that assumption, it is difficult to explain the DM time series of these pulsars arising solely from time-variable scattering. In all four instances, there are periods of correlation and anticorrelation between the DM time series measured in each frequency band.

This sort of behavior is, however, predicted by the phenomenon of "frequency-dependent DM" (Cordes et al. 2016), and very similar behavior has been seen in at least one other (canonical) pulsar (Donner et al. 2019; Lam et al. 2020), although earlier indications existed in B1937+21 (Cordes et al. 1990; Ramachandran et al. 2006; Demorest 2007) and in sparse multifrequency measurements of the highest-DM pulsar (Pennucci et al. 2015). The DM is defined as the path integral of the free-electron density sampled by a propagating electromagnetic wave. Due to the refractive nature of the ISM, the path will vary as a function of the frequency of the wave, and due to the density inhomogeneities in the ISM, the integrated density—the DM—will therefore also be a function of frequency. However, these differences are expected to be small, with rms values typically $\ll 10^{-3}$ cm^{-3} pc, and thus only high-precision observations (e.g., bright MSPs, or bright low-frequency sources) of high-DM pulsars over long periods of time are expected to convincingly show this phenomenon.

To substantiate the claim that the DM trends seen in these four pulsars may arise from this peculiar ISM effect, we can calculate the predicted rms difference between DMs measured at a fiducial frequency ν and a lower frequency ν', $\sigma_{\overline{DM}}(\nu, \nu')$, using Equations (12) and (15) of Cordes et al. (2016). Using our rough scattering timescales to estimate the scintillation bandwidths at ν, and using the appropriate frequencies for each pulsar, we find $\sigma_{\overline{DM}}(\nu, \nu') \approx 2$, 4, 2, and 3 $\times 10^{-3}$ cm^{-3} pc for J1600 −3053, J1643−1224, J1747−4036, and J1903+0327, respectively. These values are all within a factor of $\sim$2–3 of the rms differences measured in the observed DM time series: 0.6, 1.7, 2.8, and 5.9×10^{-3} cm^{-3} pc, respectively, where we only considered the PUPPI and GUPPI data for these measurements. Given that this quick assessment involves the assumptions that the density inhomogeneities in the ISM are Kolmogorov in nature, and that the scattering occurs in a single thin screen, we find this level of agreement suggestive. A more in-depth analysis is beyond the scope of this work, but these results indicate that long-term timing of high-DM MSPs in the context of PTA experiments offer a unique opportunity to study this phenomenon, as well as time-variable scattering; the low-frequency, high-cadence observations of CHIME/Pulsar are especially promising in these areas.

In the two largest-DM pulsars (J1747−4036 and J1903 +0327), there are obvious chromatic trends in the timing residuals from NG12.5 that are ameliorated in the wideband analysis. The narrowband noise analyses compensate for this by having larger white-noise parameters and slightly larger, shallower red noise, which helps to explain the timing improvements seen in the wideband data set. Similarly, because the ISM effects appear as apparently chromatic DM measurements in the wideband data set, the DMEFAC parameters are

larger than expected ($\sim$1.5–2.0). That is, the boilerplate DMX model may not be good representation of these data, even with DMEFAC and DMJUMP parameters, and more advanced DM and noise models are required.

In addition to these four pulsars, there are four more in our sample that have a DM $\gtrsim 50$ cm^{-3} pc: J0340+4130, B1937 +21, J1946+3417, and B1953+29 (a.k.a. J1955+2908; Figures 11, 40, 42, and 43, with DMs $\sim$49.6, 71.1, 110.2, and 104.5 cm^{-3} pc, respectively). None of their DM time series show the clear chromatic trends seen in the other four, but they all have some amount of additional variance that inflates their DMEFAC parameters. Using the measured scintillation parameters from Levin et al. (2016) for the three lower-DM pulsars and repeating similar calculations as above, we find that the rms differences predicted from Cordes et al. (2016) are much smaller ($\sim$an order of magnitude or more) than what is seen in the data. We could not find a published value for J1946+3417, so we estimated its scattering timescale by modeling its profile with Gaussian components in the same fashion as the first four pulsars and find $\tau_{1400} \sim 64$ μs. The predicted and observed rms DM differences are again similar, $\sim$4 and 2×10^{-3} cm^{-3} pc, respectively, and so frequency-dependent DM effects could also be playing a role here.

A couple of other well-timed pulsars with intermediate DM values show the same kind of extra DM variance (e.g., J0613 −0200; Figure 12, DM $\sim$38.8 cm^{-3} pc, and see also Section 4.4.5). Neither frequency-dependent dispersion nor time-variable scattering (in the form of profile broadening) appears to be playing a role here or in the three pulsars mentioned above. Another subtle effect may be at play in some of these pulsars, which is a manifestation of short-timescale variations referred to as "pulse jitter." Pulse jitter arises due to the fact that any finite collection of real single pulses will produce a mean profile with a slightly different shape and location between realizations, despite the long-term stability of the average profile (Helfand et al. 1975). For broadband observations that are significantly influenced by pulse jitter, the wideband DM estimate will be biased (see A. Parthasarathy et al. 2020, in preparation). Depending on the frequency dependence of pulse jitter (Lam et al. 2019), the bias may also be strongly frequency dependent. Alternatively, the "finite scintle effect," in which the relevant time-variable scattering effects occur in the strong diffractive regime (Cordes et al. 1990; Cordes & Shannon 2010), can have the same effect as pulse jitter and similarly bias the DM measurements. An investigation of the observed DM variance in some of our pulsars is beyond the scope of this paper, but it will play a role in considerations of future wideband data sets.

4.4. Comparison of Collective Timing Results

In this section, we give an overview of the wideband timing results by assessing the overall characteristics in comparison with the those found in NG12.5 and addressing a few pulsars individually. Besides those already mentioned and those that will be included in Section 4.5, specific interesting, astrophysical results from the 12.5 yr data set can be found in NG12.5; in particular, these include new or improved astrometric and binary timing model parameters. The timing residuals from both data sets are presented in Appendix C.

4.4.1. Timing Model Parameters
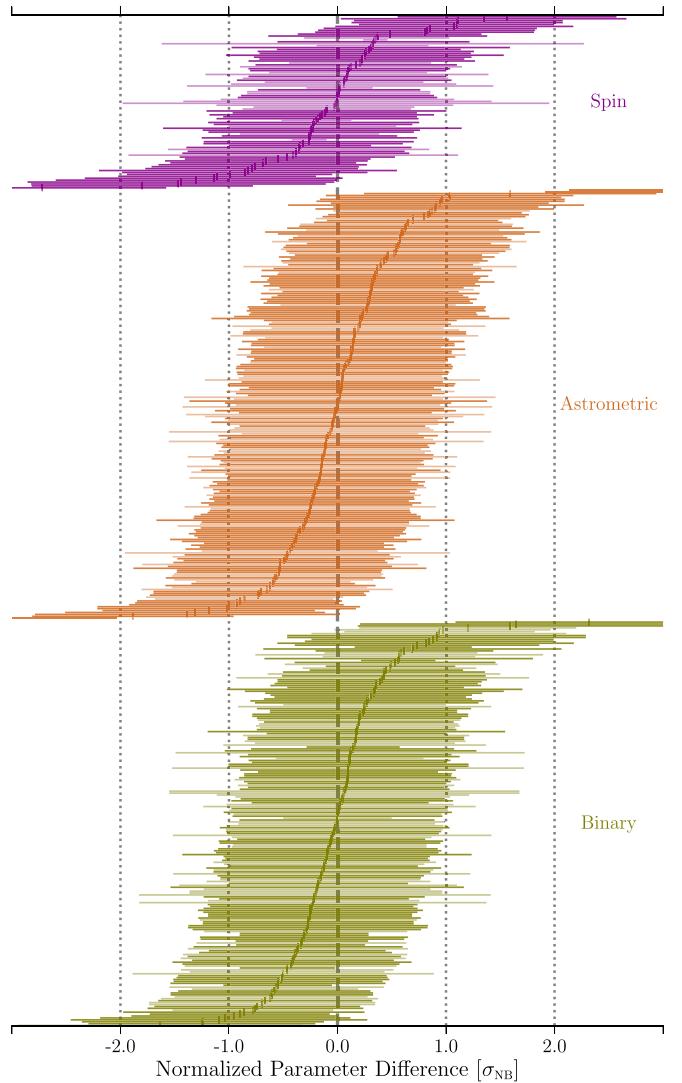
As mentioned in Section 3.5, the set of spin, astrometric, and binary timing model parameters used in our analyses is identical to that in NG12.5; the phrase "timing model parameters" used for the remainder of the text refers to this collection, excluding DMX parameters, which are compared separately. The ensemble of differences in these parameters is shown in Figure 3. The differences between parameter values are plotted, where each difference has been normalized by the parameter uncertainty from NG12.5 (σ_{NB}), and the "error bar" on each difference has a length equal to the ratio of parameter uncertainties, with the uncertainty from NG12.5 in the denominator (i.e., σ_{WB}/σ_{NB}). Such a convention allows us to discuss the relative differences we see in parameters and address their consistency without having to reference their absolute units. In the discussions that follow, we suppress the subscript on σ_{NB} and use the standalone symbol σ to refer to the units of these normalized differences. JUMP parameters are not included in Figure 3, as they are not meaningful, and parameters that reference an epoch were excluded if the epochs differed. Generally, this was not the case; 526 of 549 total parameters (96%), not including JUMPs or DMX parameters, were directly compared.

At a glance, we see that the timing model parameters are in very good agreement, almost entirely $<2\sigma$ different (99% of the parameters), and with very similar parameter uncertainties. The cases in which red noise is detected, or is detected in only one analysis, can be harder to interpret (these parameters are semitransparent in Figure 3); due to covariance with the MAP red-noise model, especially if the red noise is shallow, the parameter uncertainties can differ by a large factor. Only 1 of the 526 parameters (0.2%) is $>5\sigma$ away, while in total 4 (0.8%) are $>3\sigma$ away; for context, if these were independent experiments and we interpreted these differences as random samples from the unit normal distribution, we would "expect" ~ 0 deviations $>5\sigma$ and ~ 1 deviation $>3\sigma$. The only parameter larger than 5σ different is a known peculiarity in our data set (see Section 4.5.2). Two of the remaining three parameters with a difference larger than 3σ belong to J2234+0611, but also have larger uncertainties by $\sim 30\%$ (see Section 4.5.9). The last differing parameter is the parallax measurement of the black widow pulsar J2234+0944 (see Section 4.5.10). Nevertheless, the parameters agree remarkably well across the board, even in cases where red noise is detected.

4.4.2. DMX Parameters

We compare the mean-subtracted DMX model parameters in Figure 4, which has the same presentation as Figure 3. Of the 4,685 differences, 13 (0.3%) are $>5\sigma$ away (~ 0 "expected"), a total of 104 (2.2%) are $>3\sigma$ away (~ 6 "expected"), and 94% agree to better than 2σ. B1937+21 is responsible for 35 of the differences $>3\sigma$, which are due to the scatter in its DM measurements and the large influence they have on the DMX model (see Sections 4.3 and 4.5.6). Another 37 of these belong to the combination of J1713+0747 (see below), J1903+0327 (Section 4.3), and J2234+0944 (Section 4.5.10). The remaining 32 differences are distributed among 11 pulsars, for which we have no particular suspicions.
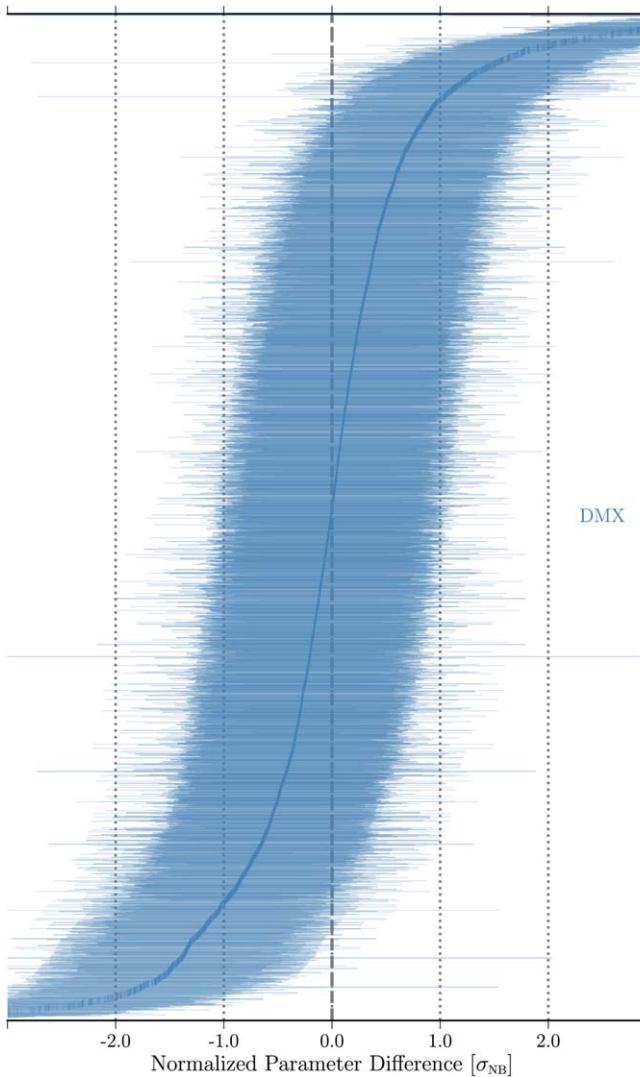
Besides the influence of differing red-noise models that was already mentioned, the FD parameters in the narrowband data set are covariant with all DMX parameters, which makes the

Figure 3. Snapshot comparison of 526 timing model parameters measured in the two data sets, divided into three main groups, each ordered by the normalized difference in parameter value. The parameter differences have been normalized by their uncertainties from NG12.5 ($\sigma_{NB} \equiv \sigma$), and "error bars" have a length $=\sigma_{WB}/\sigma_{NB}$. The more transparent points are parameters from timing models containing red noise in at least one analysis; due to covariance with, and small differences in, the MAP red-noise model (see Figure 7), these differences may be harder to interpret.

interpretation of the uncertainty ratios in Figure 4 difficult. Nevertheless, 92% of the DMX uncertainties agree to within a factor of 1.5, 99% agree to within a factor of 2, and the median DMX uncertainty for each pulsar is comparable between the data sets.

The number of DMX parameters often differs slightly between the data sets by one, two, or three parameters; there are 10, 6, and 4 such instances, respectively, with 26 pulsars having the same number of DMX parameters. The discrepancies in the number of DMX epochs arise from the slight differences in curating the data sets (Section 3.4). The exception to this is J1713+0747, where we opted to use a higher density of DMX bins during and after the second dip in its DM time series (Lam et al. 2018a), resulting in 37 additional DMX values; a similar binning exception is made for the same reason in NG12.5. However, this means the relevant DMX

Figure 4. Snapshot comparison of 4685 DMX model parameters measured in the two data sets, presented in the same manner as Figure 3. In addition to the effect of differing red-noise models between the analyses, the covariance present between DMX parameters and the FD parameters in the narrowband analysis may also skew the ratio of parameter uncertainties.

epochs in NG12.5 average over a greater span of time and will be biased in comparison to their counterparts here. The DMX time series are plotted in the topmost panels of the figures in Appendix C. In most instances, the DMX parameters from NG12.5 are hidden by those from the present analysis, demonstrating their close agreement.

4.4.3. Excess White Noise

A pulse TOA is a proxy for the moment a fixed point of longitude on the neutron star passes over the line of sight. There are a number of sources of uncertainty that obfuscate and bias the determination of this moment in time, even if the formal arrival time of the pulse can be very precisely determined. These additional uncertainties introduce either time-uncorrelated (white) scatter or time-correlated (red) trends into the timing residuals and can originate from a wide variety of sources local to the observatory, Earth, the solar system, the pulsar, or the intervening ISM. For thorough reviews of the sources of these uncertainties, we direct the reader to Verbiest

& Shaifullah (2018) and Cordes & Shannon (2010). Here, we compare the excess white noise seen in both data sets, followed by the red noise in Section 4.4.5.
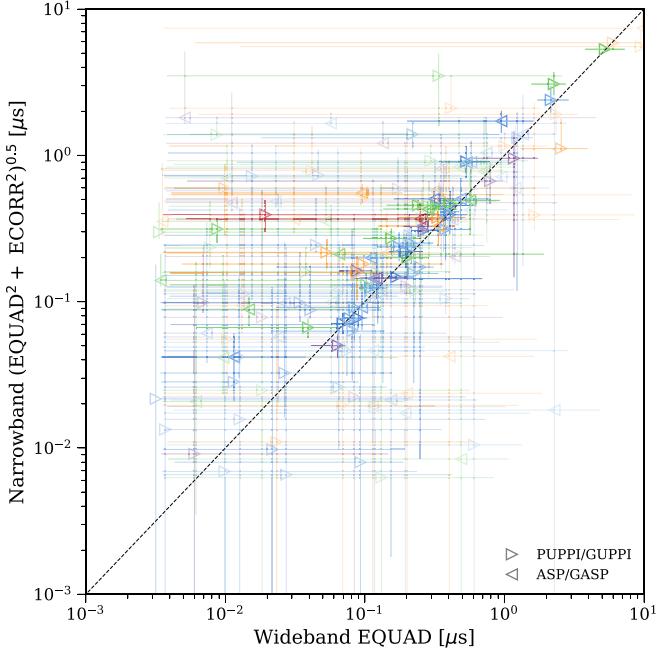
The formal TOA uncertainties are scaled in both analyses by EFAC parameters, which do not have a straightforward interpretation with respect to physical, excess noise; nominally, EFAC parameters account for misestimation of the system noise level or template-matching errors. Comparing the EFAC parameters is not very enlightening, particularly because the narrowband analysis uses fixed, nonevolving templates and uses a much broader prior on EFAC. The wideband analysis also uses DMEFAC parameters, which can absorb some excess noise that might be modeled by EFAC in the narrowband analysis. As mentioned in Section 3.5, there is a difference between the two analyses in how white noise is modeled in the timing residuals. EQUAD and ECORR parameters capture the additional variance in the narrowband analysis, but because ECORR accounts for fluctuations that are completely corre-lated for simultaneously obtained measurements (i.e., narrow-band TOAs), it cannot be differentiated from EQUAD in the wideband analysis and is therefore left out of the noise model.

To effectively compare the white noise, we plot the MAP EQUAD parameters from our analyses against the quadrature sum of the corresponding maximum-likelihood EQUAD and ECORR parameters in Figure 5. In the figure, points appear more opaque in proportion to how constrained the posterior distribution of the parameter is. There is a clear correspondence over two orders of magnitude in the white-noise parameters, suggesting that both analyses see very similar white noise.

Although the integrated pulse profile shapes of MSPs are secularly stable (Brook et al. 2018, with some exceptions, e.g., Shannon et al. 2016), they vary minutely (indeed) on short timescales due to pulse jitter (see Section 4.3). Pulse jitter contributes additional uncertainty to the TOA and is expected to manifest in ECORR parameters, though the measured ECORR values exceed the predicted level of jitter (Lam et al. 2016b). Jitter is thought to be weakly or modestly dependent on frequency (Shannon et al. 2014; Lam et al. 2019), and its effects can only be reduced by longer integration times or actively accounting for shape change (Osłowski et al. 2011). On the other hand, the various ISM effects that can contribute to EQUAD have a stronger (and mostly pulsar-independent) frequency dependence. From this perspective, analyzing narrowband TOAs may help to discriminate between sources of excess white noise, although using evolving profile templates would be an improvement to the overall approach. In this way, both forms of analysis may contribute to arriving at the best results for a given pulsar. For example, if some of our MSPs have large white noise because of time-variable scattering, then the pulse broadening can be included as part of the wideband TOA measurement.

4.4.4. rms Timing Residual

A second metric for gauging the overall level of noise is the rms timing residual (see Table 5). In Figure 6, we compare the rms values between the two analyses, taking care to use the averaged residuals from the narrowband data set and the whitened set of residuals whenever red noise was detected in either of the analyses. Almost no pulsars differ by more than a factor of 1.5, with a number of exceptions explained as part of Section 4.5, and half of them agree to within a factor of 1.1. However, the rms residual from either analysis can be very
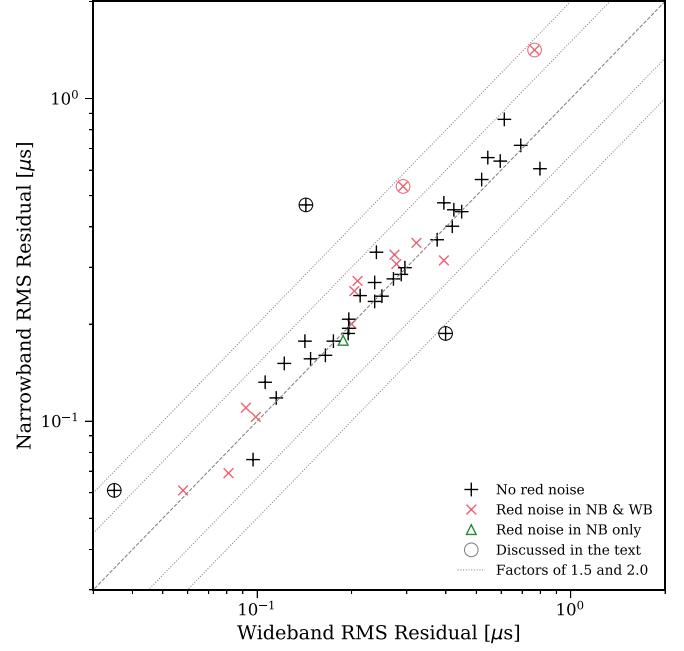
Figure 5. Comparison of excess white noise seen in the two data sets. Each symbol demarcates a single combination of pulsar, receiver, and back-end instrument; the symbol direction indicates the back end, whereas the colors indicate the receiver as in Figure 1: 327 MHz (red), 430 MHz (orange), 820 MHz (green), 1.4 GHz (lighter blue for AO, darker blue for the GBT), and 2.1 GHz (purple). As ECORR parameters are not part of the wideband noise model, the quadrature sum of maximum-likelihood estimates for the narrowband EQUAD and ECORR parameters is plotted against the corresponding wideband MAP EQUAD estimate. The central 95% interval of each parameter's posterior is shown as a superimposed horizontal or vertical line (the smaller of the EQUAD and ECORR intervals was chosen for each narrowband value). The transparency of the symbols is a proxy for the mutual significance of the parameter: the smaller the combined intervals, the more opaque the marker. In this way, a clear correlation is brought out, suggesting similar white noise is seen in both analyses.

Figure 6. Comparison of the timing residuals' weighted rms values between the two data sets. The rms of the "whitened" residual is plotted in all applicable cases; the values are given in Table 5. Encircled pulsars are addressed as part of Section 4.5; in increasing order of their wideband timing rms, these are J2234+0611, J1946+3417, J1643−1224, J1910+1256, and J1747−4036.

sensitive to the exact noise model, which is fixed in the final optimization of the timing model. The noise analyses explore the logarithm of the EQUAD, ECORR, and red-noise amplitude parameters, so small statistical deviations in the best-fit parameters arising from the Monte Carlo analysis can lead to rather different rms values. The rms should be thought of as a random variable, whose variance is influenced by the posterior distributions of the noise parameters. This is true even when the noise-model parameters are constrained, and it underscores the need for advanced noise-modeling techniques. Nevertheless, it is encouraging that 31 of the 47 pulsars show some amount of improvement and that all but five pulsars have rms residuals no more than ∼10% larger than their narrowband counterparts.

4.4.5. Detection of Red Noise

A final, and perhaps most crucial, litmus test for the wideband analyses is the detection of red noise in individual pulsars. Obviously, the presence of red noise in the wideband data set (or lack thereof), in relation to what is seen in the narrowband data set, guides our expectations of full-scale GW analyses, which heretofore have only been vetted on our narrowband data sets. We introduced the red-noise model in Section 3.5; there are additional details in Appendix B,

NG9, NG11, and NG12.5. Here we discuss our findings in contrast to those from the narrowband analysis.

In Figure 7, we show the significantly detected power-law red noise in our analyses compared to those from NG12.5. We again find the level of agreement between the data sets reassuring. Recall from Section 3.5 that a pulsar is deemed to have "significant red noise" if the estimated Bayes factor is above 100 (see Table 5 for Bayes factors). Thirteen pulsars have detected red noise in both analyses, one pulsar has significant red noise detected in just the narrowband analysis (J0613−0200), and two black widow pulsars, which are not shown in the plot, are treated differently and not discussed further here (J0023+0923 and J2234+0944; see Section 4.5.10). Ten of these pulsars (plus J1713+0747) had detected red noise in NG11; J1744−1134, J1853+1303, and J2317+1439 are new detections in NG12.5, which all have significant red noise here.

It is thought that unmitigated ISM effects can manifest as shallow-spectrum red noise (Foster & Cordes 1990; Rickett & Lyne 1990; Cordes & Shannon 2010; Shannon & Cordes 2017), which we indicate in Figure 7 for $\gamma_{\text{red}} > -3$. J0613−0200's DM is in the top third of our sample ($\sim 38.8\,\text{cm}^{-3}\,\text{pc}$, respectively) and has fairly shallow red noise in its narrowband analyses. Red noise is only marginally favored in its wideband analysis, as indicated by the Bayes factors of ∼15 in Table 5. When red noise is included in the wideband analysis (the dashed–dotted lines in Figure 7), the MAP model has the same index as, a slightly smaller amplitude than, and similar white-noise parameters to NG12.5. Without red noise, the corresponding wideband white-noise EQUAD parameters are statistically unchanged. This suggests that the wideband analysis might be able to mitigate some of the ISM-induced red noise.

Figure 7. Comparison of the significantly detected power-law red-noise parameters in the two data sets; measurements from the wideband data set (red) are plotted below those from NG12.5 (blue). Pulsars are ordered top to bottom by highest to lowest red-noise amplitude seen in the wideband data set, and the large symbols represent the MAP parameter estimates: squares indicate the logarithm of the amplitude at a frequency of 1 yr^{-1} (dual units shown) and diamonds represent the power-law index. The central 95% of the marginalized posterior distribution for each parameter is shown as a line with a tick indicating the median. One pulsar (J0613 −0200) has above-threshold red noise in the narrowband analyses, but not in the wideband analysis; we nevertheless indicate its MAP values and posterior distribution intervals (with dashed–dotted lines) when red noise is included in the modeling. The apparent correlation between red-noise amplitude and index is in part due to the parameterization of referencing the amplitude to a frequency of 1 yr^{-1}. Unmitigated ISM effects are thought to induce fluctuations with a spectrum having a characteristic index lying within the darker gray region ($\gamma_{red} > -3$; see Shannon & Cordes 2017). The lighter gray region is the prediction for intrinsic spin noise across a broad pulsar population from Lam et al. (2017), $\gamma_{spin} = -4.46 \pm 0.16$, although the scatter in the relation is substantial. We indicate with vertical lines the fiducial index for the stochastic background of gravitational waves and our most recently published 95% upper limit for its amplitude, from the 11 yr data set (Arzoumanian et al. 2018a); this limit accounts for both interpulsar correlations and uncertainties in the solar system ephemeris.

Intrinsic spin noise in pulsars has been modeled in the literature as a random walk in phase, frequency, or frequency derivative, with corresponding power spectral indices of −2, −4, and −6, respectively, as well as arising from chaotic behavior (e.g., Harding et al. 1990). The lighter gray region in Figure 7 represents the best-fit index ($\gamma_{spin} = -4.46 \pm 0.16$) for timing noise seen across pulsars of all types from Lam et al. (2017), consistent with a mixture of random walks (e.g., Cordes & Downs 1985; D'Alessandro et al. 1995). The scatter in this best-fit relation, however, is large enough to essentially cover the range of observed spectra. It is therefore difficult to interpret the spread of red noise we have detected, particularly because we suspect that some of the pulsars with shallow red noise are dominated by contributions from the ISM, whereas others may have a mix of contributions. Coexisting with the red noise intrinsic to the pulsar and that from the ISM, there is a contribution from the background of stochastic, low-frequency GWs, which is thought to have a steep power-law index ($\gamma_{GWB} = -13/3$; Phinney 2001; Jaffe & Backer 2003), indicated by a dotted vertical line in the figure. For scale, the dashed vertical line indicates the 95% upper limit on the amplitude of the GW background from analyzing the 11 yr data set (Arzoumanian et al. 2018a). A more recent search for the

stochastic GW background in the 12.5-year narrowband data set is presented in Arzoumanian et al. (2020).

4.5. Additional Discussion of Individual Pulsars

The results from a number of pulsars, some of which have been previously mentioned, deserve additional comments, caveats, or emphasis, which we detail here. In addition, for the simple purpose of highlighting one example of generally good, comprehensive agreement with the narrowband results, and one example of where perhaps wideband timing did not prove beneficial, we direct the reader to J0931−1902 and J1910+1256, respectively.

4.5.1. J0931−1902

J0931−1902 has the distinction of having the largest fractional difference between the number of pulse profiles used in the wideband analysis and the number of TOAs in the narrowband analysis; its wideband data set makes use of 81% more profiles (see Table 3). Again, this difference arises because of the S/N threshold used in the narrowband analysis; because this pulsar is fairly weak and scintillates, a large number of its low-S/N profiles get individually discarded in the narrowband analysis, even though they combine to yield useful wideband TOAs. J0931−1902 is the second worst

pulsar in our data set in terms of raw *L*-band timing precision (see Figure 2), but is somewhere in the middle in terms of rms (∼ 440 ns in both data sets). There is absolutely nothing else different about its results from the narrowband analysis— except that its timing model parameters are all ∼15% more precise in the wideband analysis. At least two other pulsars— J0340+4130 and J0740+6620—show this level of improvement that is most likely attributable to a similar explanation, although their differences in data volume are not extreme. These improvements underscore the benefit of using the wideband TOA approach for salvaging all information contained in less bright or scintillating pulsars.

4.5.2. J1640+2224

The difference in J1640+2224's ecliptic longitude is the lone culprit referred to earlier for being very different (∼6σ) from its counterpart in the narrowband analysis. However, this is a known anomaly to us, albeit of unknown origin; we have previously compared timing results from different timing software using the exact same data sets, and J1640+2224's ecliptic longitude was the single outlier to be significantly different (see also the comparison between Tempo and PINT Luo et al. 2019 in NG12.5). The published position from Very Long Baseline Interferometry (Vigeland et al. 2018) is not precise enough to discern between the two measurements. However, it should be noted that the value from NG12.5 is better than 1σ consistent with the extrapolated value from NG11, whereas the value from the wideband analysis is ∼2σ consistent with the extrapolated value from NG9. Fonseca et al. (2016) followed up on NG9 and suspected that J1640+2224 is a massive neutron star (see also Deng et al. 2020); the improvements on the mass measurements will be presented elsewhere.

4.5.3. J1643−1224

We have already discussed J1643−1224 at some length in Section 4.3. It is worth emphasizing, though, that some of the complexity and chromatic dependence seen in the DM measurements and timing residuals of this pulsar almost certainly arise from the fact that it lies directly behind the H II region Sh 2–27 associated with ζ Ophiuchi (Ocker et al. 2020). This association may also be responsible for a protracted decrease in its flux density (Maitia et al. 2003). In addition to the confounding factors of the ISM, at least one intrinsic profile shape change event is thought to have occurred in this pulsar around 2015 February (Shannon et al. 2016). Although we see the corresponding discrete perturbation in J1643−1224's timing residuals at this time, the follow-up analysis by Brook et al. (2018) on our 11 yr data set argues that ISM effects cannot be ruled out. The ∼45% improvement in its rms timing residual seen in Figure 6 is almost certainly a result of the mitigation of the chromatic structure in its residuals; see the discussion at the end of Section 4.3.

4.5.4. J1747−4036

Similarly, we have already discussed J1747−4036 in Section 4.3. J1747−4036 also stands out in Figure 6, with the same level of improvement in rms residual as J1643−2224 due to the mitigation of chromatic structure in the timing residuals.

4.5.5. J1910+1256

J1910+1256 has a significantly worse rms wideband timing residual in Figure 6, by just over a factor of 2. We find a significant *L*-band EQUAD detected in the wideband analysis, whereas the posterior distributions for the *L*-band EQUAD and ECORR are consistent with upper limits. Interestingly, the white-noise parameters for the *S* band are significantly measured in both analysis and are of similar amplitude. J1910+1256 is in the top 10 pulsars by raw *L*-band timing precision (Figure 2), with the median *L*-band PUPPI TOA having a precision just above 100 ns; the MAP PUPPI *L*-band EQUAD is more than three times larger. The source of this discrepancy has not been determined, but despite the difference, the timing model parameters are no more than ∼10% worse than their narrowband counterparts.

4.5.6. B1937+21

B1937+21 (a.k.a. J1939+2134) presents a special set of challenges for the wideband analysis, being the brightest pulsar in the data set with the smallest formal measurement uncertainties by a considerable margin (see Figure 2). As mentioned in Section 3.3, its profile modeling is contaminated by spectral leakage because it is so bright, although we do not believe this meaningfully affects the timing results. As mentioned in Section 4.3, it has a substantial amount of scatter in its wideband DM measurements once the long-term trend is removed; this results in the highest DMEFAC parameters in the data set as well as the worst goodness-of-fit value for its timing model, due to the additional contribution from the DM model. The restrictive Gaussian prior (see Section 3.5) inhibits the DMEFAC parameters from taking even larger values, which would encapsulate more of the variance in the DM time series. Relaxing the prior is not physically motivated, and so these results direct us to implement an additional DM model parameter in future analyses, one that is analogous to the standard EQUAD parameter. Given that both pulse jitter and variable diffractive interference in the ISM (i.e., the "finite scintle effect") play a roll in the observations of this pulsar (Lam et al. 2019), it is feasible that both effects serve to bias the wideband DM estimates, resulting in extra variance in the DM time series. Despite the additional variance in the wideband DM time series, the astrometric timing model parameters are in very good agreement (<1σ) with similar uncertainties.

4.5.7. J1946+3417

J1946+3417 is one of the two new pulsars in this data set, which has already been discussed in Section 4.3 due to it having the third largest DM in the data set (∼110.2 cm⁻³ pc). It has the distinction of showing the single largest difference in rms in either direction, seen in Figure 6; the wideband rms timing residual is a factor of 3 smaller. Both analyses examine the same amount of data and the wideband raw timing precision is ∼10% better (see Table 4 and the equivalent table in NG12.5). The Bayes factor for red noise in the narrowband analysis is ∼59, whereas it is not at all favored in the wideband analysis. The preferred red-noise model is large and shallow, and as a result of it not being included, the narrowband white-noise parameters are larger than their wideband counterparts. The timing model parameters agree to ⩽1σ, but with ∼10% larger uncertainties in the wideband analysis. It should also be noted that J1946+3417 is an astrophysically interesting source,

as it is one of the few eccentric binary MSPs in the field and also contains a massive neutron star (Antoniadis 2014; Freire & Tauris 2014; Jiang et al. 2015; Barr et al. 2017, all of which also make note of J2234+0611).

4.5.8. J2043+1711

J2043+1711 has the highest subthreshold Bayes factor in Table 5, $B \sim 50$. In repeated analyses, the statistic B was noisy enough to sometimes cross our significance threshold. The narrowband analysis also favors red noise, but with a lower Bayes factor ~ 26. The difference between the analyses may arise from the amount of data examined. As can be seen in Table 3, J2043+1711's wideband data set is $\sim 70\%$ larger than its narrowband counterpart, the third largest difference, which is due to its scintillation characteristics combined with the S/N ratio cutoff in the narrowband analysis. J2043+1711 has a fairly low DM (~ 20.8 cm^{-3} pc), a timing baseline of six years and, importantly, it has been included in our high-cadence observations at Arecibo since 2015, which has increased its data volume by $\sim 70\%$ since the 11 yr data set. The narrow features in its profile enable this pulsar to be timed very precisely when it is detected (see Tables 4 and 5, and Figure 2), and so we expect the emerging red noise in this pulsar to be significantly detected in the near future.

4.5.9. J2234+0611

At face value, J2234+0611 is the best-timed pulsar in the data set: the narrowband and wideband timing rms values are ~ 60 and 35 ns, respectively (Figure 6), with no preference for red noise in either analysis. This is partially due to it only having a timing baseline 3.4 yr in length, although it is in the top 10 pulsars by raw L-band timing precision. Both analyses detect excess white noise, although the wideband analysis measures a significantly larger EQUAD in the 430 MHz band; this results in an overweighting of the wideband L-band data, which may explain the significantly smaller rms value. We make special mention of this pulsar also because it stands out for its level of disagreement in its timing model parameters with NG12.5, as mentioned in Section 4.4.1. All of its wideband timing model parameters have uncertainties larger by $\sim 30\%$–40%, but no other pulsar shows quite this level of disagreement. Its ecliptic latitude and parallax measurements are $\sim 3.5\sigma$ different from their narrowband analysis counterparts. The fact that J2234+0611 has a relatively short timing baseline but has significantly measured secular binary parameters is a testament to its timing precision. In fact, additional modeling of its binary orbit is necessary, which was carried out in Stovall et al. (2019) with an additional 1.5 yr of data, most of which were NANOGrav observations collected beyond the cutoff of the present data set. Along with the Shapiro delay and annual orbital parallax, Stovall et al. (2019) were able to determine the 3D orbital geometry of the binary. We are confident that the discrepancies seen here will be resolved with the implementation of the Stovall et al. (2019) timing solution in future data sets.

4.5.10. J2234+0944

J2234+0944 was previously mentioned in Sections 4.4.1, 4.4.2, and 4.4.5. This pulsar is one of four black widow pulsars in the data set (along with J0023+0923, J0636+5128, and J2214+3000), and one of two (along with J2214+3000) that

do not show orbital or secular variability according to Bak Nielsen et al. (2020), who studied three of these systems over ~ 8 yr baselines (J0636+5128 was not part of their study). This pulsar has a very significantly detected "red noise" in the wideband analysis, but no indication of it in the narrowband analysis, according to the Bayes factors in Table 5 and its analog in NG12.5. However, this "red noise" is specious; the preferred model is extremely shallow and the power-law fit to the function in Equation (5) is dominated by the frequencies higher than 1 yr^{-1}, reflecting the short timing baseline ($T_{span} \sim 4.0$ yr). Based on this reasoning, we exclude the red-noise component from J2234+0944's analysis; we similarly excluded the "red noise" seen in J0023+0923 for the same reason. The origin of the excess noise seen in the wideband data set is not known; it could be a sign of variability (Torres et al. 2017), but the findings of Bak Nielsen et al. (2020) refute this. Interestingly, the black widow J2214+3000 had a very similar issue in NG11, when it had a similar timing baseline, which was resolved with the additional data in this data set and a reparameterization of its timing model. Finally, NG12.5 reports that the parallax measurement is no longer significant, in contrast to NG11; this loss of significance in NG12.5 is marginal and not the case in the wideband analysis. Despite being $\sim 3\sigma$ different from NG12.5, J2234 +0944's parallax is significantly measured and is $<1\sigma$ consistent with the value from NG11.

5. Summary and Conclusions

In this paper, we have demonstrated the promise of wideband data sets for the purpose of high-precision pulsar timing and GW experiments with PTAs. Specifically, we reprocessed the pulse profiles from the 47 MSPs comprising the NANOGrav 12.5 yr data set using "wideband" methods, produced a parallel data set,[49] and compared the results with those presented in NG12.5. Our wideband framework employed an innovative, compact modeling of pulse profile evolution, extracted simultaneous TOA and DM measurements from broadband pulsar observations, and analyzed the data using novel developments in our Bayesian noise models and timing software.

The broad agreement in results spans a variety of metrics, from timing residuals, timing model parameters, and DM time series, to white- and red-noise-model components. In many of the simplest cases, the wideband timing results are at least on par with their narrowband counterparts, and often times show indications of improvements (e.g., J0931−1902, J1125+7819, J2043+1711). In other cases, complexities point toward favoring one kind of analysis over the other, or toward an unresolved discrepancy with perhaps interesting results (e.g., J1910+1256, J1946+3417, J2234+0944).

We gain the most assurance from the congruence of results for our most important, best-timed pulsars, and from the concurrence in all red-noise models. For example, for J1909 −3744 and J1713+0747, all but one of their timing model parameters agree to within 1σ (the last to within 1.5σ), with very similar parameter uncertainties, and nearly the same form of detected red noise. In the case of J1713+0747, considering that its noise model included 30 parameters—12 of which belong to two types of newly implemented parameters—and

---

[49] Both data sets are available at data.nanograv.org.

that its TOA volume was reduced by a factor of 37, we find this level of agreement remarkable.

Our most significant results include:

1. Better than 2σ agreement for the large majority (99%) of timing model parameters (Section 4.4.1) and better than 3σ in all but four of them; 98% of DMX parameters agree to better than 3σ (Section 4.4.2).
2. Consistently detected red noise for 13 of the 14 pulsars in NG12.5 (Section 4.4.5).
3. Very similar timing residuals and DMX time series (Appendix C), comparable or improved rms timing residuals for 31 of the 47 pulsars, with virtually all of them agreeing within a factor of 1.5 (Section 4.4.4).
4. Recovery of low-S/N profile data (Appendix A), leading to a larger profile data set by 16% and more precise timing model parameters in several pulsars (Section 4.5).
5. Indications of frequency-dependent DMs in at least four MSPs and significant variance in the DM measurements in others (Section 4.3).
6. Per-observation mean flux density measurements (Section 4.1).
7. Wideband developments to the `ENTERPRISE` and `Tempo` software packages (Appendix B).
8. A reduction in the TOA volume of the 12.5 yr data set by a factor of 33, and an overall reduction in data volume (once including the DM measurements) by a factor of 16 (Table 3).

The reduction in the data set volume is a particularly important development because PTA experiments are maturing and are well into their second decade of operation; as a result, they have burgeoning facilities, an increasing number of pulsars, growing bandwidths, and, therefore, an exploding number of TOAs. However, additional developments will need to be made if we are to realize some of the sought-after significant computational speed-ups by moving to wideband data sets. Nevertheless, wideband techniques offer a number of avenues for tackling problems related to profile evolution, the ISM, and broad-bandwidth observations.

It very well may be that choosing between wideband and narrowband approaches is a pulsar-dependent question and that some of the advantages that come with retaining frequency-resolved TOAs can aid in making new advances or analyzing wideband measurements. In all cases, conventional narrowband analyses ought to adopt frequency-dependent profile templates, which would also facilitate a shared framework in which the methods operate. We note, however, how to optimize a PTA experiment is still an open question, particularly with respect to scheduling and selecting frequencies and bandwidths with which to time individual pulsars (e.g., Lee et al. 2014; Lam 2018; Lam et al. 2018b). Ultrawideband receivers and simultaneous multiband observations are becoming norms in pulsar timing, and along with the anticipated increase in cadence (for which CHIME is the archetype), we anticipate wideband timing techniques to follow closely behind. In the mean time, we will make new improvements to the wideband strategy, some of which we have already mentioned. These include incorporating polarization information into the wideband TOA measurement, accounting for additional time-variable effects from the ISM, implementing Gaussian processes to model our DM measurements, and developing the `PINT` timing software package (Luo et al. 2020) for full compatibility with wideband data sets.

The final test for our wideband data set will be to analyze it for GWs. Arzoumanian et al. (2020) find strong evidence for an unidentified common-spectrum stochastic process across pulsars in the narrowband data set, and early analyses indicate we should expect similar results from the wideband data set; we will present that investigation elsewhere. The NANOGrav 12.5 yr data set represents a milestone in part because it lays the groundwork for future wideband data sets, which will meet the challenges posed by PTA experiments.

Author contributions

The alphabetical-order author list reflects the broad variety of contributions of authors to the NANOGrav project. Some specific contributions to this paper, particularly those that overlap with and are in addition to NG12.5, which made this project possible, are as follows. T.T.P. was responsible for the research, development, implementation, computation, analysis, and write-up of this work, contributing significantly to all aspects. P.B.D. and M.V. developed the formal wideband timing likelihood. P.B.D. and T.T.P. made necessary developments to `Tempo`. M.V. and T.T.P. made necessary developments to `ENTERPRISE`. M.E.D. coordinated the development of the primary 12.5 yr data set, was its

---

[50] https://github.com/demorest/tempo_utils

primary lead, coauthored observing proposals, and coordinated the observations at the Arecibo Observatory. M.T.L. designed the original `Python` notebook analysis pipeline, which was repurposed by T.T.P. for these analyses. P.B.D. wrote observing proposals, performed calibration and data reduction, coordinated data management, developed and implemented the methodology used to mitigate the artifact images in the data, and advised closely about this research. E.F. wrote observing proposals and assisted in the coordination of Arecibo observations. P.B.D. and K.S. coordinated GBT observations. S.M.R. provided computational facilities for this work. P.T.B., H.T.C., J.M.C., P.B.D., T.D., D.L.K., M.T.L., C.M.F.M., D.J.N., and M.V. contributed directly to portions of the manuscript. B.J.S. and J.S.H. contributed to the analysis concerning B1855+09. N.G.D. oversaw and maintained much of the computational infrastructure related and essential to this work, which included regularly updating software and maintaining the servers where data and analysis pipelines are hosted. The NANOGrav Timing Working Group advised about all stages of the analyses; D.J.N. served as its chair during the development of the 12.5 yr data set. Z.A., H.B., P.T.B., H.T.C., M.E.D., P.B.D., T.D., R.D.F., E.C.F., E.F., P.A.G., M.L.J., M.A.L., D.R.L., R.S.L., M.A.M., C.N., D.J.N., T.T.P., S.M.R., K.S., I.H.S., J.K.S., R.S., S.J.V., and W.Z. each ran at least 10 sessions and/or 20 hr of observations for this project. M.F.A., K.E.B., K.C., R.S. C., R.L.C., W.F., Y.G., D.H., C.J., K.M., B.M.X.N., J.R., and M. T. were undergraduate observing-team leaders, supervised by F.C., T.D., D.L.K., and J.K.S. P.T.B., P.B.D., M.E.D., M.T.L., J.L., M. A.M., T.T.P., and K.S. developed and refined procedures and computational tools for the timing pipeline. H.B., P.R.B., H.T.C., M.E.D., P.B.D., E.F., D.C.G., M.L.J., M.T.L., M.A.M., D.J.N., N. S.P., T.T.P., S.M.R., I.H.S., and K.S. generated and checked timing solutions for individual pulsars in NG12.5, which became the starting point for the analyses performed here.

Appendix A
Low-S/N Wideband TOAs

Here we justify the empirically determined S/N thresholding applied to the wideband TOA data set described in Section 3.4 and listed in Table 2. We follow an analogous analysis as Appendix B of NG9 in which a similar justification was made for excluding all narrowband TOAs with S/N < 8, a practice that continued in both NG11 and NG12.5. The main reason for excluding these data is that the TOA probability distribution function (PDF) at low S/N becomes very non-Gaussian, gains heavy tails, and approaches a uniform distribution as the noise level becomes comparable to the amplitude of the pulse.

Using the frequency-dependent notation introduced in Section 3.2, we define the "per-channel" S/N in a wideband TOA as

$$S_n \equiv a_n T_n / \sigma_n, \tag{A1}$$

where $T_n \equiv \sqrt{\sum_k |t_{nk}|^2}$, t_{nk} is the DFT of the template profile with frequency index n and Fourier harmonic index k, a_n is the scaling amplitude, and σ_n is the noise level in t_{nk}. This equation is the same form as the conventional, narrowband TOA S/N given in NG9 for each channel's matched template, but which is subject to the constraint in Equation (3). With this definition in hand, we can immediately write down the joint PDF of a wideband TOA ($\phi_\circ$) and DM as a function of S/N, which will be independent of any particular, noisy realization of data. This PDF has the same form as Equation (13) from NG9, but now

contains a sum over frequency channels (indexed by n),

$$p(\phi_\circ, \mathrm{DM}) \propto \exp\left(\sum_n \frac{S_n^2}{2} \frac{C_{tt,n}^2(\phi_n)}{T_n^4} \right), \tag{A2}$$

where $C_{tt,n}$ is the template autocorrelation as a function of $\phi_\circ$ and DM, via ϕ_n (Equation (3)). $C_{tt,n}$ is normalized such that $C_{tt,n}(\phi_n = 0) = T_n^2$, which explains our definition of the wideband TOA S/N as
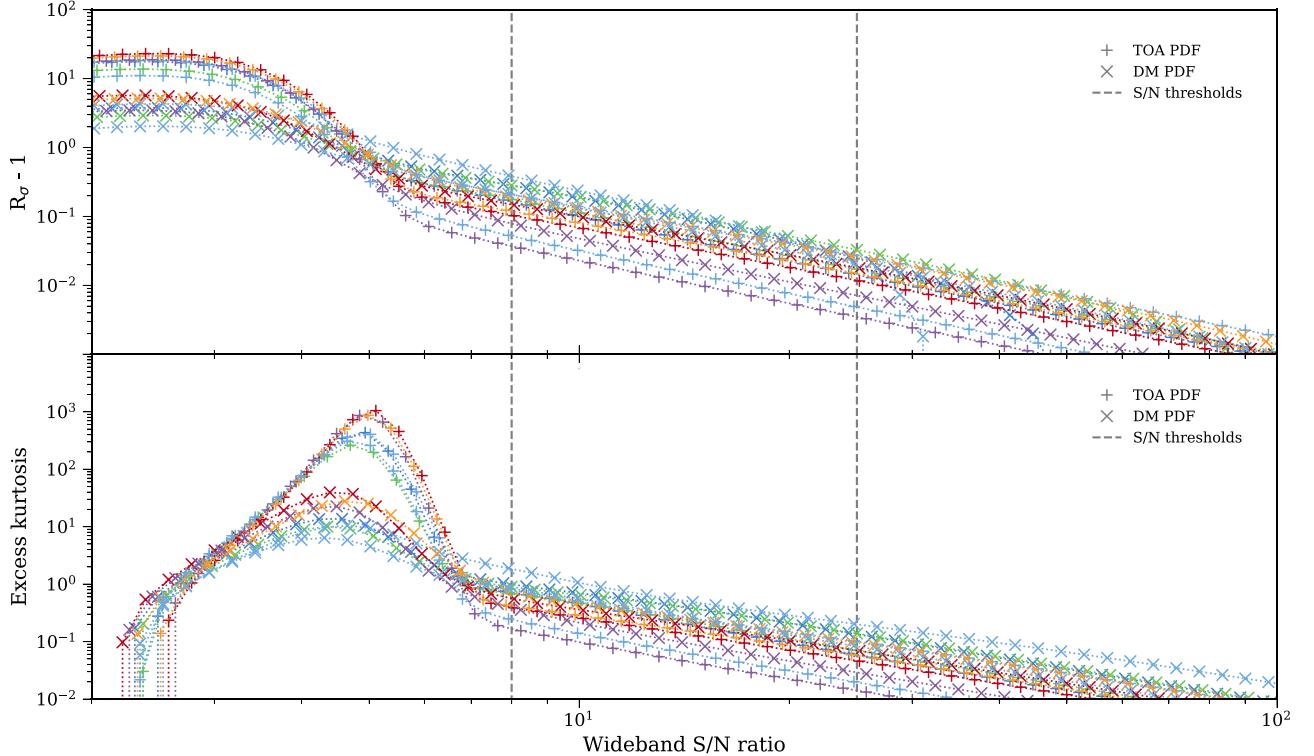
$$S \equiv \sqrt{\sum_n S_n^2}. \tag{A3}$$

This is the quantity paired with the wideband TOA flag `-snr` from Table 2.

We can see that Equation (A3) utilizes information that would otherwise be discarded on a per-channel basis by a narrowband TOA threshold of S/N < 8, unless the original data were averaged down to fewer frequency channels to boost each channel's S/N. As an extreme example, suppose a single subintegration has just enough signal distributed evenly over all frequency channels such that all of its narrowband TOAs would be removed by thresholding unless all of the profiles are averaged together, thus acquiring an S/N > 8. By this averaging argument, we should therefore expect that the minimally informative wideband TOA has a "typical" per-channel $S_n < 8$ and that its PDF behaves similarly such that it becomes highly non-Gaussian around $S \sim 8$.

However, by the same token, Equations (A3) and (A1) tell us that S will always be biased high, and this bias can be particularly high in the limit of very low S/N. This is because the maximum-likelihood estimates of a_n are noisy (in particular, they will never be exactly zero), they will be poorly estimated in the low-S/N regime, and they enter Equation (A3) as a_n^2. That is, even in the absence of any signal, S is strictly positive. Depending on the statistical properties of a_n in the absence of a signal, S may be more biased when the same bandwidth is divided up into a greater number of frequency channels. Furthermore, in the low-S/N regime, the presence of otherwise low-level RFI will further bias S high. It is for these reasons that, even though we recover the theoretical behavior of the wideband TOA PDF around $S \sim 8$ (see below), we implemented a larger threshold. From visual inspection, many of the TOAs between $8 < S < 25$ appeared to be subject to these biases; after implementing the threshold that TOAs with $S < 25$ are cut, only a handful of additional TOAs needed to be manually culled, which were confirmed to be affected by subtle, broadband RFI.

Table 3 reveals that, overall, the wideband data set is including a lot of the profiles that were discarded in the narrowband analysis by its threshold of S/N < 8; the number of profiles in the wideband data set is 16% larger than the number of retained narrowband TOAs. This hypothesis is supported by pointing out that there are 92,290 TOAs cut from the narrowband data set due to its S/N thresholding, whereas there are only 500 TOAs removed from the wideband data set due to its S/N thresholding. Taking the number 30 as a representative number of frequency channels per wideband TOA on average, those low-S/N wideband TOAs correspond to ~15,000 profiles. Without considering any of the other curating described in Section 3.4, then as a back-of-the-envelope estimate there are ~77,290 more profiles in the wideband data set that were discarded as TOAs by the narrowband S/N threshold; this is in line with the 16% difference in Table 3. The S/N thresholding results in the largest single cut to the narrowband TOA data set by a very large margin (see Table 1 in NG12.5), and

Figure 8. Behavior of maximum-likelihood wideband TOA and DM PDFs in the low-S/N regime for three pulsars' evolving template models (J1012+5307, J1903 +0327, and J2317+1437), which together cover all receivers in the data set. The colors indicate the receiver as in Figure 1: 327 MHz (red), 430 MHz (orange), 820 MHz (green), 1.4 GHz (lighter blue for AO, darker blue for the GBT), 2.1 GHz (purple). The PDFs were calculated to emulate data from PUPPI and GUPPI, but the counterpart ASP and GASP curves overlap almost identically. The behavior of all other pulsars' profile evolution models is qualitatively the same. The top panel plots the ratio R_σ (minus one), where the ratio is the standard deviation of the evaluated PDF divided by the expected 1σ parameter uncertainty. The zero-covariance TOA reference frequency is used in all calculations (see the Appendix of Pennucci et al. 2014). The bottom panel plots the excess kurtosis (i.e., kurtosis minus three), where the kurtosis for a normally distributed random variable is three. The deviation from the Gaussian expectation ($R_\sigma = 1$, excess kurtosis = 0) is large below S/ N ~ 8, and for reasons described in the text, we make a more conservative threshold at S/N = 25.

the wideband processing has recovered ~80% of these profiles. It is important to point out, however, that because many of these profiles will have at most an S/N ~ 8 (and will have zero signal in many cases), the impact they have is much less than one would expect from having 16% more of typical data.

To verify the theoretical expectation for the expected uncertainties on the wideband measurements, we evaluated Equation (A2) as a function of S/N for each of our evolving template models. For each model, we constructed the frequency-dependent template using a central frequency, bandwidth, and number of channels typical of the receiver in question, for both generations of back-end instruments. Furthermore, we zero-weighted a typical number of random channels for that receiver to better emulate the measurement uncertainties in the real data set. For a given model and S/N, we calculated the second and fourth moments of the PDF, related to the variance and kurtosis, respectively, each for the TOA and DM by fixing the other parameter to the maximum-likelihood value. Figure 8 shows the results of this analysis for three pulsars that together cover all receiver bands: J1012 +5307, J1903+0327, and J2317+1437. In the figure, we plot $R_\sigma - 1$ and the excess kurtosis. R_σ is the ratio of the PDF's measured standard deviation to the expected 1σ parameter uncertainty estimated from the Fisher information of Equation (2), which assumes Gaussian statistics. An idealized Gaussian-distributed variable will have $R_\sigma = 1$ and an excess kurtosis of zero. It is evident that below S/N ~ 8, the PDFs

deviate largely from the Gaussian expectation, and we also indicate our wideband S/N threshold of 25 in the figure. These conclusions are bolstered by the Monte Carlo analyses performed in Pennucci et al. (2014), which demonstrated that the uncertainties are properly estimated (assuming Gaussian noise) down to low S/N.

Appendix B
Wideband Timing Likelihood

In this section we derive our new wideband timing likelihood. We borrow notation from Appendix C of NG9, which also contains details that we omit here. The wideband timing residuals δt are modeled by deterministic and stochastic components via

$$\delta t = M\epsilon + Fa + n. \tag{B1}$$

The product of the timing model design matrix M with small offsets in the timing model parameters ϵ describes the systematic residuals from subtracting the timing model. F is the design matrix for the Fourier series decomposition of the red noise, with a being the amplitudes of the Fourier basis functions. Lastly, n represents the noise remaining in the residuals, which is expected to be uncorrelated in both frequency and time. This white noise is formally a Gaussian

process with likelihood

$$p(\boldsymbol{n}) = \frac{\exp\left(-\frac{1}{2}\boldsymbol{n}^T N^{-1}\boldsymbol{n}\right)}{\sqrt{|2\pi N|}}, \qquad (B2)$$

where N is an $N_{\mathrm{TOA}} \times N_{\mathrm{TOA}}$ diagonal data covariance matrix with entries

$$N_{ij} = (E_{k(i)}^2 \sigma_i^2 + Q_{k(i)}^2)\,\delta_{ij}. \qquad (B3)$$

The TOA uncertainties σ_i are modified by the EFAC and EQUAD parameters E_k and Q_k, respectively.[51] The label function k indicates the observing system combination of the front-end receiver and back-end data acquisition instrument for the observation with index i (or j), and δ_{ij} is the Kronecker delta. As mentioned in Section 3.5, because of the nature of wideband TOAs, we do not separately model jitter-like white noise that is completely correlated across simultaneously measured multifrequency TOAs and completely uncorrelated between epochs (i.e., there are no ECORR parameters). Any physical effects that would contribute to ECORR in the narrowband analyses will be completely absorbed by EQUAD and the red noise in the wideband analysis. The red noise is also modeled as a Gaussian process specified by $2n_{\mathrm{mode}}$ Fourier basis vectors (the columns of F) and by the prior on the $2n_{\mathrm{mode}}$ coefficients $\boldsymbol{a}$ (i.e., weights):

$$p(\boldsymbol{a}\,|A_{\mathrm{red}},\,\gamma_{\mathrm{red}}) = \frac{\exp\left(-\frac{1}{2}\boldsymbol{a}^T\varphi^{-1}\boldsymbol{a}\right)}{\sqrt{|2\pi\varphi|}}, \qquad (B4)$$

where φ is a $2n_{\mathrm{mode}} \times 2n_{\mathrm{mode}}$ diagonal matrix with entries $T_{\mathrm{span}}^{-1}P(f_m)$. Here, T_{span} is the span of the data set, $P(f_m)$ is the power-law function of Equation (5), and f_m are the n_{mode} frequencies of the Fourier components indexed by m.

We also model the timing model corrections as a Gaussian process. We refer to the subset of the timing model offsets ϵ that describe the piecewise-constant DMX model as $\epsilon^{\mathrm{DM X}}$. Except for $\epsilon^{\mathrm{DM X}}$, the remaining timing model offsets are given uninformative priors; formally, these are zero-mean Gaussian distributions with very large variances. The novel development we make here is to use the wideband DM measurements to provide a prior for $\epsilon^{\mathrm{DM X}}$. Assuming that the $\delta\boldsymbol{t}$ are computed with respect to a fiducial DM that is constant in the data set and that $\delta\boldsymbol{D}$ is the vector of DM measurements relative to the fiducial DM, then the prior for $\epsilon^{\mathrm{DM X}}$ can be written as

$$p(\epsilon^{\mathrm{DM X}}\,|\delta\boldsymbol{D},\,\boldsymbol{J}^{\mathrm{DM}},\,\boldsymbol{E}^{\mathrm{DM}})$$
$$= \frac{\exp-\frac{1}{2}((\epsilon^{\mathrm{DM X}} - \delta\boldsymbol{D} - \boldsymbol{J}^{\mathrm{DM}})^T N^{\mathrm{DM}^{-1}}(\epsilon^{\mathrm{DM X}} - \delta\boldsymbol{D} - \boldsymbol{J}^{\mathrm{DM}}))}{\sqrt{|2\pi N^{\mathrm{DM}}|}},$$
$$(B5)$$

where N^{DM} is an $n_{\mathrm{DM}} \times n_{\mathrm{DM}}$ ($=n_{\mathrm{TOA}} \times n_{\mathrm{TOA}}$) diagonal covariance matrix containing the DM measurement errors σ_i^{DM} scaled by DMEFAC parameters $\boldsymbol{E}^{\mathrm{DM}} \equiv E_k^{\mathrm{DM}}$,

$$N_{ij}^{\mathrm{DM}} = (E_{k(i)}^{\mathrm{DM}}\sigma_i^{\mathrm{DM}})^2\,\delta_{ij}, \qquad (B6)$$

---

[51] Equation (B3) is the same formulation as found in ENTERPRISE; in Tempo, however, the EFAC parameter is applied after the quadrature sum, meaning a conversion is necessary to obtain the corresponding Tempo EQUAD parameter, $Q_{k(i),\mathrm{Tempo}} = Q_{k(i)}/E_{k(i)}$.

and where $\boldsymbol{J}^{\mathrm{DM}} \equiv J_{r(i)}^{\mathrm{DM}}$ are the DMJUMP parameters described in Sections 3.3 and 3.5, labeled by receiver r. Altogether, our model of the measurement yields the posterior

$$p(\epsilon,\,\boldsymbol{a},\,\phi,\,\boldsymbol{J}^{\mathrm{DM}},\,\boldsymbol{E}^{\mathrm{DM}}\,|\delta\boldsymbol{t},\,\delta\boldsymbol{D}) \propto p(\boldsymbol{a}\,|A_{\mathrm{red}},\,\gamma_{\mathrm{red}})$$
$$\times\, p(\epsilon^{\mathrm{DM X}}\,|\delta\boldsymbol{D},\,\boldsymbol{J}^{\mathrm{DM}},\,\boldsymbol{E}^{\mathrm{DM}}) \times p(\delta\boldsymbol{t}\,|\epsilon,\,\boldsymbol{a},\,\phi), \qquad (B7)$$

where the last term on the right is the usual likelihood for the timing residuals,

$$p(\delta\boldsymbol{t}\,|\epsilon,\,\boldsymbol{a},\,\phi) = \frac{\exp\left(-\frac{1}{2}\boldsymbol{r}^T N^{-1}\boldsymbol{r}\right)}{\sqrt{|2\pi N|}}, \qquad (B8)$$

the EFAC and EQUAD parameters comprise the vector ϕ, and $\boldsymbol{r} = \delta\boldsymbol{t} - M\epsilon - F\boldsymbol{a}$. The marginalization of the posterior over the timing model parameters proceeds in the same way as described in NG9. Note that the two separate data covariance matrices N and N^{DM} imply zero covariance between the TOA and DM measurements; as mentioned in Section 3.2, all wideband TOAs reference a frequency such that the measurement has an estimated zero covariance with its associated DM. Another way to look at Equation (B7) is to see the DM measurements as data in a joint likelihood with the wideband TOAs instead of as prior information on the DMX parameters; in either case, the formulation will be the same.

We implemented the wideband posterior in the PTA analysis package ENTERPRISE, with which we performed the analyses described in Section 3.5. In ENTERPRISE, the functionality is accessed by using the signal class WidebandTimingModel with a Pulsar object that has wideband TOAs and DM measurements. Similarly, we implemented the DMX prior in Equation (B5), which can also be viewed as an additional likelihood component, in the pulsar timing software Tempo. Tempo's generalized least-squares fit must be used in order to enable the new functionality with wideband TOAs, and the input timing model parameter file must contain the line DMDATA 1, which we have included in the released files. As a result of these developments, the wideband timing models in this data set come with DMEFAC and DMJUMP parameters, along with the usual EFAC, EQUAD, and red-noise parameters. Our formalism of using the wideband DM measurements currently only works with the DMX model for DM variations. Extending this to a stochastic, Gaussian process model of DM variations (e.g., Lentati et al. 2013a) is currently under development (J. Simon et al. 2020, in preparation).

Appendix C
Timing Residuals and DM Variations
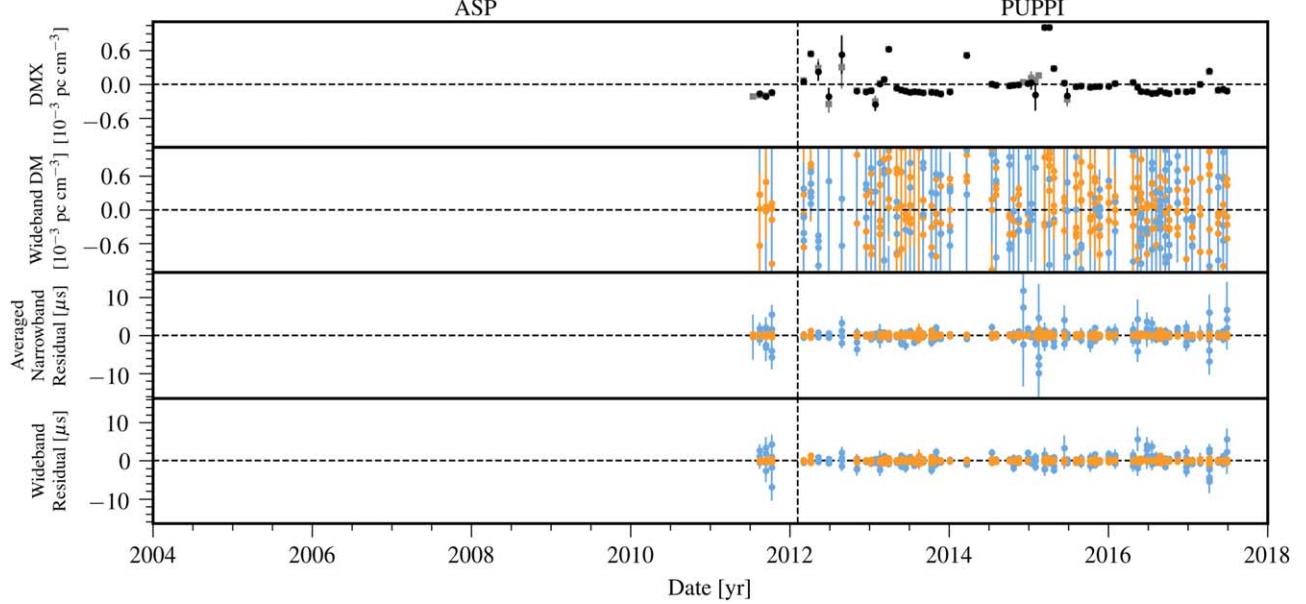
Here we include an appendix of timing residuals and DM variations for each pulsar in our data set (Figures 9–55) as a complement to a similar appendix in NG12.5. Measurements from both wideband and narrowband data sets are plotted for visual comparison. The predominant back-end instrument for a given time period is printed at the top of each plot, with vertical dashed lines indicating times at which the instruments changed. The color-coding of the timing residuals and wideband DM measurements indicates the receiver used for that observation and is the same as in Figure 1: 327 MHz (red), 430 MHz (orange), 820 MHz (green), 1.4 GHz (lighter blue for AO, darker blue for the GBT), and 2.1 GHz (purple).

DM variations. The top two panels of each figure show the variation in DM for each pulsar. The black circles in the topmost panel are the DMX model parameters (see Section 3.5) and the gray squares are the corresponding DMX parameters modeled in NG12.5, which may not be visible due to the agreement with their wideband counterparts. The panel second from the top shows the DM measurements that are paired with each wideband TOA; these measurements are adjusted based on the MAP DMEFAC and DMJUMP parameters (see Appendix B). The average DM value has been removed from all three time series, and the two panels have the same scale, determined by the maximum DMX deviation in the narrow-band data set. As a result, some of the wideband DM measurements in the second panel fall outside the plotted range (particularly those from the ASP and GASP era), depending on how informative the measurements are to the DMX model. A number of pulsars show a DM variation that may be a function of frequency; see Section 4.3 for further discussion.

Timing residuals. The remaining panels contain timing residuals, which are the observed TOAs minus the predicted arrival time from the timing model (see Section 3.5). All residual uncertainties include the white-noise-model compo-nents (i.e., the MAP EFAC and EQUAD parameters; see Appendix B). Linear and quadratic trends have been subtracted from the plotted timing residuals, as they are completely covariant with the pulsar's rotation frequency and frequency derivative in the timing model, respectively, and hence would be absorbed by these parameters. The first panel after the DM panels show the averaged narrowband timing residuals, which is the same as panel (d) from the analogous residual plot in NG12.5. Where red noise is significant in both data sets (see Table 5 and Figure 7), the panel second from the bottom contains the whitened averaged narrowband timing residuals, which is the same as panel (e) from NG12.5. The panels just below each of these two panels show their wideband counter-parts, the results of the present work. The limits in each timing residual panel mirror those from NG12.5, which permit a useful visual comparison between the data sets. However, a small number of residuals ($\sim$0.5%) fall outside of the limits; the averaged narrowband residuals are also plotted in NG12.5 such that all data points are visible. Overall, the agreement in timing residuals is remarkable, though see Sections 4.4 and 4.5 for further discussion.

J0023+0923
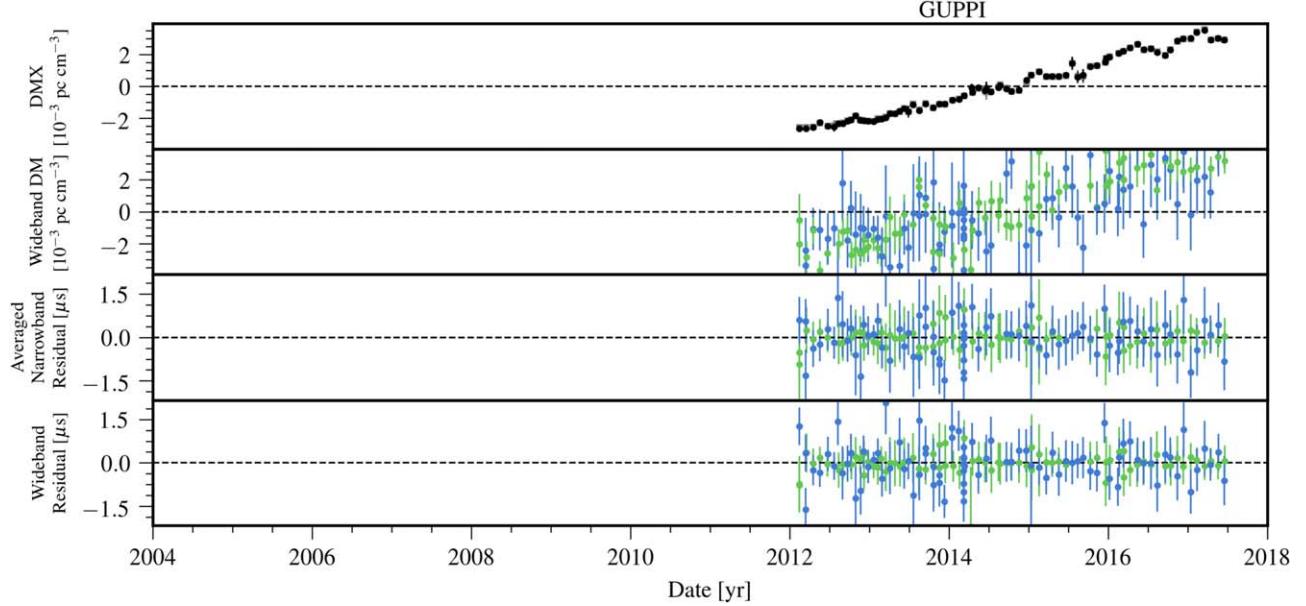
Figure 9. Timing residuals and DM variations for J0023+0923. See Appendix C for details. DMX model parameters from the wideband (black circles) and narrowband (gray squares) data sets are shown in the top panel. Colors in the lower panels indicate the receiver for the observation: 430 MHz (orange) and 1.4 GHz (light blue).

J0030+0451
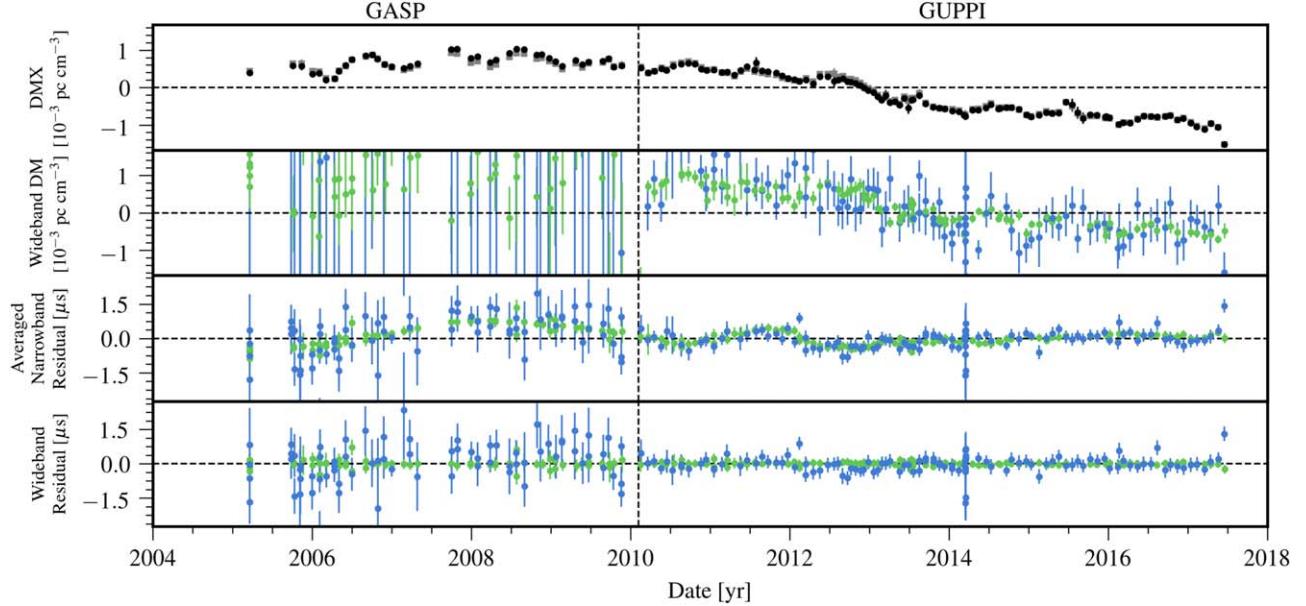
Figure 10. Timing residuals and DM variations for J0030+0451. See Appendix C for details. DMX model parameters from the wideband (black circles) and narrowband (gray squares) data sets are shown in the top panel. Colors in the lower panels indicate the receiver for the observation: 430 MHz (orange), 1.4 GHz (light blue), and 2.1 GHz (purple).
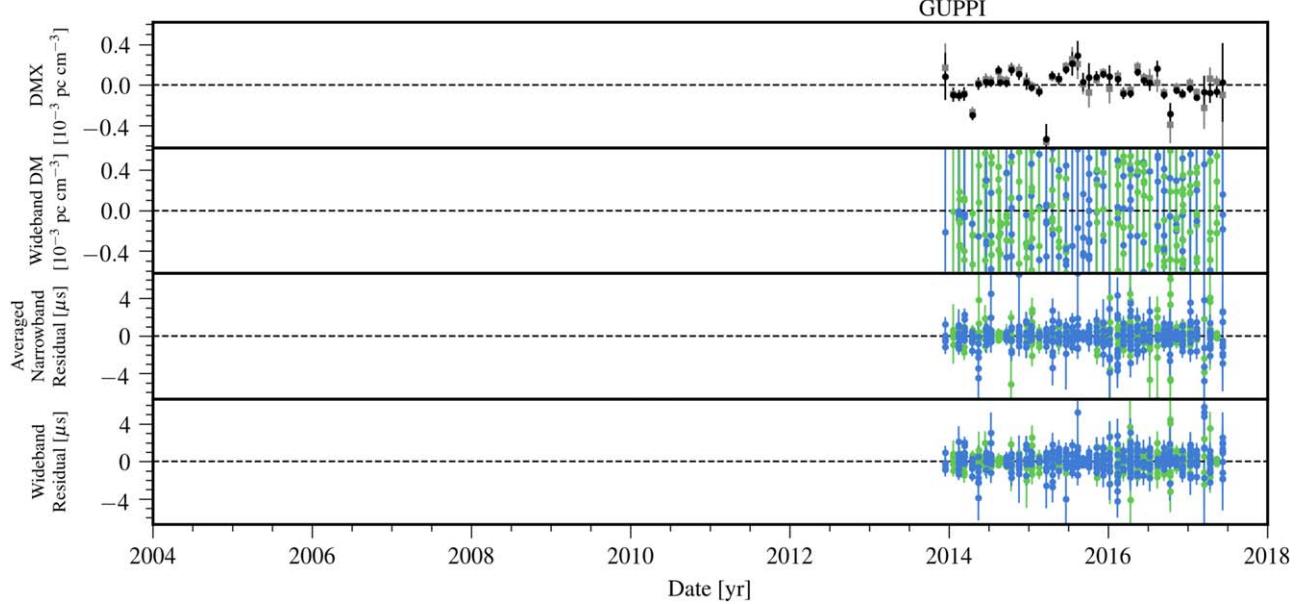
Figure 11. Timing residuals and DM variations for J0340+4130. See Appendix C for details. DMX model parameters from the wideband (black circles) and narrowband (gray squares) data sets are shown in the top panel. Colors in the lower panels indicate the receiver for the observation: 820 MHz (green) and 1.4 GHz (dark blue).
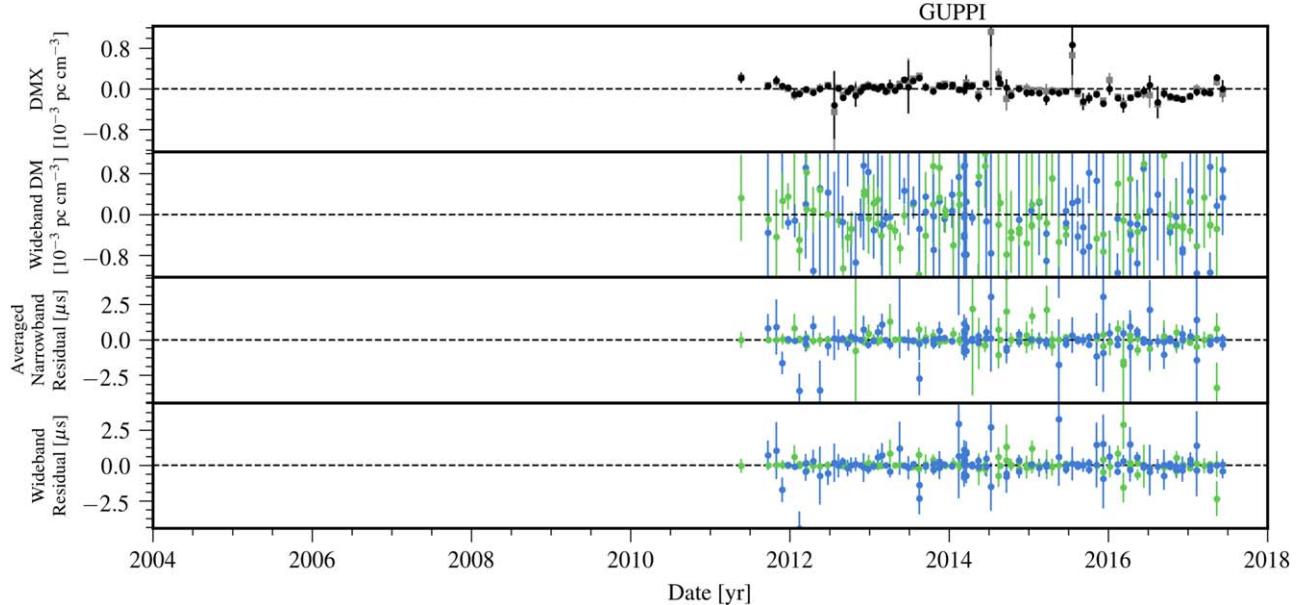

Figure 12. Timing residuals and DM variations for J0613−0200. See Appendix C for details. DMX model parameters from the wideband (black circles) and narrowband (gray squares) data sets are shown in the top panel. Colors in the lower panels indicate the receiver for the observation: 820 MHz (green) and 1.4 GHz (dark blue).

J0636+5128
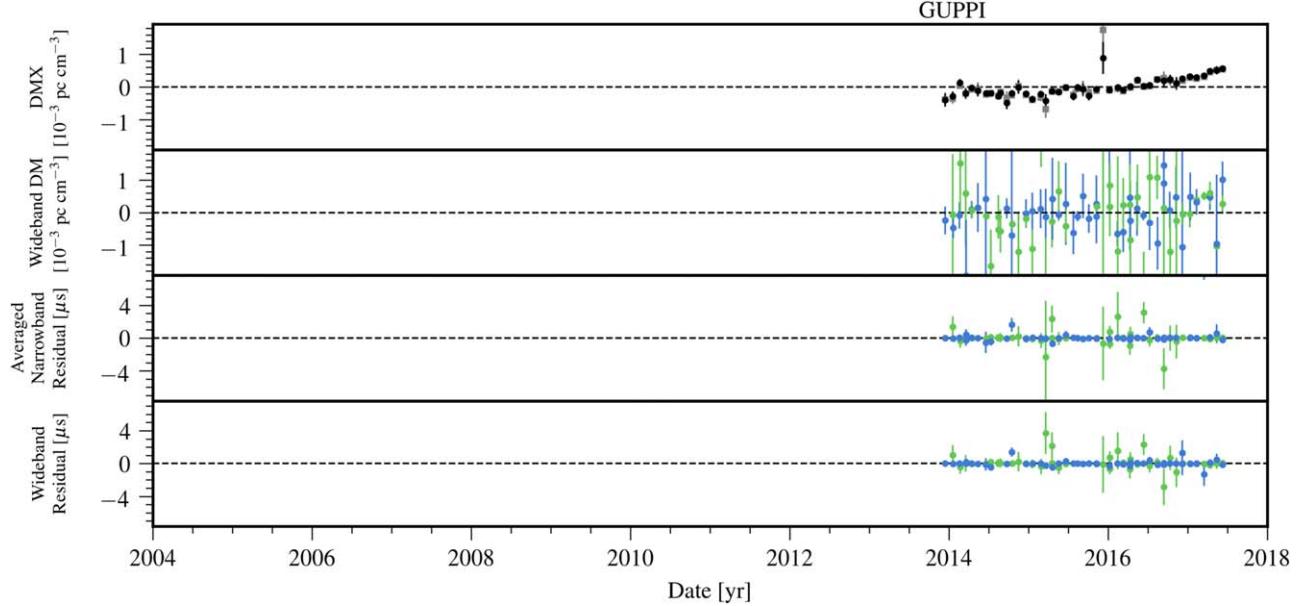
Figure 13. Timing residuals and DM variations for J0636+5128. See Appendix C for details. DMX model parameters from the wideband (black circles) and narrowband (gray squares) data sets are shown in the top panel. Colors in the lower panels indicate the receiver for the observation: 820 MHz (green) and 1.4 GHz (dark blue).

J0645+5158
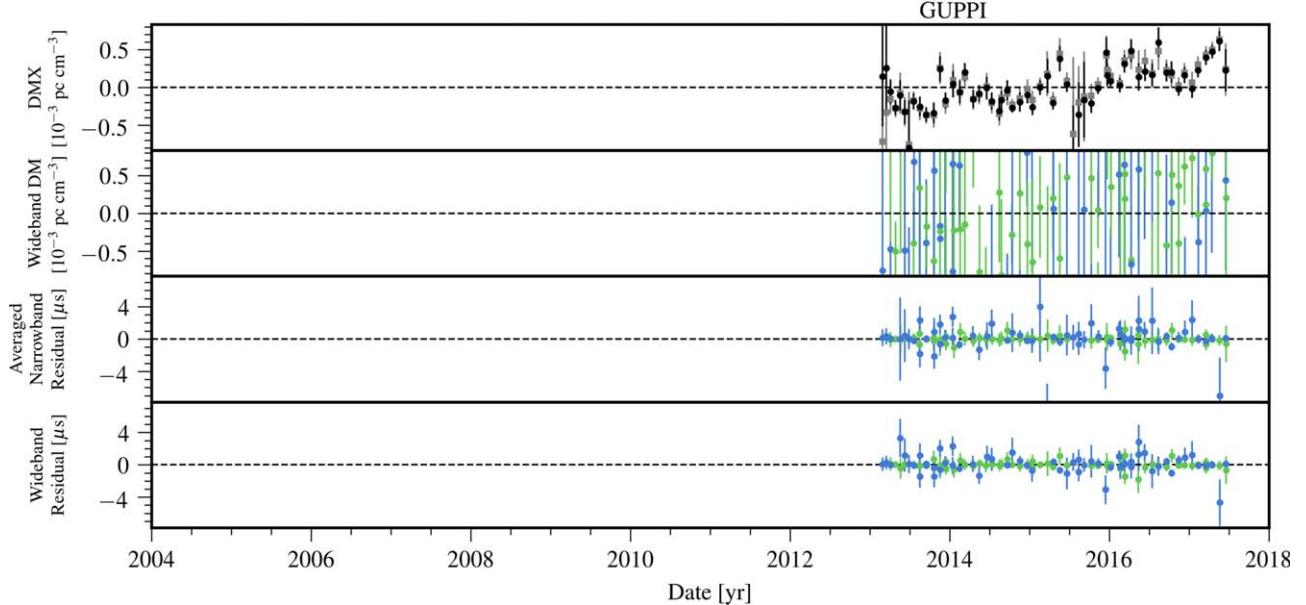
Figure 14. Timing residuals and DM variations for J0645+5158. See Appendix C for details. DMX model parameters from the wideband (black circles) and narrowband (gray squares) data sets are shown in the top panel. Colors in the lower panels indicate the receiver for the observation: 820 MHz (green) and 1.4 GHz (dark blue).

J0740+6620
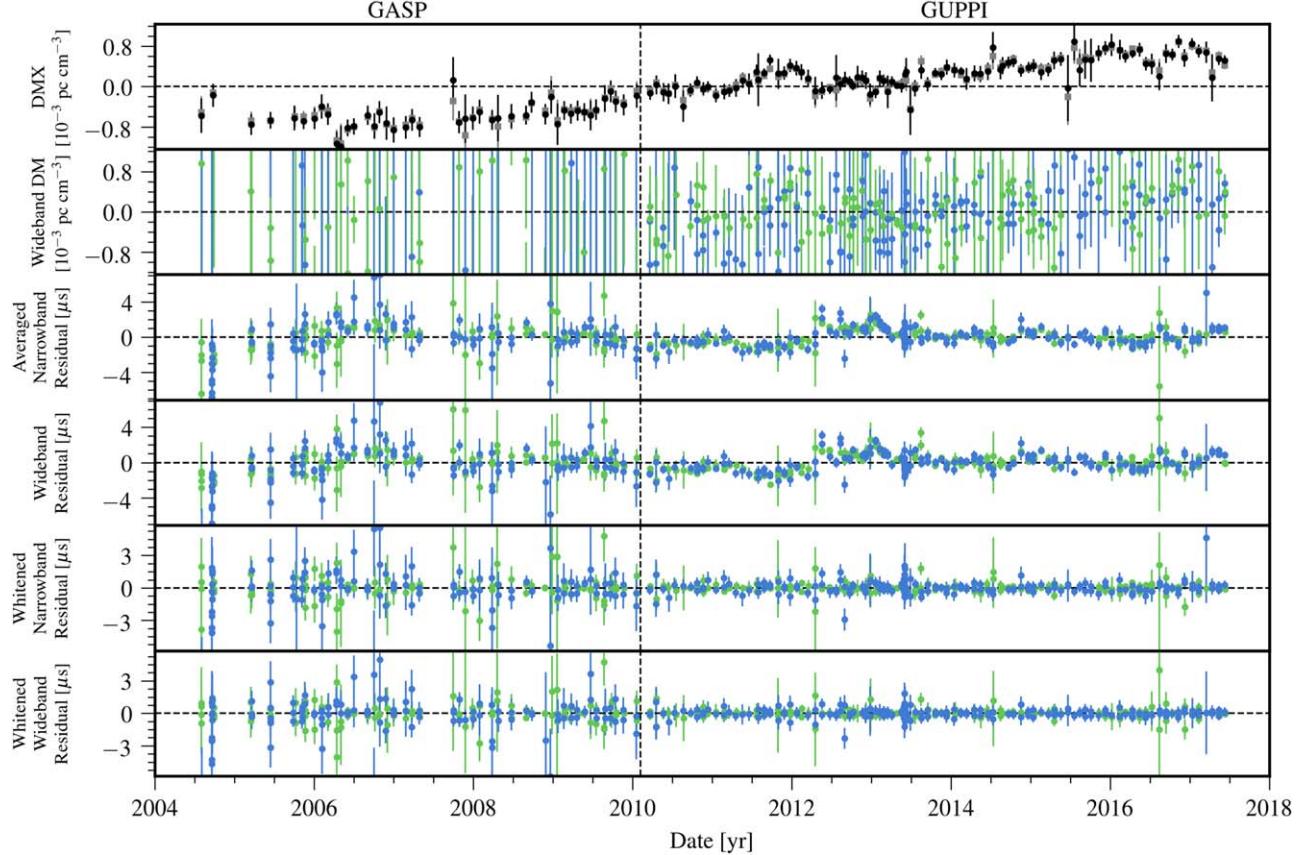
Figure 15. Timing residuals and DM variations for J0740+6620. See Appendix C for details. DMX model parameters from the wideband (black circles) and narrowband (gray squares) data sets are shown in the top panel. Colors in the lower panels indicate the receiver for the observation: 820 MHz (green) and 1.4 GHz (dark blue).

J0931−1902
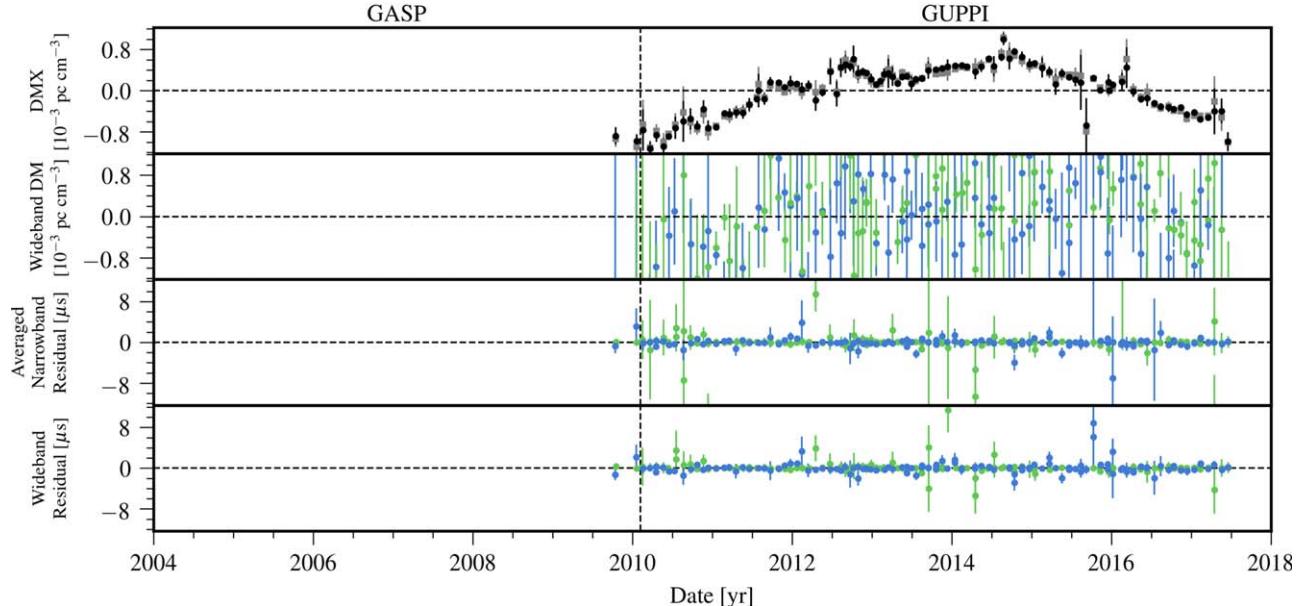
Figure 16. Timing residuals and DM variations for J0931−1902. See Appendix C for details. DMX model parameters from the wideband (black circles) and narrowband (gray squares) data sets are shown in the top panel. Colors in the lower panels indicate the receiver for the observation: 820 MHz (green) and 1.4 GHz (dark blue).

J1012+5307
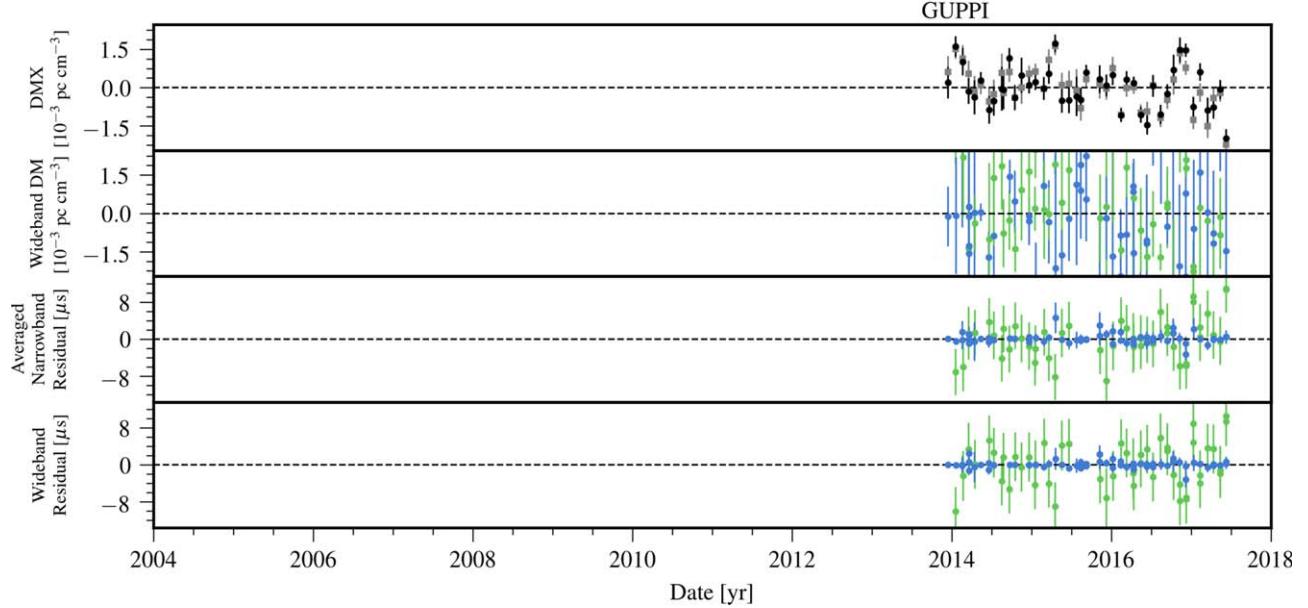
Figure 17. Timing residuals and DM variations for J1012+5307. See Appendix C for details. DMX model parameters from the wideband (black circles) and narrowband (gray squares) data sets are shown in the top panel. Colors in the lower panels indicate the receiver for the observation: 820 MHz (green) and 1.4 GHz (dark blue).

J1024−0719
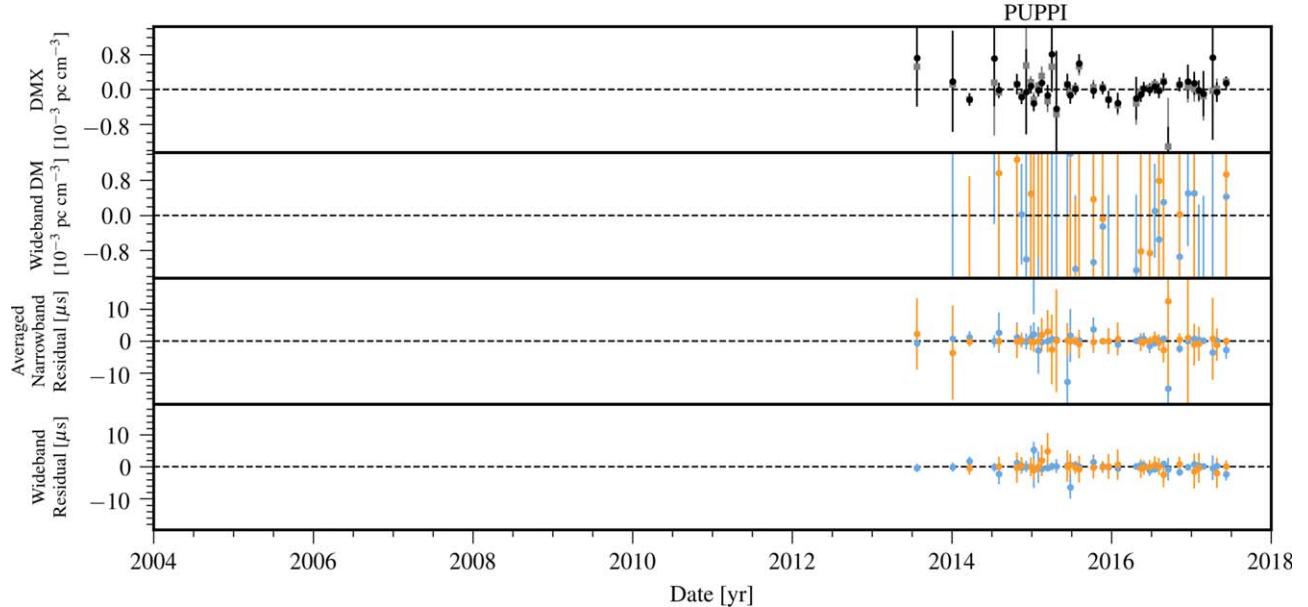
Figure 18. Timing residuals and DM variations for J1024−0719. See Appendix C for details. DMX model parameters from the wideband (black circles) and narrowband (gray squares) data sets are shown in the top panel. Colors in the lower panels indicate the receiver for the observation: 820 MHz (green) and 1.4 GHz (dark blue).

J1125+7819
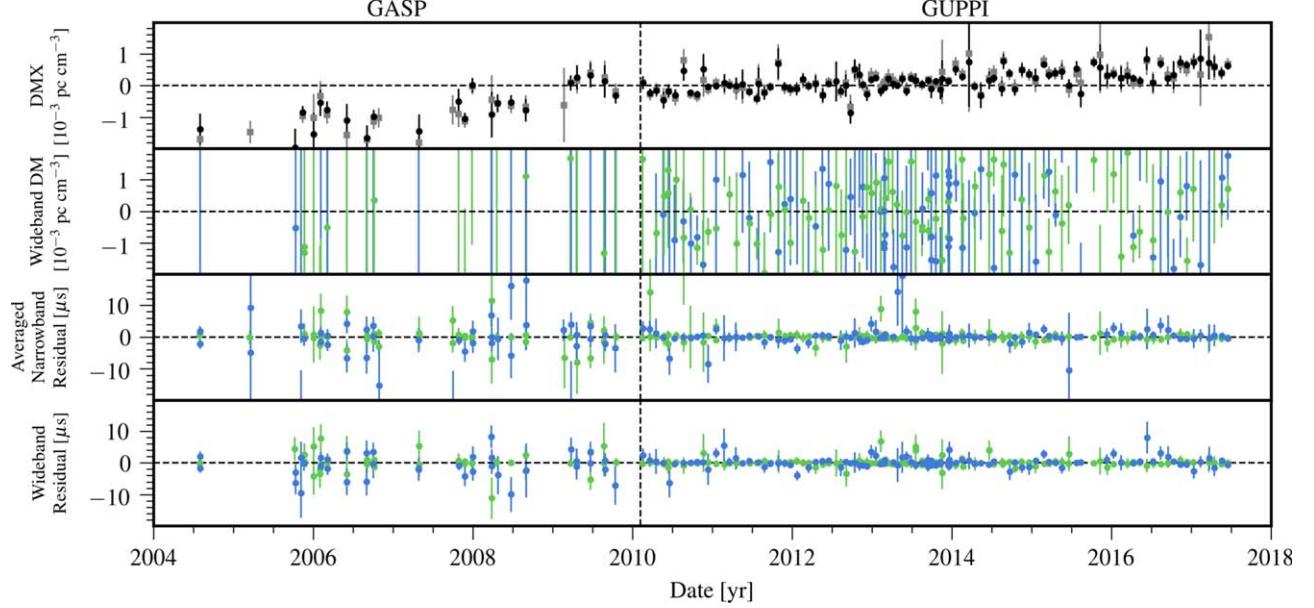
Figure 19. Timing residuals and DM variations for J1125+7819. See Appendix C for details. DMX model parameters from the wideband (black circles) and narrowband (gray squares) data sets are shown in the top panel. Colors in the lower panels indicate the receiver for the observation: 820 MHz (green) and 1.4 GHz (dark blue).

J1453+1902
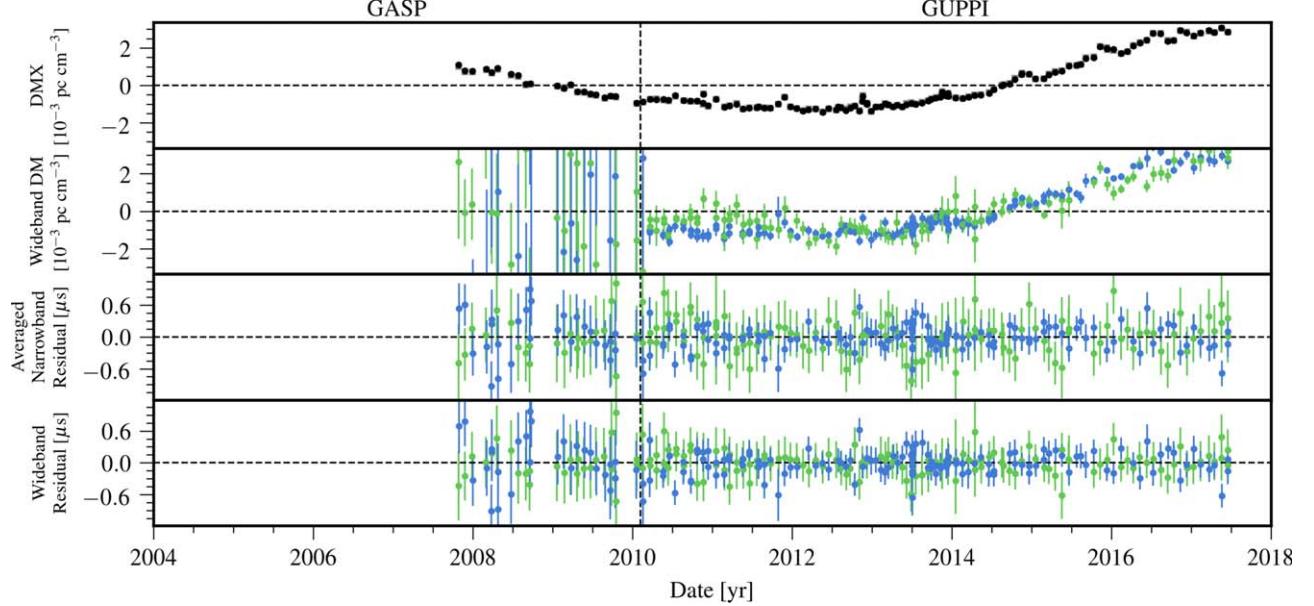
Figure 20. Timing residuals and DM variations for J1453+1902. See Appendix C for details. DMX model parameters from the wideband (black circles) and narrowband (gray squares) data sets are shown in the top panel. Colors in the lower panels indicate the receiver for the observation: 430 MHz (orange) and 1.4 GHz (light blue).
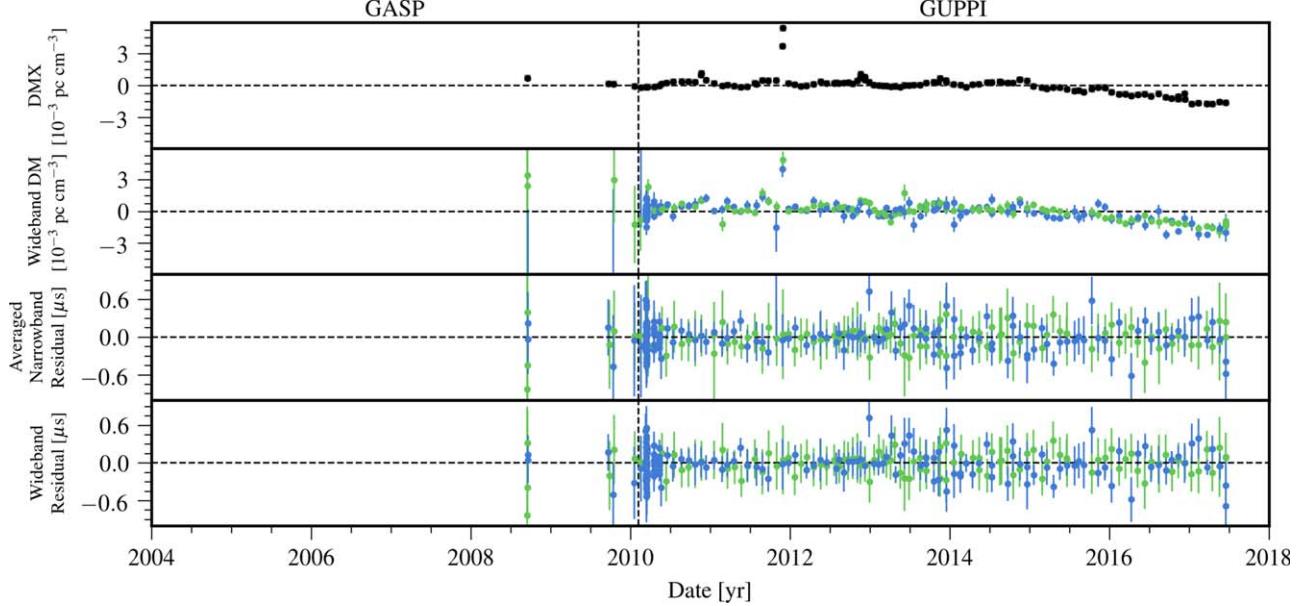
Figure 21. Timing residuals and DM variations for J1455−3330. See Appendix C for details. DMX model parameters from the wideband (black circles) and narrowband (gray squares) data sets are shown in the top panel. Colors in the lower panels indicate the receiver for the observation: 820 MHz (green) and 1.4 GHz (dark blue).
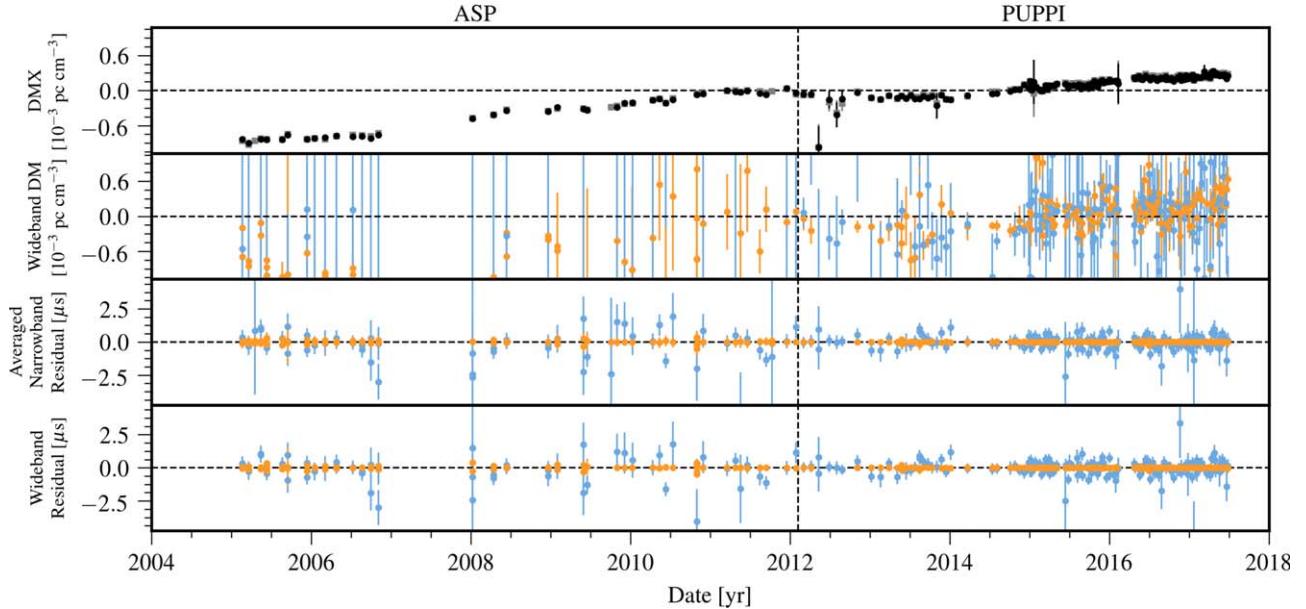
**Figure 22.** Timing residuals and DM variations for J1600−3053. See Appendix C for details. DMX model parameters from the wideband (black circles) and narrowband (gray squares) data sets are shown in the top panel. Colors in the lower panels indicate the receiver for the observation: 820 MHz (green) and 1.4 GHz (dark blue).
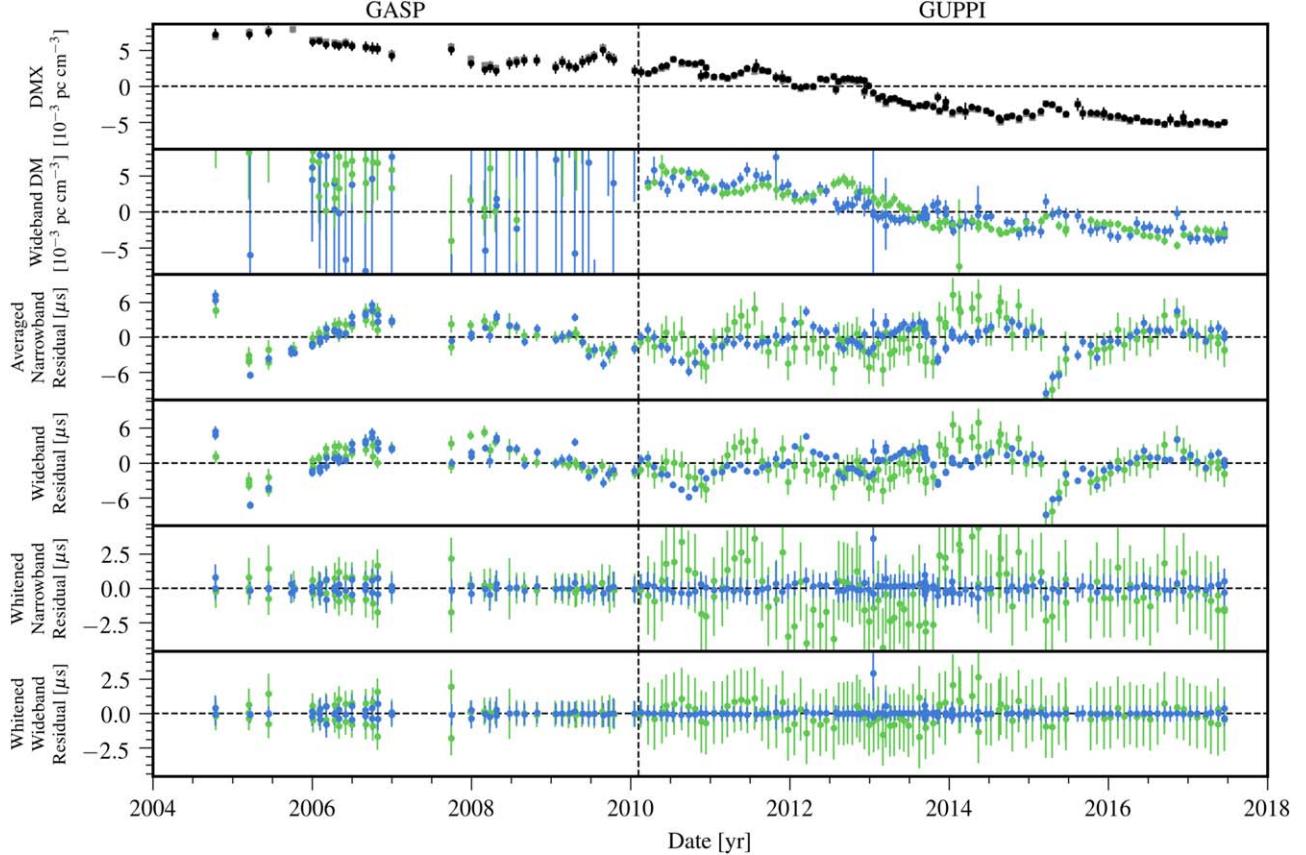
Figure 23. Timing residuals and DM variations for J1614−2230. See Appendix C for details. DMX model parameters from the wideband (black circles) and narrowband (gray squares) data sets are shown in the top panel. Colors in the lower panels indicate the receiver for the observation: 820 MHz (green) and 1.4 GHz (dark blue).
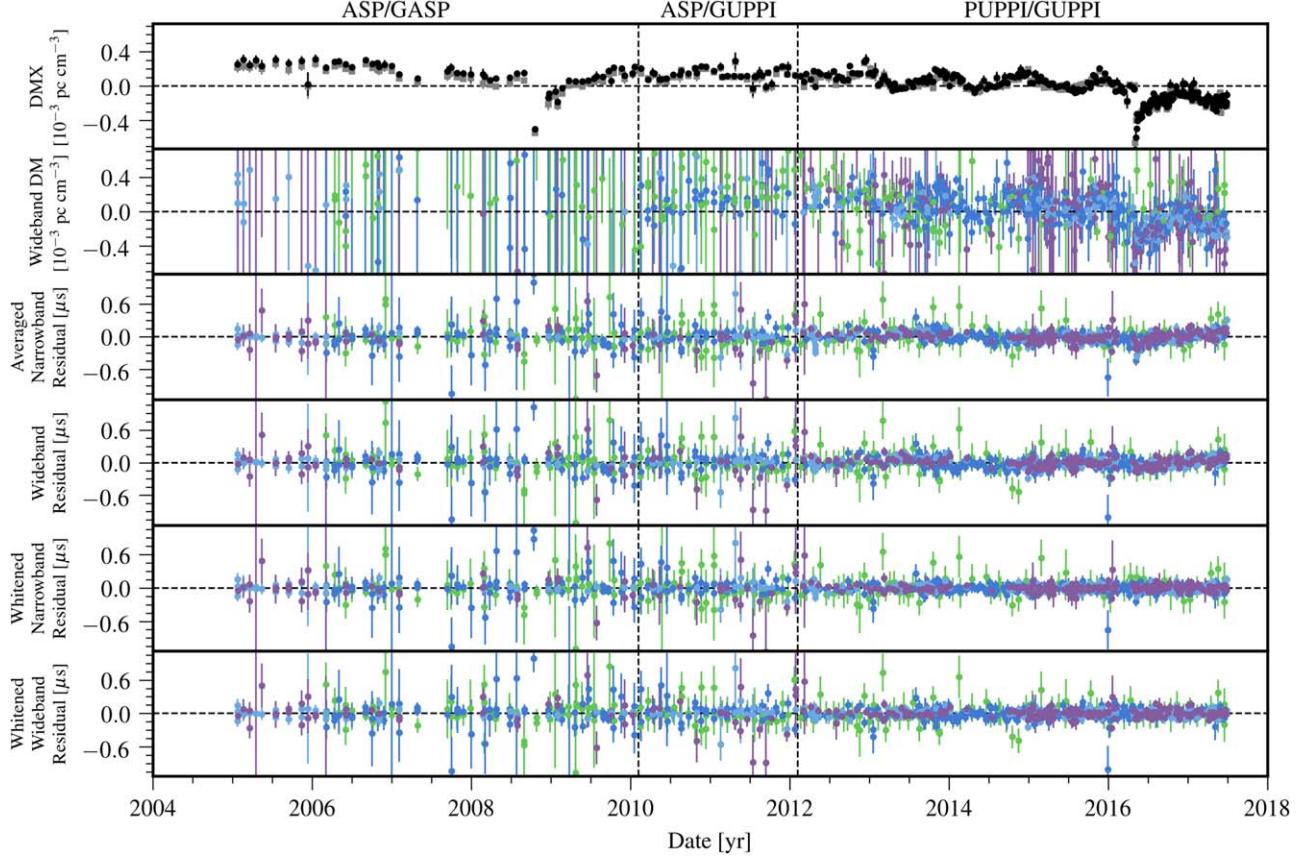
Figure 24. Timing residuals and DM variations for J1640+2224. See Appendix C for details. DMX model parameters from the wideband (black circles) and narrowband (gray squares) data sets are shown in the top panel. Colors in the lower panels indicate the receiver for the observation: 430 MHz (orange) and 1.4 GHz (light blue).
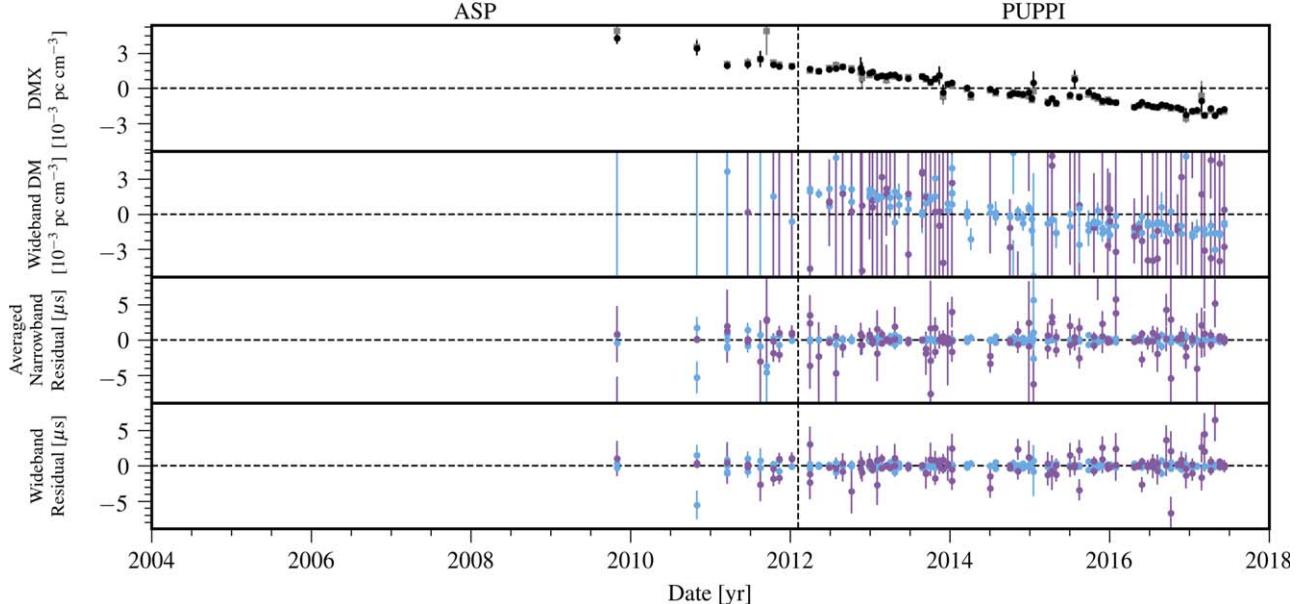
Figure 25. Timing residuals and DM variations for J1643−1224. See Appendix C for details. DMX model parameters from the wideband (black circles) and narrowband (gray squares) data sets are shown in the top panel. Colors in the lower panels indicate the receiver for the observation: 820 MHz (green) and 1.4 GHz (dark blue).
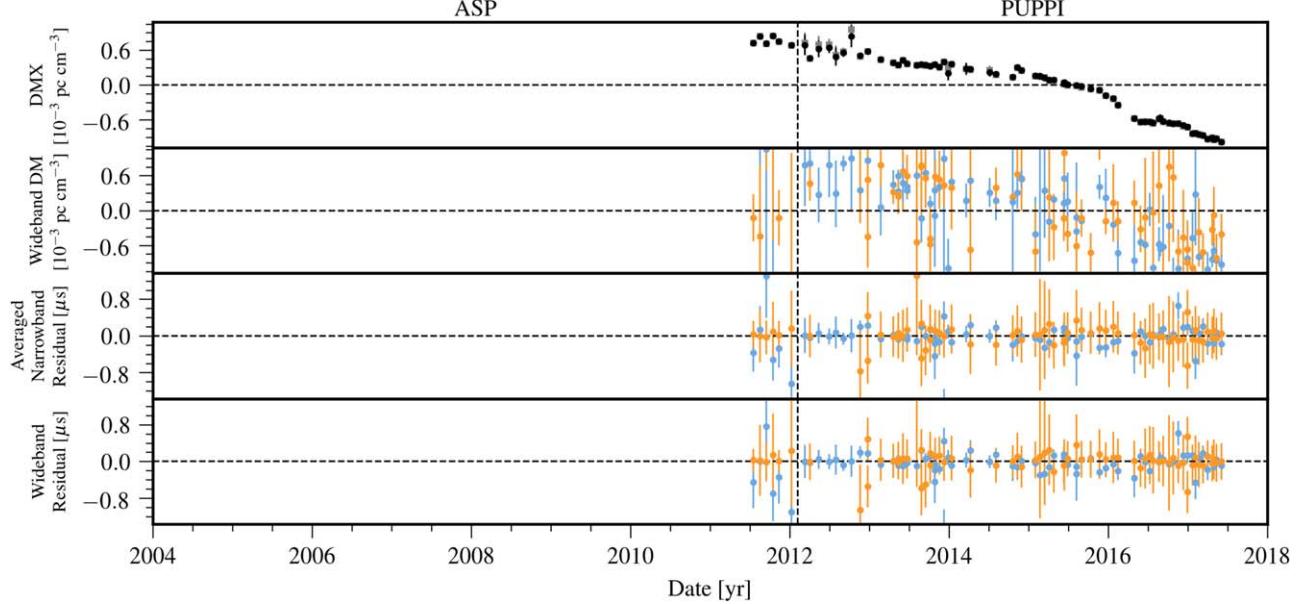
Figure 26. Timing residuals and DM variations for J1713+0747. See Appendix C for details. DMX model parameters from the wideband (black circles) and narrowband (gray squares) data sets are shown in the top panel. Colors in the lower panels indicate the receiver for the observation: 820 MHz (green), 1.4 GHz (dark blue), 1.4 GHz (light blue), and 2.1 GHz (purple).
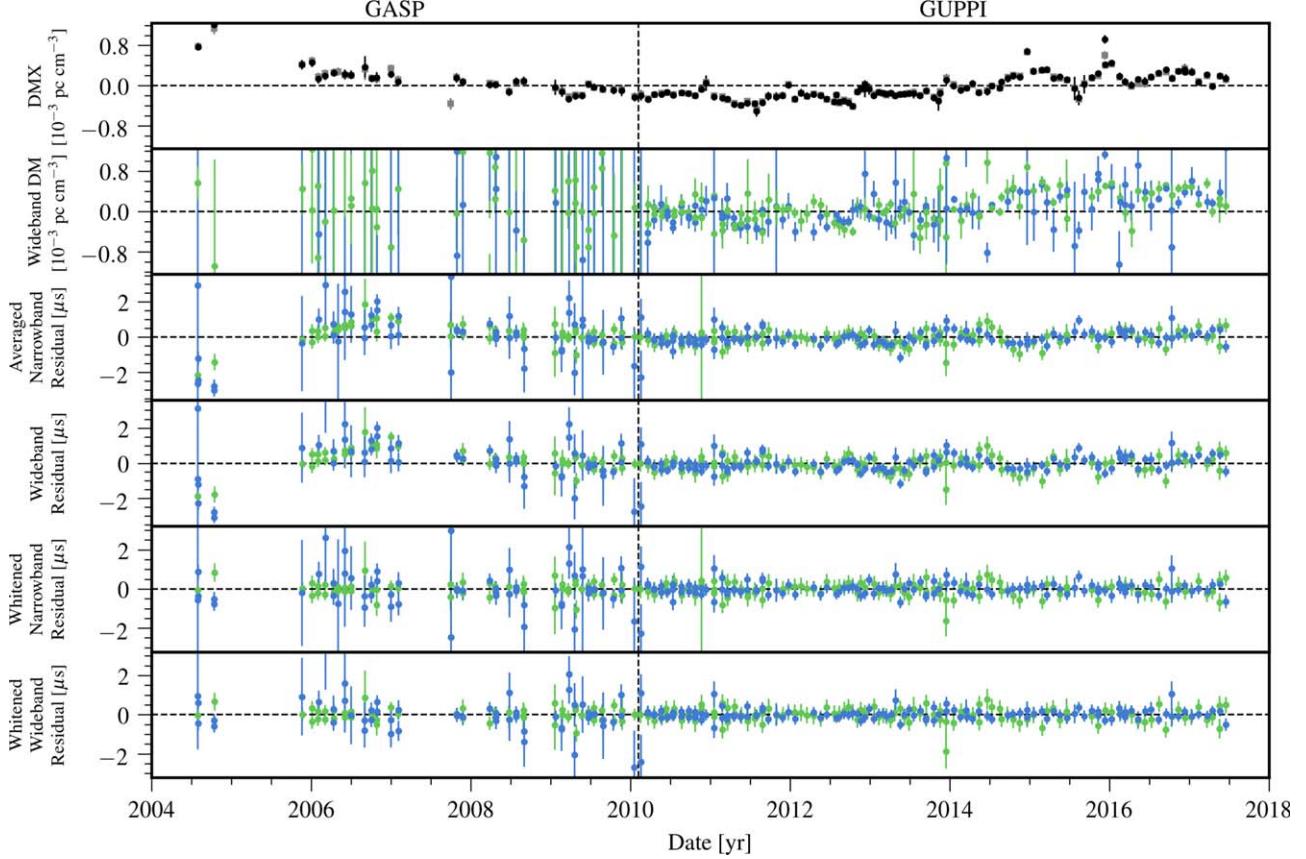

Figure 27. Timing residuals and DM variations for J1738+0333. See Appendix C for details. DMX model parameters from the wideband (black circles) and narrowband (gray squares) data sets are shown in the top panel. Colors in the lower panels indicate the receiver for the observation: 1.4 GHz (light blue) and 2.1 GHz (purple).
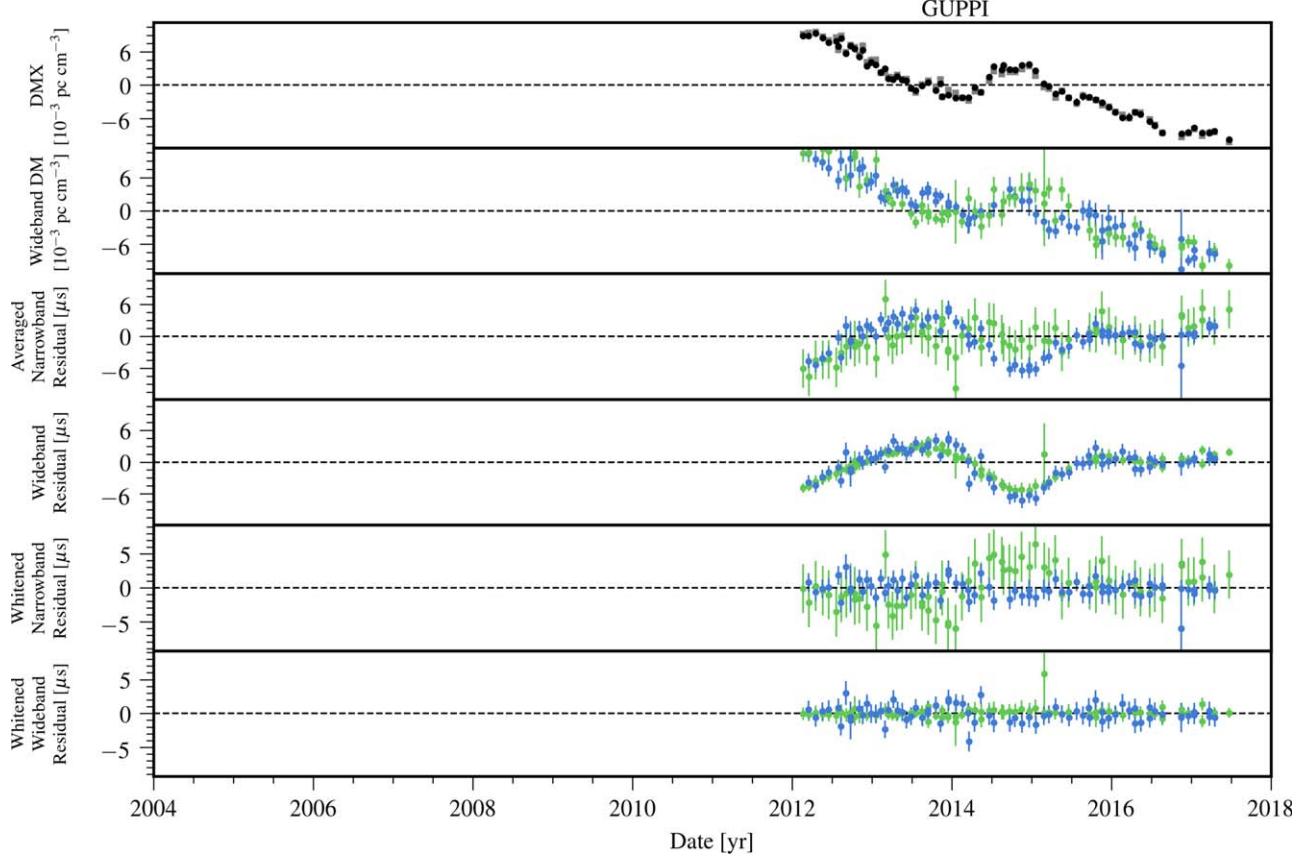
Figure 28. Timing residuals and DM variations for J1741+1351. See Appendix C for details. DMX model parameters from the wideband (black circles) and narrowband (gray squares) data sets are shown in the top panel. Colors in the lower panels indicate the receiver for the observation: 430 MHz (orange) and 1.4 GHz (light blue).
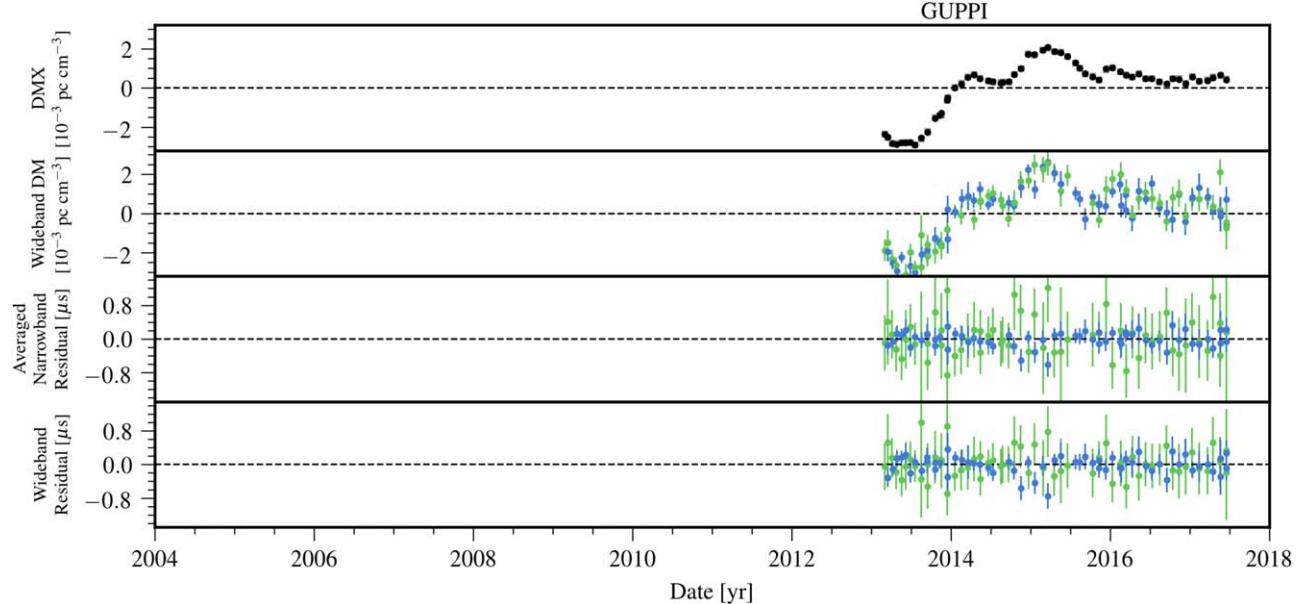
Figure 29. Timing residuals and DM variations for J1744−1134. See Appendix C for details. DMX model parameters from the wideband (black circles) and narrowband (gray squares) data sets are shown in the top panel. Colors in the lower panels indicate the receiver for the observation: 820 MHz (green) and 1.4 GHz (dark blue).

J1747−4036
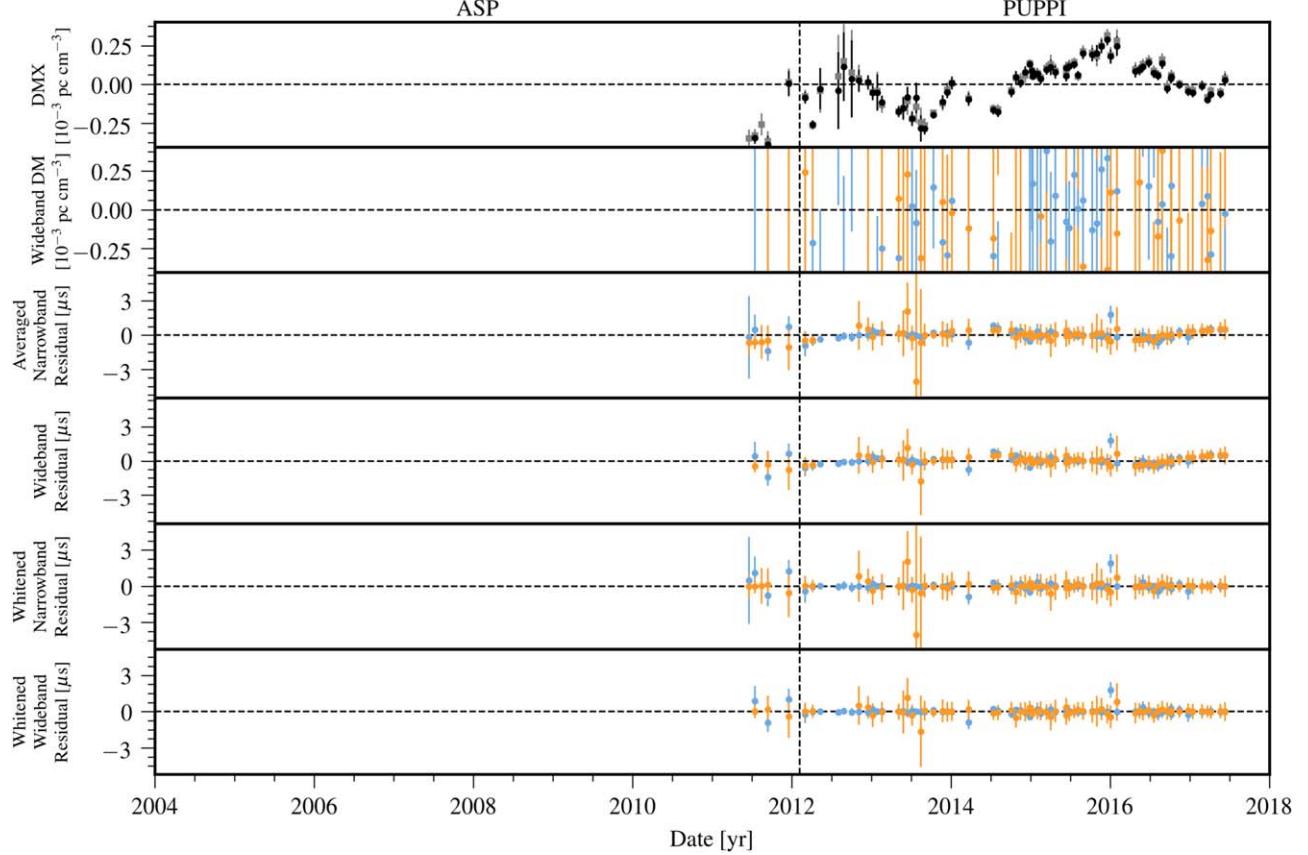
Figure 30. Timing residuals and DM variations for J1747−4036. See Appendix C for details. DMX model parameters from the wideband (black circles) and narrowband (gray squares) data sets are shown in the top panel. Colors in the lower panels indicate the receiver for the observation: 820 MHz (green) and 1.4 GHz (dark blue).

J1832−0836
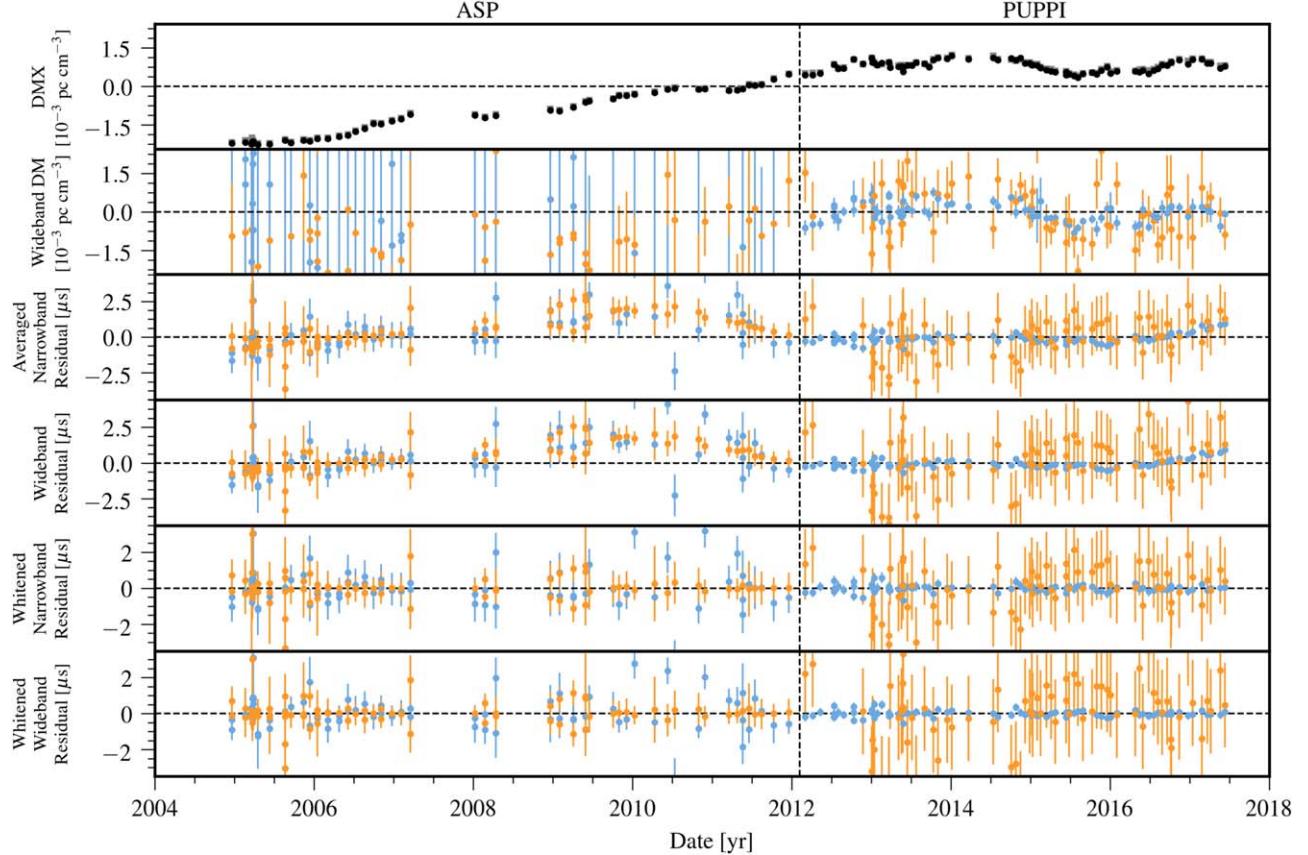
Figure 31. Timing residuals and DM variations for J1832−0836. See Appendix C for details. DMX model parameters from the wideband (black circles) and narrowband (gray squares) data sets are shown in the top panel. Colors in the lower panels indicate the receiver for the observation: 820 MHz (green) and 1.4 GHz (dark blue).
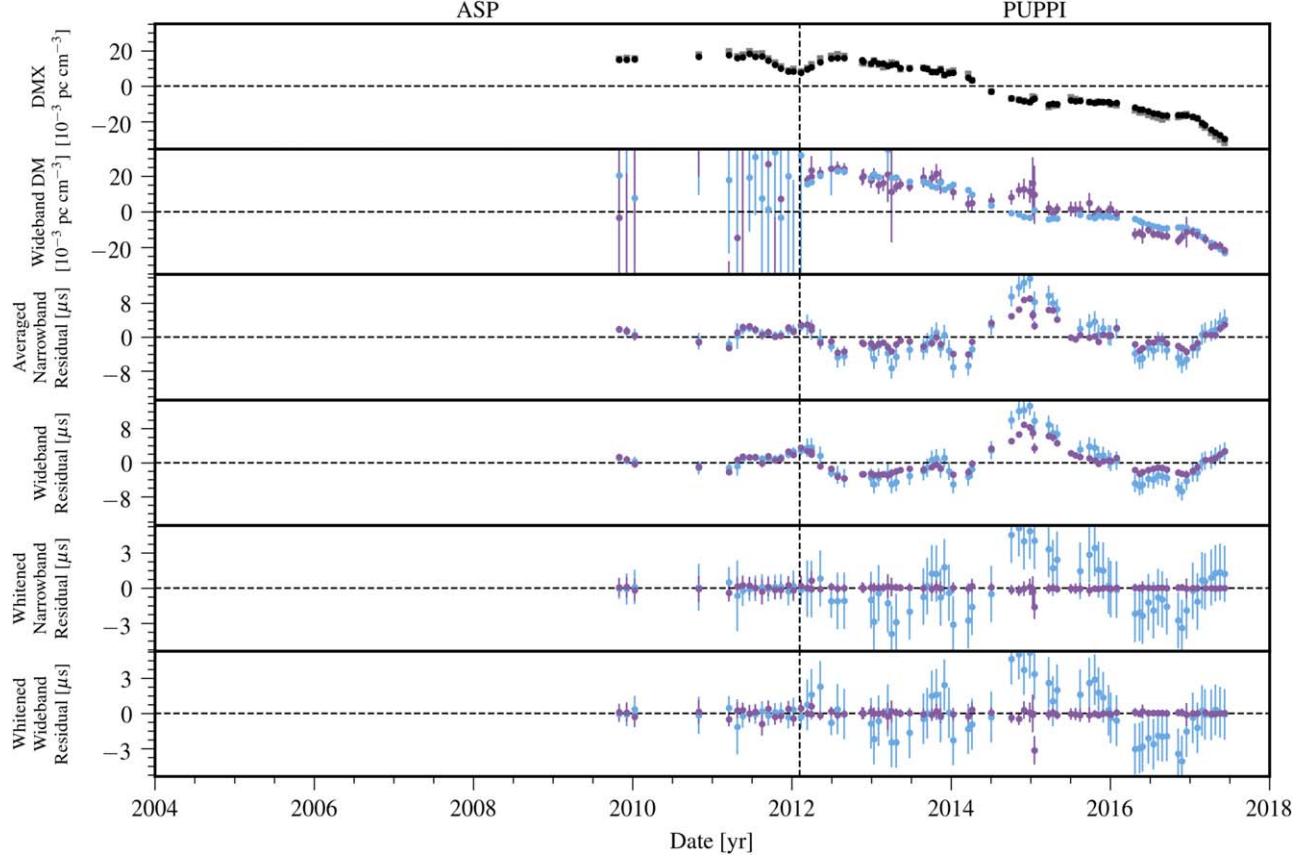
Figure 32. Timing residuals and DM variations for J1853+1303. See Appendix C for details. DMX model parameters from the wideband (black circles) and narrowband (gray squares) data sets are shown in the top panel. Colors in the lower panels indicate the receiver for the observation: 430 MHz (orange) and 1.4 GHz (light blue).
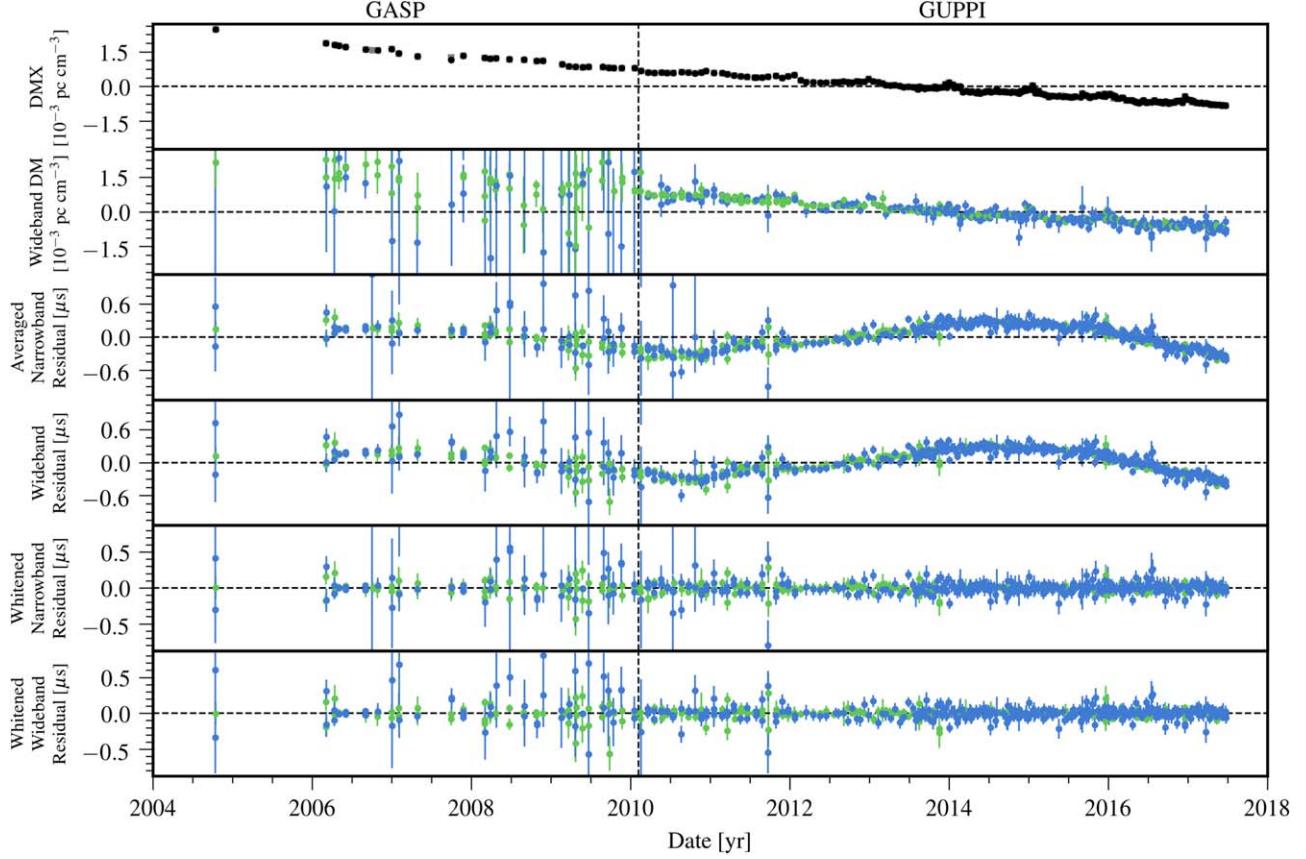
Figure 33. Timing residuals and DM variations for B1855+09. See Appendix C for details. DMX model parameters from the wideband (black circles) and narrowband (gray squares) data sets are shown in the top panel. Colors in the lower panels indicate the receiver for the observation: 430 MHz (orange) and 1.4 GHz (light blue).
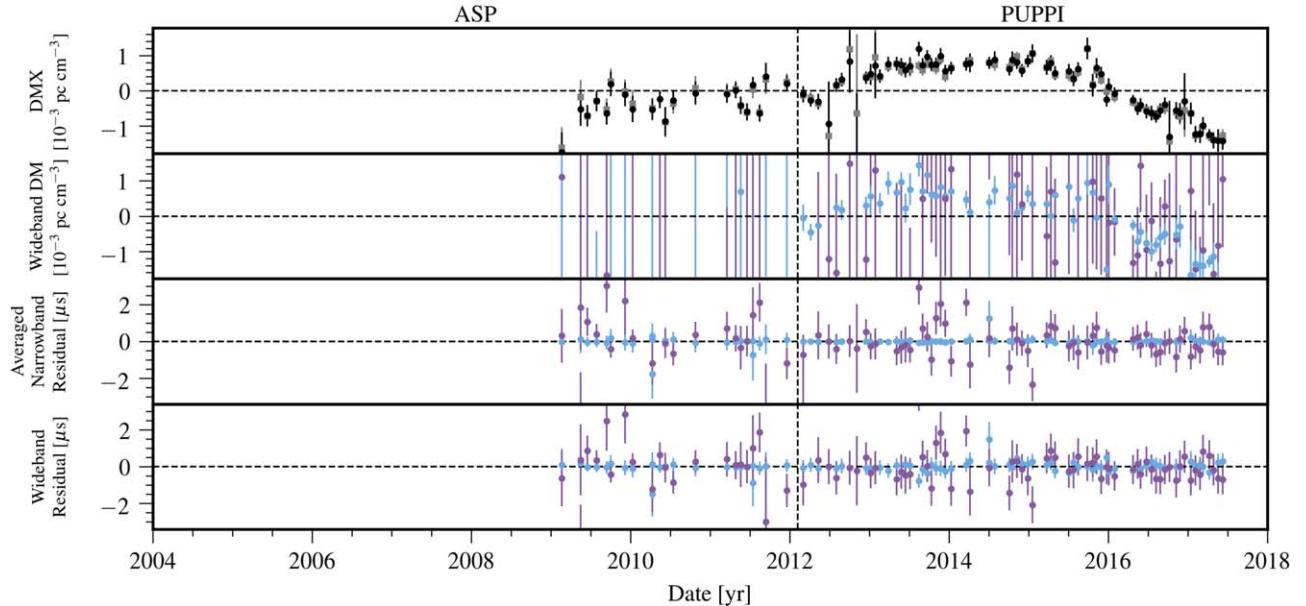
Figure 34. Timing residuals and DM variations for J1903+0327. See Appendix C for details. DMX model parameters from the wideband (black circles) and narrowband (gray squares) data sets are shown in the top panel. Colors in the lower panels indicate the receiver for the observation: 1.4 GHz (light blue) and 2.1 GHz (purple).

J1909−3744
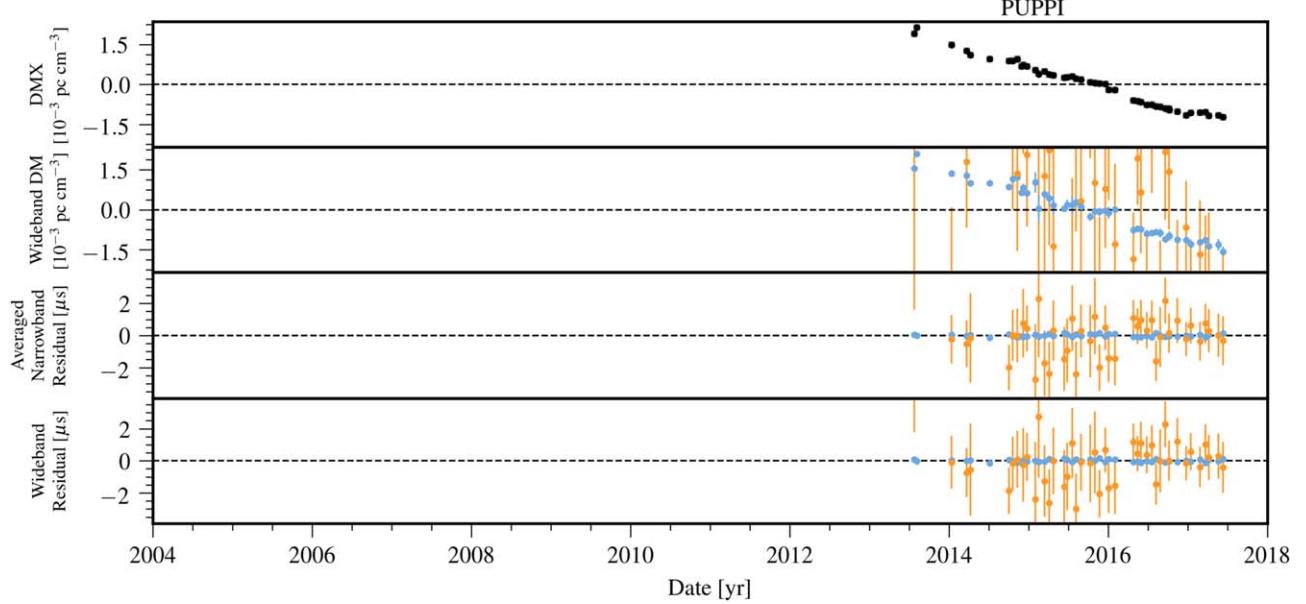
Figure 35. Timing residuals and DM variations for J1909−3744. See Appendix C for details. DMX model parameters from the wideband (black circles) and narrowband (gray squares) data sets are shown in the top panel. Colors in the lower panels indicate the receiver for the observation: 820 MHz (green) and 1.4 GHz (dark blue).

J1910+1256
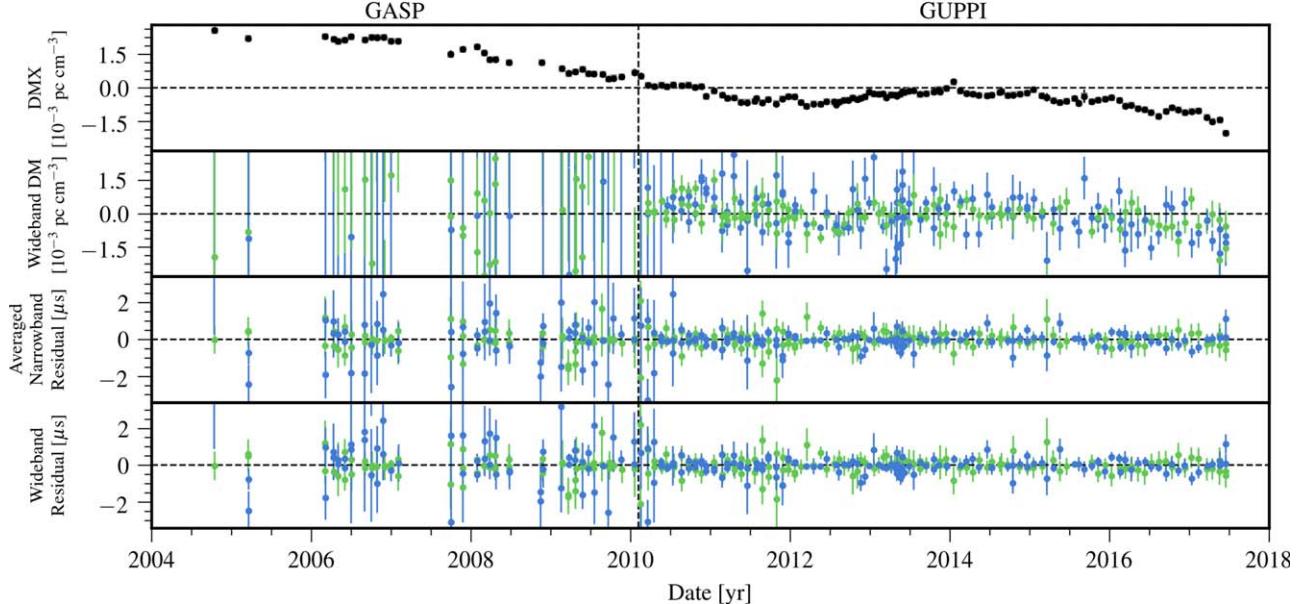
Figure 36. Timing residuals and DM variations for J1910+1256. See Appendix C for details. DMX model parameters from the wideband (black circles) and narrowband (gray squares) data sets are shown in the top panel. Colors in the lower panels indicate the receiver for the observation: 1.4 GHz (light blue) and 2.1 GHz (purple).

J1911+1347
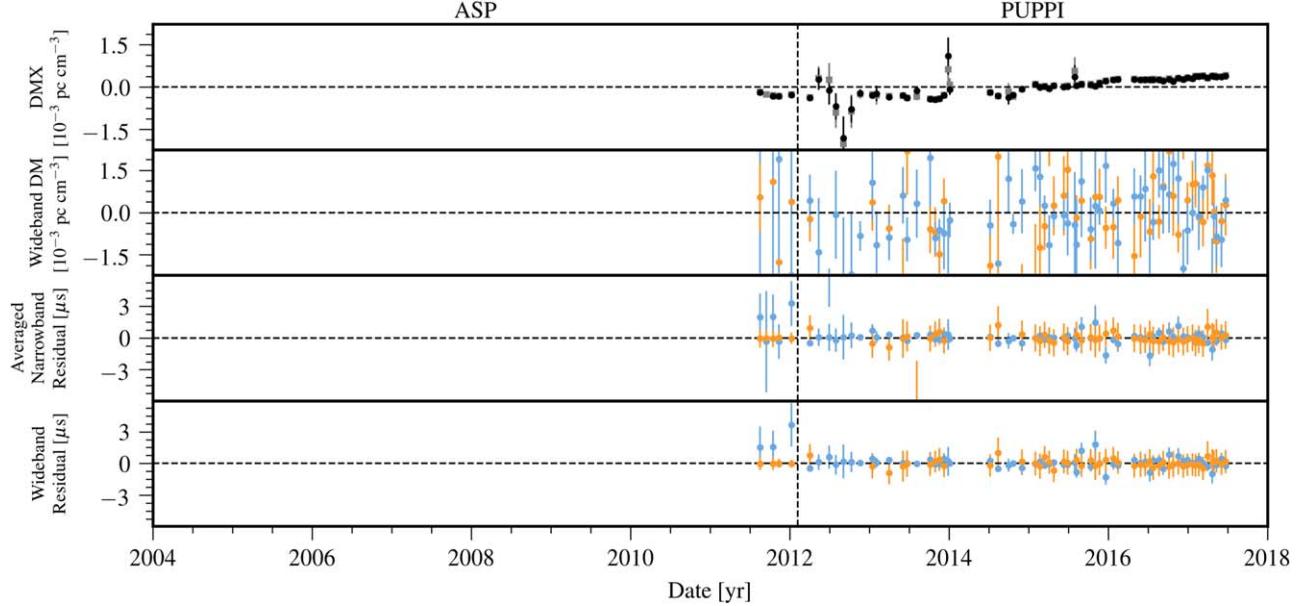
Figure 37. Timing residuals and DM variations for J1911+1347. See Appendix C for details. DMX model parameters from the wideband (black circles) and narrowband (gray squares) data sets are shown in the top panel. Colors in the lower panels indicate the receiver for the observation: 430 MHz (orange) and 1.4 GHz (light blue).

J1918−0642
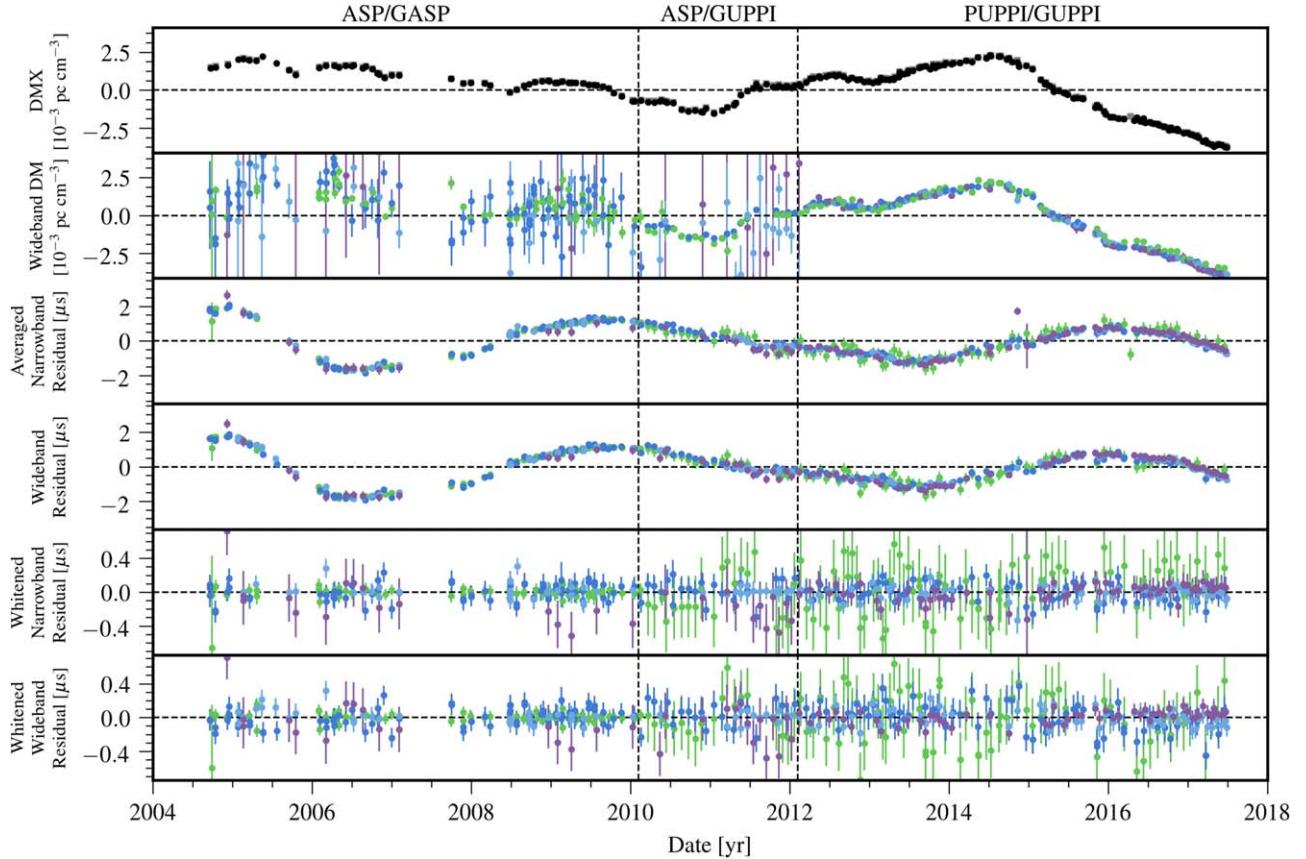
Figure 38. Timing residuals and DM variations for J1918−0642. See Appendix C for details. DMX model parameters from the wideband (black circles) and narrowband (gray squares) data sets are shown in the top panel. Colors in the lower panels indicate the receiver for the observation: 820 MHz (green) and 1.4 GHz (dark blue).

J1923+2515
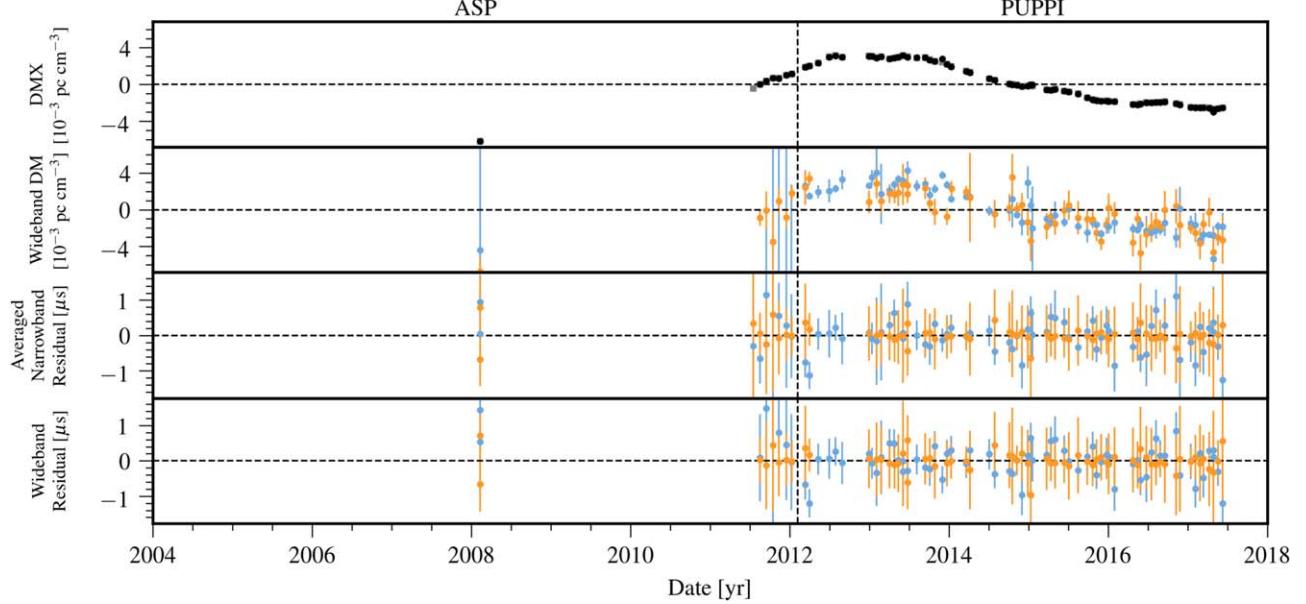
Figure 39. Timing residuals and DM variations for J1923+2515. See Appendix C for details. DMX model parameters from the wideband (black circles) and narrowband (gray squares) data sets are shown in the top panel. Colors in the lower panels indicate the receiver for the observation: 430 MHz (orange) and 1.4 GHz (light blue).

B1937+21
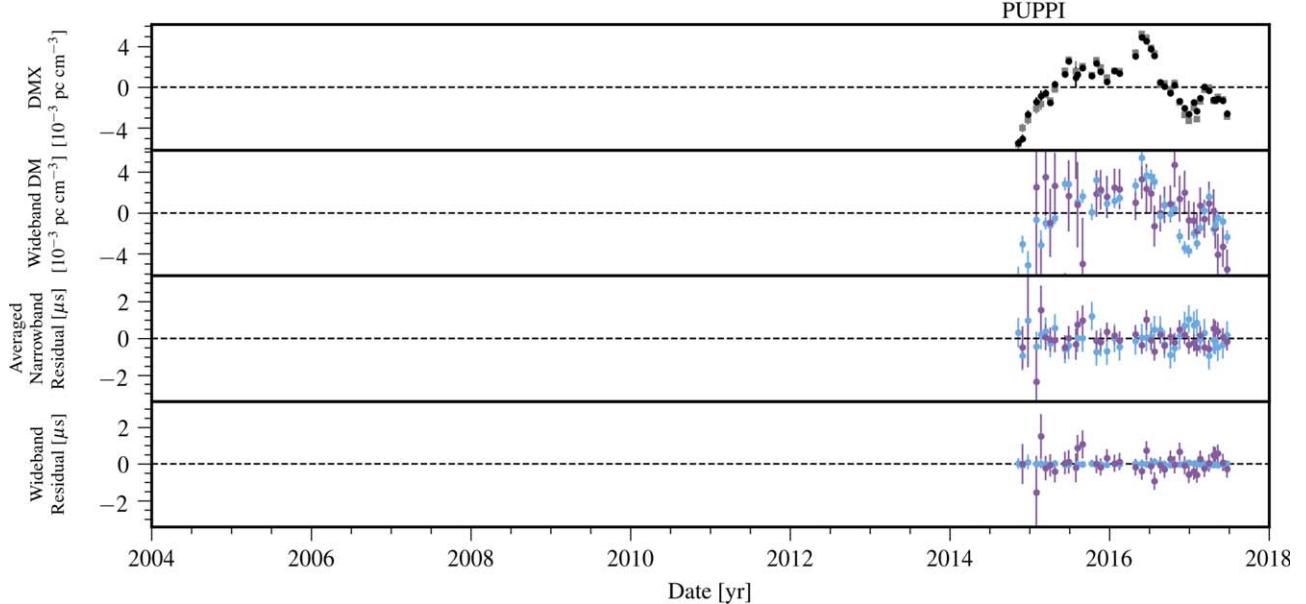
Figure 40. Timing residuals and DM variations for B1937+21. See Appendix C for details. DMX model parameters from the wideband (black circles) and narrowband (gray squares) data sets are shown in the top panel. Colors in the lower panels indicate the receiver for the observation: 820 MHz (green), 1.4 GHz (dark blue), 1.4 GHz (light blue), and 2.1 GHz (purple).

J1944+0907
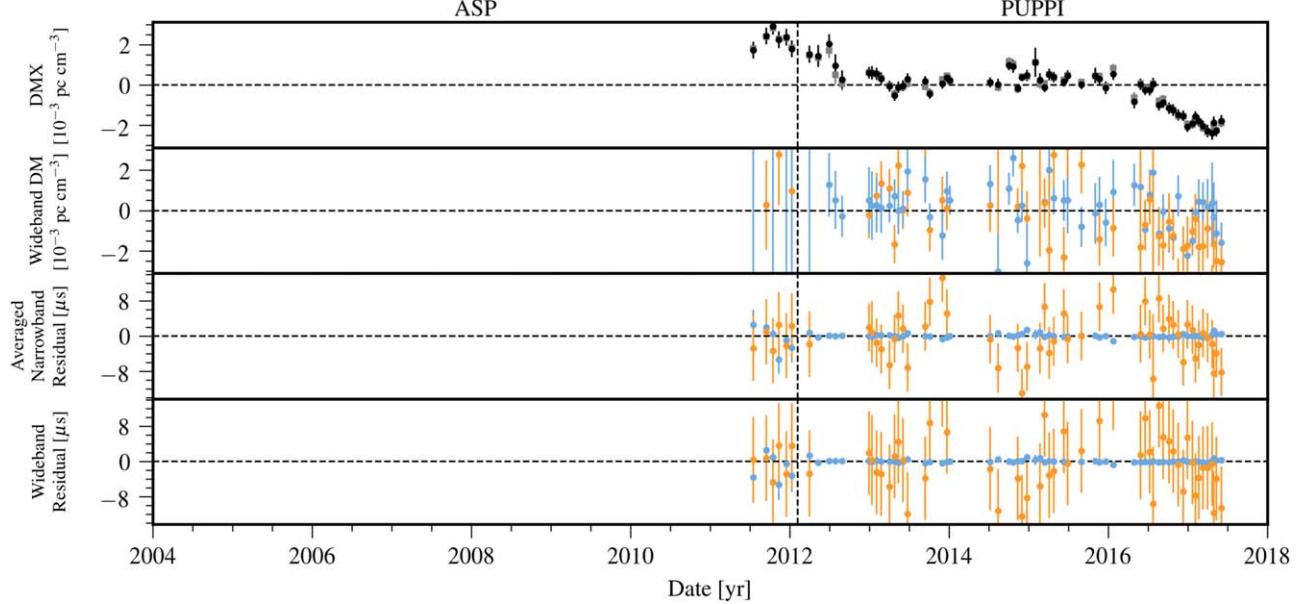
Figure 41. Timing residuals and DM variations for J1944+0907. See Appendix C for details. DMX model parameters from the wideband (black circles) and narrowband (gray squares) data sets are shown in the top panel. Colors in the lower panels indicate the receiver for the observation: 430 MHz (orange) and 1.4 GHz (light blue).

J1946+3417
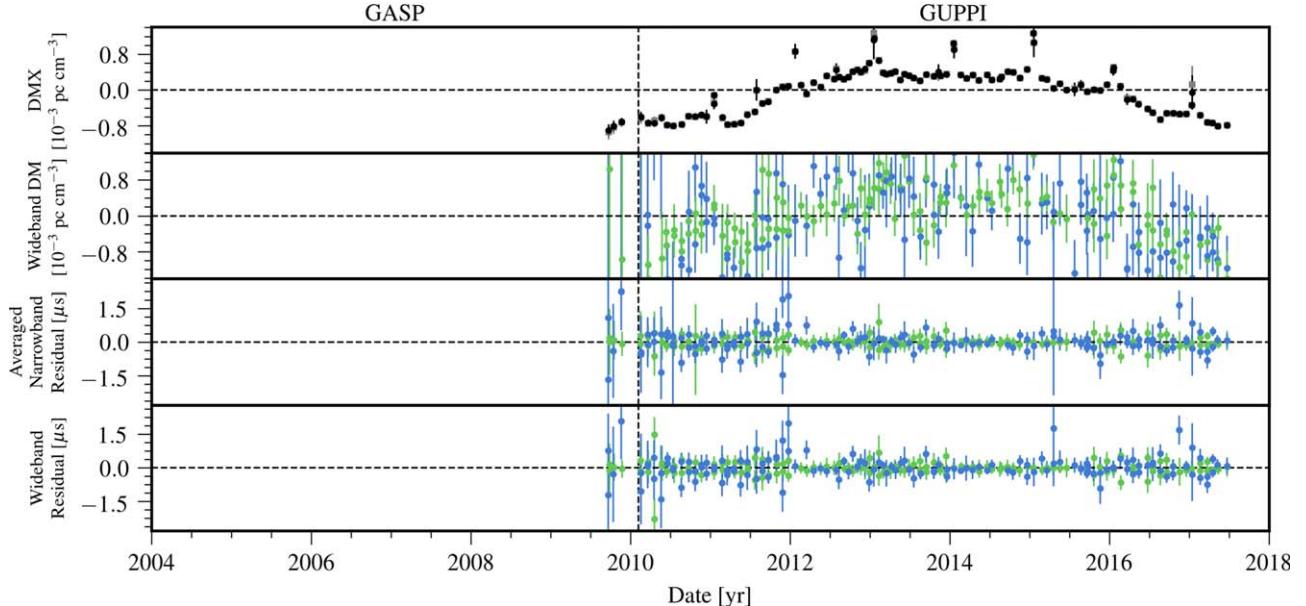
Figure 42. Timing residuals and DM variations for J1946+3417. See Appendix C for details. DMX model parameters from the wideband (black circles) and narrowband (gray squares) data sets are shown in the top panel. Colors in the lower panels indicate the receiver for the observation: 1.4 GHz (light blue) and 2.1 GHz (purple).

B1953+29
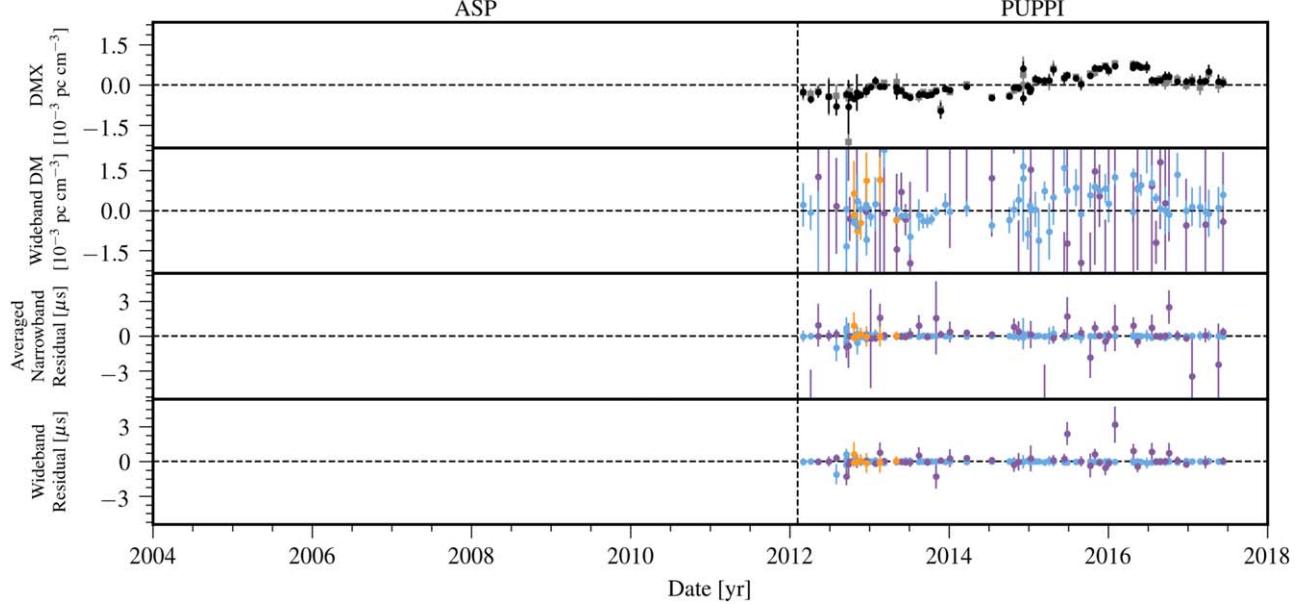
Figure 43. Timing residuals and DM variations for B1953+29. See Appendix C for details. DMX model parameters from the wideband (black circles) and narrowband (gray squares) data sets are shown in the top panel. Colors in the lower panels indicate the receiver for the observation: 430 MHz (orange) and 1.4 GHz (light blue).

J2010−1323
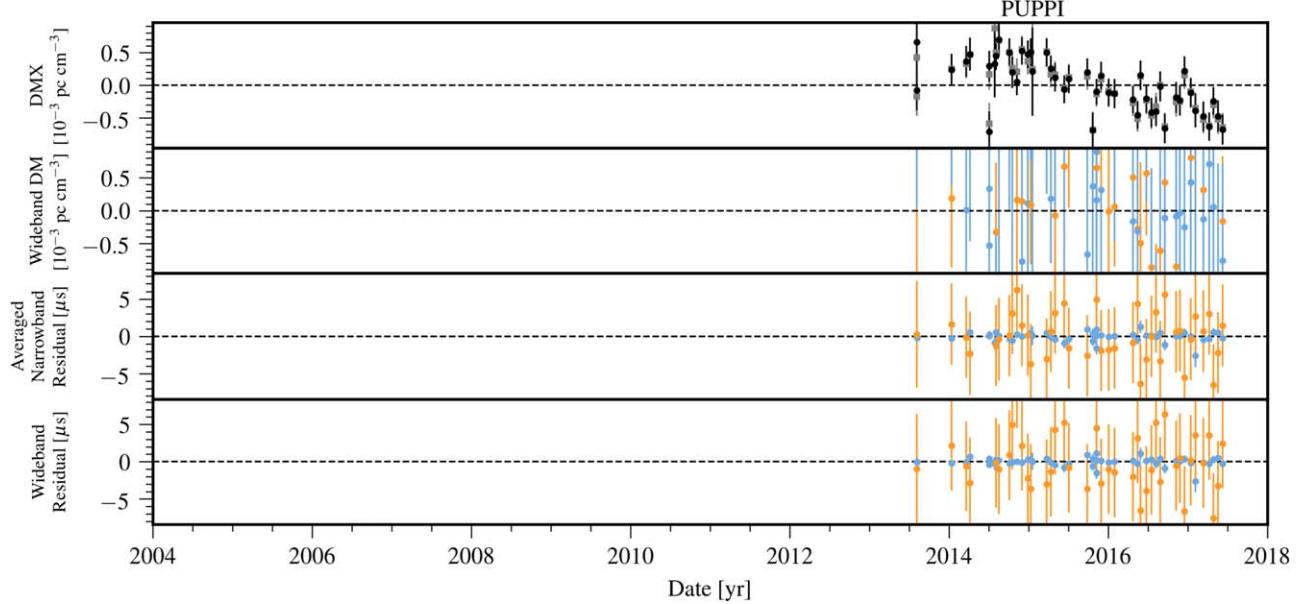
Figure 44. Timing residuals and DM variations for J2010−1323. See Appendix C for details. DMX model parameters from the wideband (black circles) and narrowband (gray squares) data sets are shown in the top panel. Colors in the lower panels indicate the receiver for the observation: 820 MHz (green) and 1.4 GHz (dark blue).
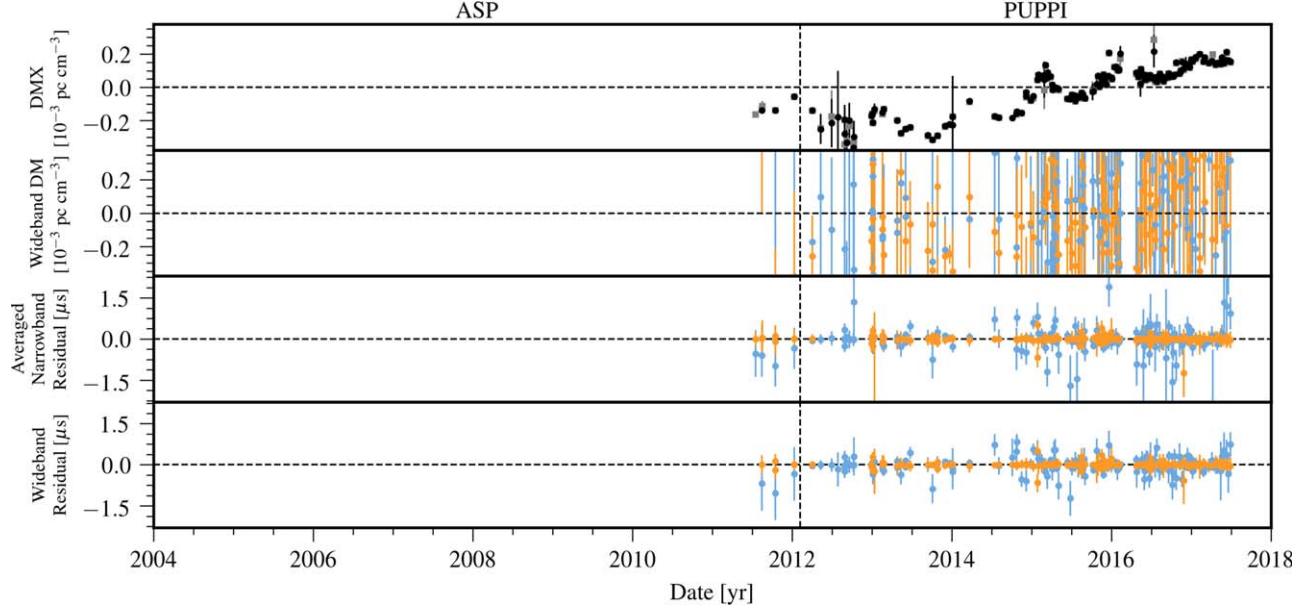
Figure 45. Timing residuals and DM variations for J2017+0603. See Appendix C for details. DMX model parameters from the wideband (black circles) and narrowband (gray squares) data sets are shown in the top panel. Colors in the lower panels indicate the receiver for the observation: 430 MHz (orange), 1.4 GHz (light blue), and 2.1 GHz (purple).
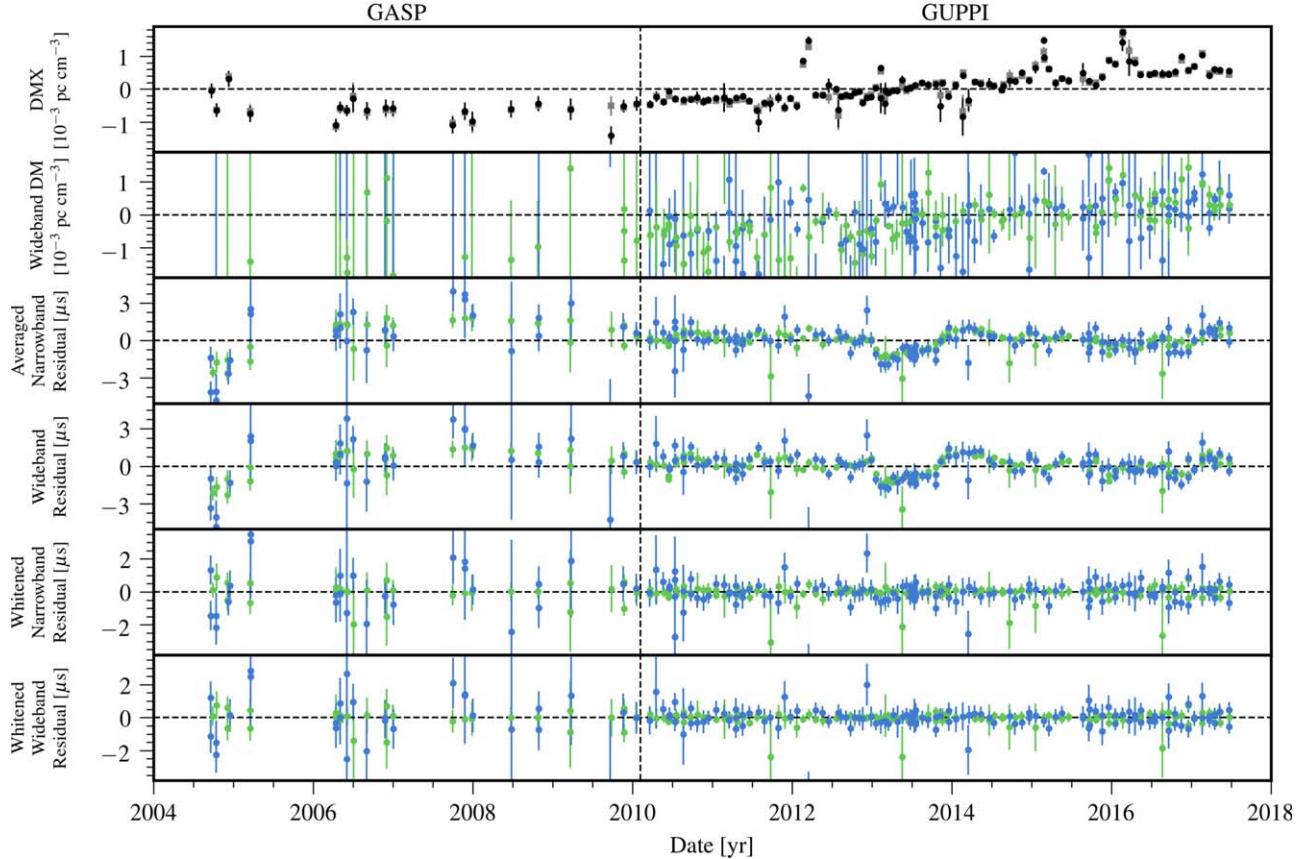
Figure 46. Timing residuals and DM variations for J2033+1734. See Appendix C for details. DMX model parameters from the wideband (black circles) and narrowband (gray squares) data sets are shown in the top panel. Colors in the lower panels indicate the receiver for the observation: 430 MHz (orange) and 1.4 GHz (light blue).

J2043+1711
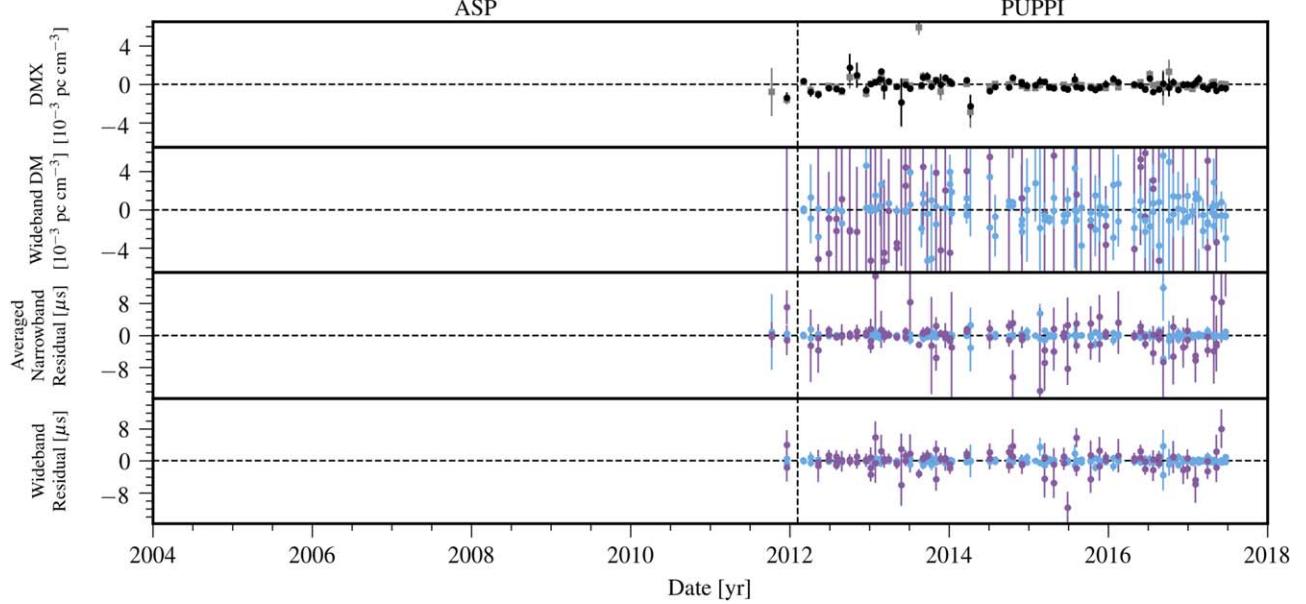
Figure 47. Timing residuals and DM variations for J2043+1711. See Appendix C for details. DMX model parameters from the wideband (black circles) and narrowband (gray squares) data sets are shown in the top panel. Colors in the lower panels indicate the receiver for the observation: 430 MHz (orange) and 1.4 GHz (light blue).

J2145−0750
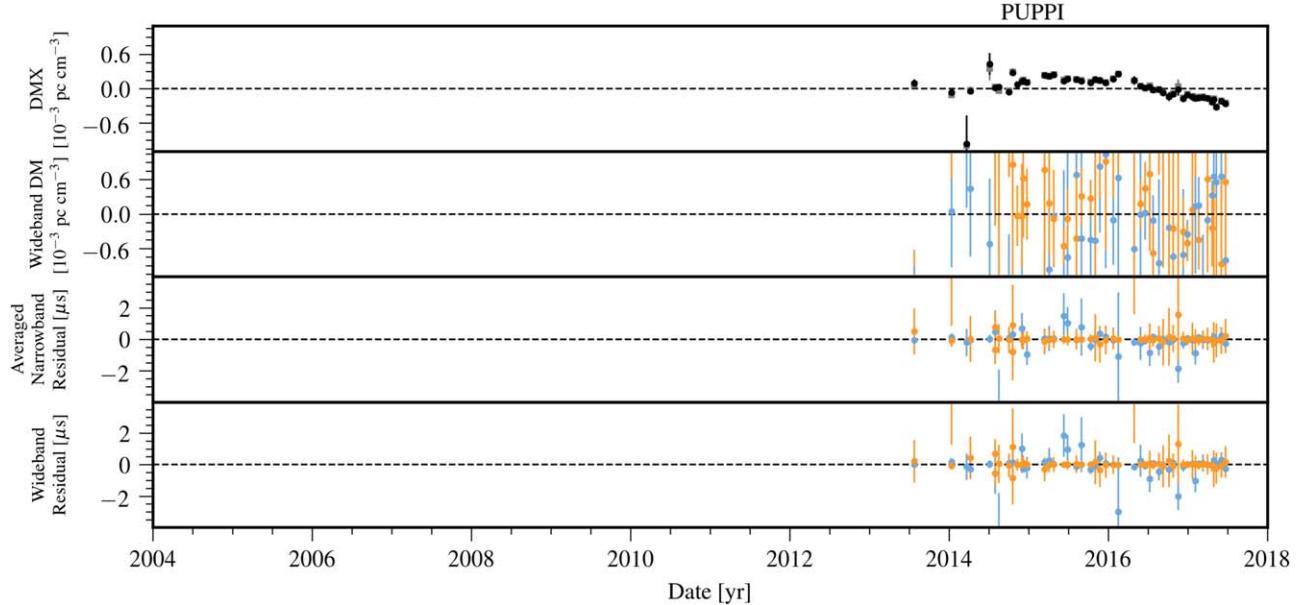
Figure 48. Timing residuals and DM variations for J2145−0750. See Appendix C for details. DMX model parameters from the wideband (black circles) and narrowband (gray squares) data sets are shown in the top panel. Colors in the lower panels indicate the receiver for the observation: 820 MHz (green) and 1.4 GHz (dark blue).
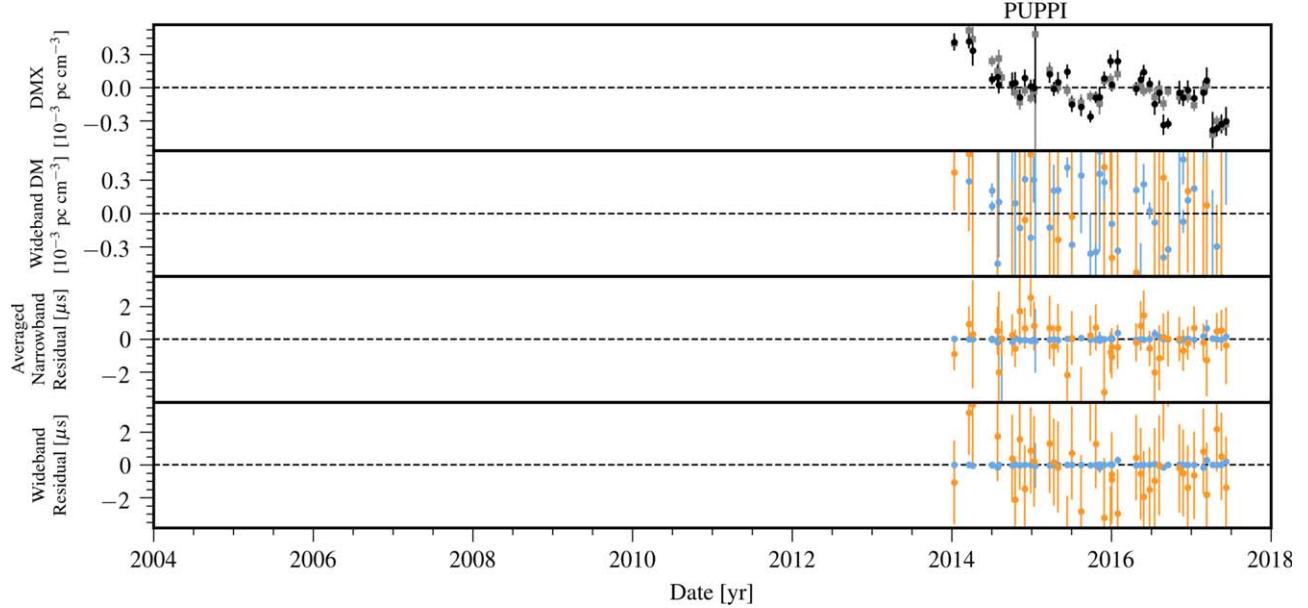
Figure 49. Timing residuals and DM variations for J2214+3000. See Appendix C for details. DMX model parameters from the wideband (black circles) and narrowband (gray squares) data sets are shown in the top panel. Colors in the lower panels indicate the receiver for the observation: 1.4 GHz (light blue) and 2.1 GHz (purple).
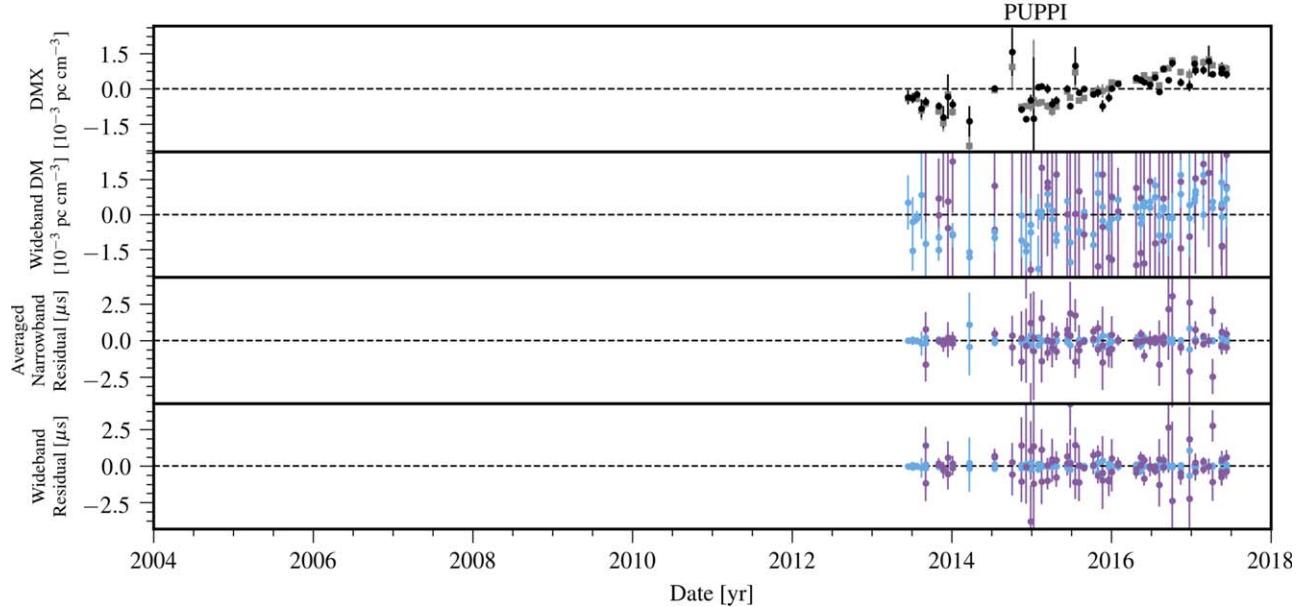
Figure 50. Timing residuals and DM variations for J2229+2643. See Appendix C for details. DMX model parameters from the wideband (black circles) and narrowband (gray squares) data sets are shown in the top panel. Colors in the lower panels indicate the receiver for the observation: 430 MHz (orange) and 1.4 GHz (light blue).

J2234+0611
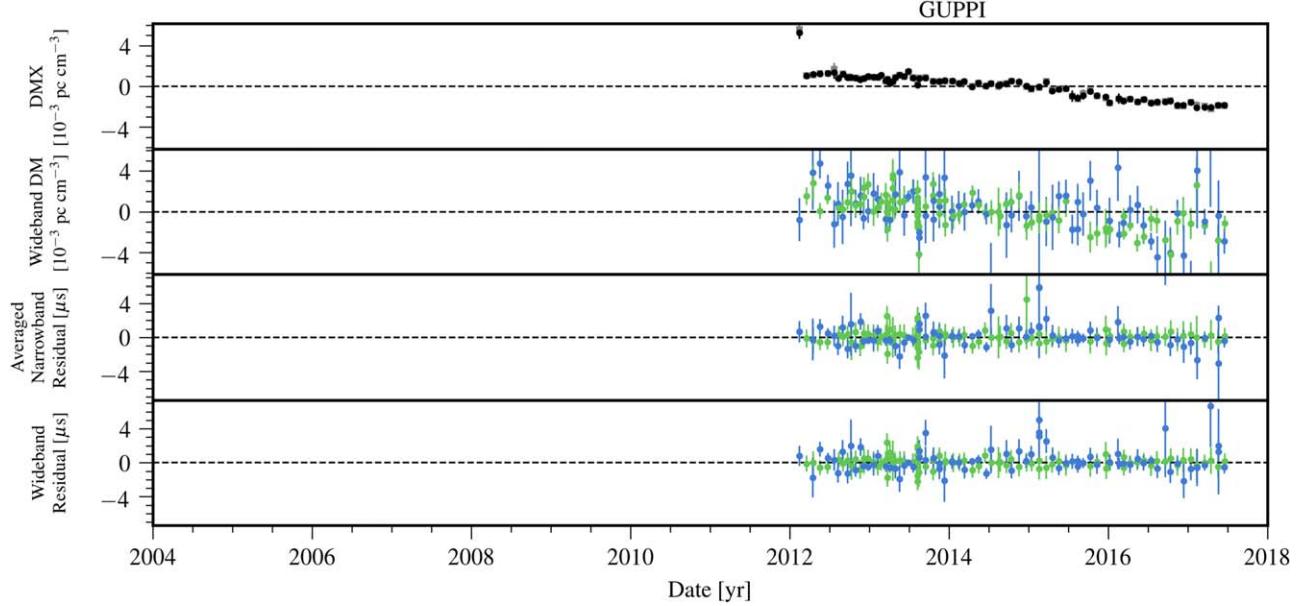
Figure 51. Timing residuals and DM variations for J2234+0611. See Appendix C for details. DMX model parameters from the wideband (black circles) and narrowband (gray squares) data sets are shown in the top panel. Colors in the lower panels indicate the receiver for the observation: 430 MHz (orange) and 1.4 GHz (light blue).

J2234+0944
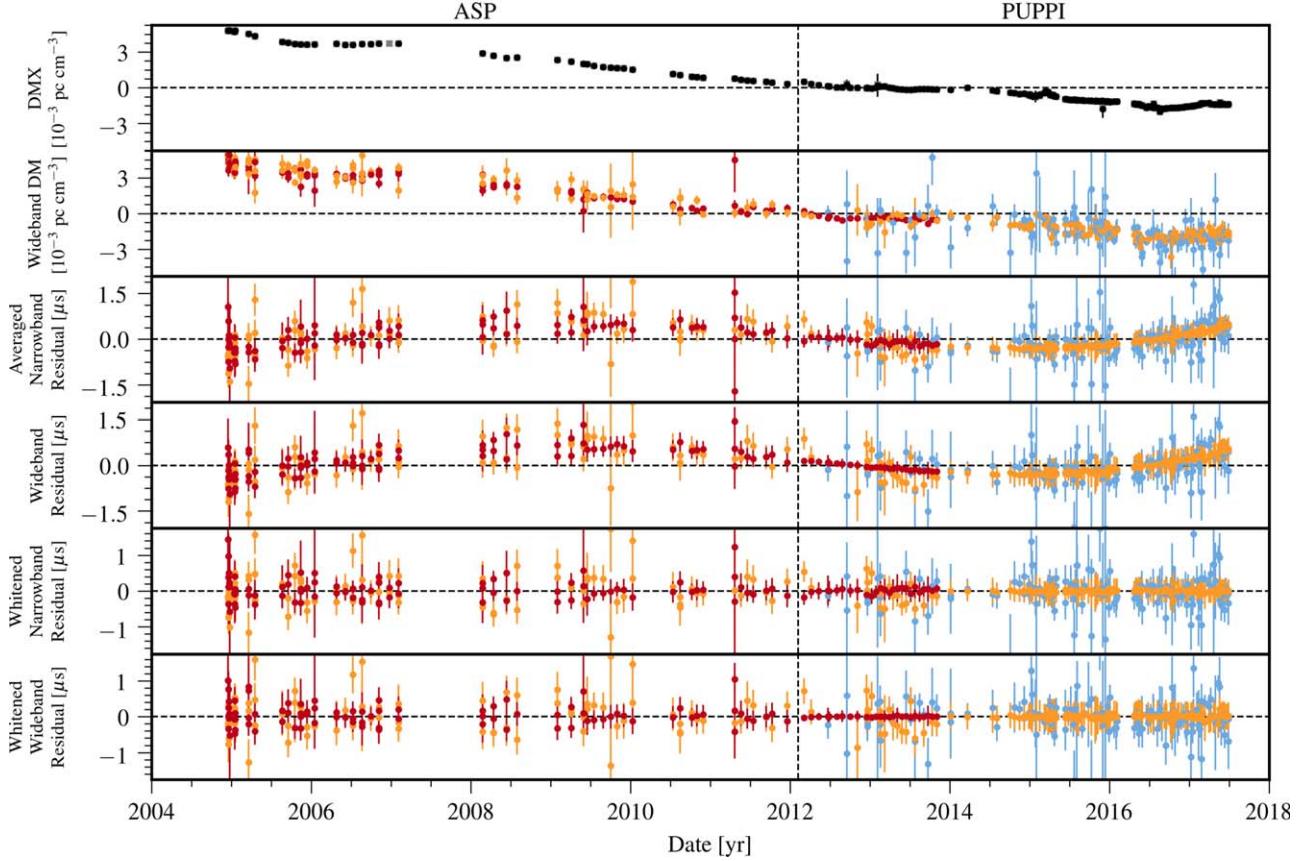
Figure 52. Timing residuals and DM variations for J2234+0944. See Appendix C for details. DMX model parameters from the wideband (black circles) and narrowband (gray squares) data sets are shown in the top panel. Colors in the lower panels indicate the receiver for the observation: 1.4 GHz (light blue) and 2.1 GHz (purple).

J2302+4442
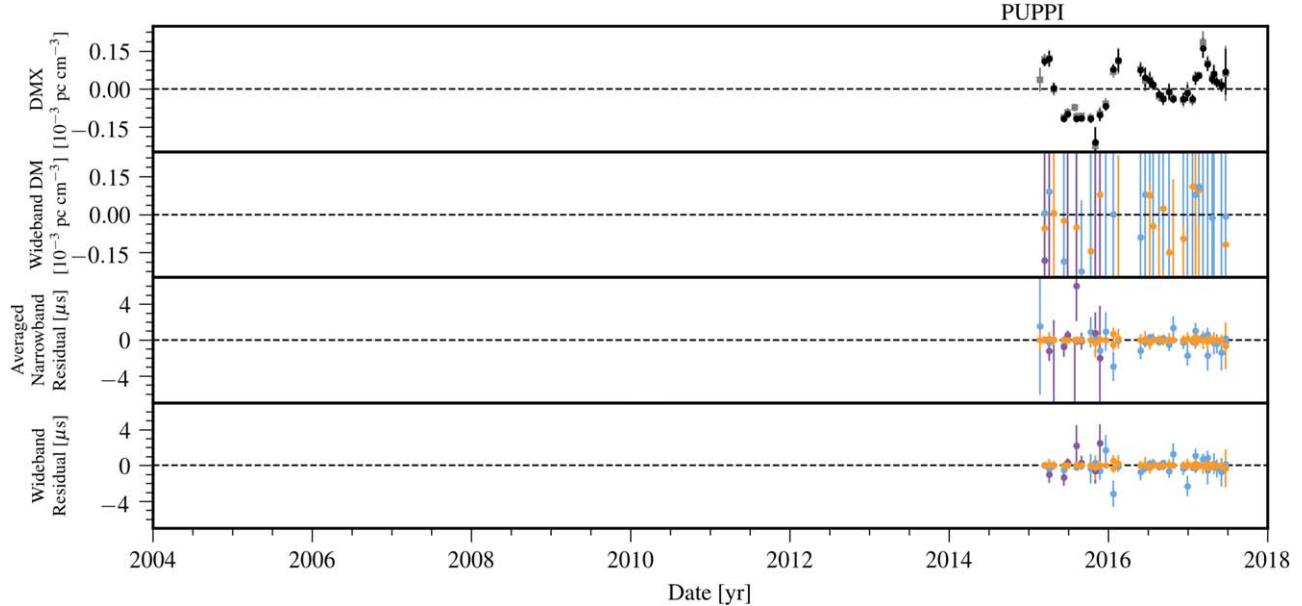
Figure 53. Timing residuals and DM variations for J2302+4442. See Appendix C for details. DMX model parameters from the wideband (black circles) and narrowband (gray squares) data sets are shown in the top panel. Colors in the lower panels indicate the receiver for the observation: 820 MHz (green) and 1.4 GHz (dark blue).

J2317+1439

Figure 54. Timing residuals and DM variations for J2317+1439. See Appendix C for details. DMX model parameters from the wideband (black circles) and narrowband (gray squares) data sets are shown in the top panel. Colors in the lower panels indicate the receiver for the observation: 327 MHz (Red), 430 MHz (orange), and 1.4 GHz (light blue).

J2322+2057

Figure 55. Timing residuals and DM variations for J2322+2057. See Appendix C for details. DMX model parameters from the wideband (black circles) and narrowband (gray squares) data sets are shown in the top panel. Colors in the lower panels indicate the receiver for the observation: 430 MHz (orange), 1.4 GHz (light blue), and 2.1 GHz (purple).

ORCID iDs

Md F. Alam ● https://orcid.org/0000-0003-2449-5426
Paul T. Baker ● https://orcid.org/0000-0003-2745-753X
Harsha Blumer ● https://orcid.org/0000-0003-4046-884X
Paul R. Brook ● https://orcid.org/0000-0001-5645-5336
Sarah Burke-Spolaor ● https://orcid.org/0000-0003-4052-7838
Shami Chatterjee ● https://orcid.org/0000-0002-2878-1502
James M. Cordes ● https://orcid.org/0000-0002-4049-1882
Neil J. Cornish ● https://orcid.org/0000-0002-7435-0869
Fronefield Crawford ● https://orcid.org/0000-0002-2578-0360
H. Thankful Cromartie ● https://orcid.org/0000-0002-6039-692X
Megan E. DeCesar ● https://orcid.org/0000-0002-2185-1790
Paul B. Demorest ● https://orcid.org/0000-0002-6664-965X
Timothy Dolch ● https://orcid.org/0000-0001-8885-6388
Robert D. Ferdman ● https://orcid.org/0000-0002-2223-1235
Elizabeth C. Ferrara ● https://orcid.org/0000-0001-7828-7708
Emmanuel Fonseca ● https://orcid.org/0000-0001-8384-5049
Nathan Garver-Daniels ● https://orcid.org/0000-0001-6166-9646
Peter A. Gentile ● https://orcid.org/0000-0001-8158-683X
Deborah C. Good ● https://orcid.org/0000-0003-1884-348X
Jordan A. Gusdorff ● https://orcid.org/0000-0001-6609-2997
Daniel Halmrast ● https://orcid.org/0000-0003-2289-2575
Jeffrey S. Hazboun ● https://orcid.org/0000-0003-2742-3321
Ross J. Jennings ● https://orcid.org/0000-0003-1082-2342
Cody Jessup ● https://orcid.org/0000-0002-4188-6827
Megan L. Jones ● https://orcid.org/0000-0001-6607-3710
Andrew R. Kaiser ● https://orcid.org/0000-0002-3654-980X
David L. Kaplan ● https://orcid.org/0000-0001-6295-2881
Luke Zoltan Kelley ● https://orcid.org/0000-0002-6625-6450
Joey Shapiro Key ● https://orcid.org/0000-0003-0123-7600
Michael T. Lam ● https://orcid.org/0000-0003-0721-651X
Duncan R. Lorimer ● https://orcid.org/0000-0003-1301-966X
Jing Luo ● https://orcid.org/0000-0001-5373-5914
Ryan S. Lynch ● https://orcid.org/0000-0001-5229-7430
Dustin R. Madison ● https://orcid.org/0000-0003-2285-0404

Maura A. McLaughlin ● https://orcid.org/0000-0001-7697-7422
Chiara M. F. Mingarelli ● https://orcid.org/0000-0002-4307-1322
Cherry Ng ● https://orcid.org/0000-0002-3616-5160
David J. Nice ● https://orcid.org/0000-0002-6709-2566
Timothy T. Pennucci ● https://orcid.org/0000-0001-5465-2889
Nihan S. Pol ● https://orcid.org/0000-0002-8826-1285
Joshua Ramette ● https://orcid.org/0000-0002-4709-6236
Scott M. Ransom ● https://orcid.org/0000-0001-5799-9714
Paul S. Ray ● https://orcid.org/0000-0002-5297-5278
Brent J. Shapiro-Albert ● https://orcid.org/0000-0002-7283-1124
Xavier Siemens ● https://orcid.org/0000-0002-7778-2990
Joseph Simon ● https://orcid.org/0000-0003-1407-6607
Renée Spiewak ● https://orcid.org/0000-0002-6730-3298
Ingrid H. Stairs ● https://orcid.org/0000-0001-9784-8670
Daniel R. Stinebring ● https://orcid.org/0000-0002-1797-3277
Kevin Stovall ● https://orcid.org/0000-0002-7261-594X
Joseph K. Swiggum ● https://orcid.org/0000-0002-1075-3837
Stephen R. Taylor ● https://orcid.org/0000-0003-0264-1453
Michael Tripepi ● https://orcid.org/0000-0002-4657-9826
Michele Vallisneri ● https://orcid.org/0000-0002-4162-0033
Sarah J. Vigeland ● https://orcid.org/0000-0003-4700-9072
Caitlin A. Witt ● https://orcid.org/0000-0002-6020-9274
Weiwei Zhu ● https://orcid.org/0000-0001-5105-4058

References

Alam, Md F., Arzoumanian, Z., Baker, P. T., et al. 2020, ApJS, 252, 5
Antoniadis, J. 2014, ApJL, 797, L24
Arzoumanian, Z., Baker, P. T., Blumer, H., et al. 2020, arXiv:2009.04496
Arzoumanian, Z., Baker, P. T., Brazier, A., et al. 2018a, ApJ, 859, 47
Arzoumanian, Z., Brazier, A., Burke-Spolaor, S., et al. 2014, ApJ, 794, 141
Arzoumanian, Z., Brazier, A., Burke-Spolaor, S., et al. 2015, ApJ, 813, 65
Arzoumanian, Z., Brazier, A., Burke-Spolaor, S., et al. 2018b, ApJS, 235, 37
Bailes, M., Barr, E., Bhat, N. D. R., et al. 2018, arXiv:1803.07424
Bailes, M., Jameson, A., Abbate, F., et al. 2020, PASA, 37, e028
Bak Nielsen, A.-S., Janssen, G. H., Shaifullah, G., et al. 2020, MNRAS, 494, 2591

Barr, E. D., Freire, P. C. C., Kramer, M., et al. 2017, MNRAS, 465, 1711
Brook, P. R., Karastergiou, A., McLaughlin, M. A., et al. 2018, ApJ, 868, 122
Burke-Spolaor, S., Taylor, S. R., Charisi, M., et al. 2019, A&ARv, 27, 5
Burt, B. J., Lommen, A. N., & Finn, L. S. 2011, ApJ, 730, 17
Cordes, J., McLaughlin, M. A. & Nanograv Collaboration 2019, BAAS, 51, 447
Cordes, J. M., & Downs, G. S. 1985, ApJS, 59, 343
Cordes, J. M., & Shannon, R. M. 2010, arXiv:1010.3785
Cordes, J. M., Shannon, R. M., & Stinebring, D. R. 2016, ApJ, 817, 16
Cordes, J. M., Wolszczan, A., Dewey, R. J., Blaskiewicz, M., & Stinebring, D. R. 1990, ApJ, 349, 245
D'Alessandro, F., McCulloch, P. M., Hamilton, P. A., & Deshpande, A. A. 1995, MNRAS, 277, 1033
Demorest, P. B. 2007, PhD thesis, University of California, Berkeley
Demorest, P. B. 2018, nanopipe: Calibration and Data Reduction Pipeline for Pulsar Timing, Astrophysics Source Code Library, ascl:1803.004
Demorest, P. B., Ferdman, R. D., Gonzalez, M. E., et al. 2013, ApJ, 762, 94
Deng, Z.-L., Gao, Z.-F., Li, X.-D., & Shao, Y. 2020, ApJ, 892, 4
Desvignes, G., Caballero, R. N., Lentati, L., et al. 2016, MNRAS, 458, 3341
Dickey, J. M. 1971, Ann. Math. Statist., 42, 204
Donner, J. Y., Verbiest, J. P. W., Tiburzi, C., et al. 2019, A&A, 624, A22
Driessen, L. N., Janssen, G. H., Bassa, C. G., Stappers, B. W., & Stinebring, D. R. 2019, MNRAS, 483, 1224
DuPlain, R., Ransom, S., Demorest, P., et al. 2008, Proc. SPIE, 7019, 70191D
Edwards, R. T., Hobbs, G. B., & Manchester, R. N. 2006, MNRAS, 372, 1549
Ellis, J., & van Haasteren, R. 2017, jellis18/PTMCMCSampler: Official Release v1.0.0, Zenodo, doi:10.5281/zenodo.1037579
Ellis, J. A., Siemens, X., & van Haasteren, R. 2013, ApJ, 769, 63
Ellis, J. A., Vallisneri, M., Taylor, S. R., & Baker, P. T. 2019, ENTERPRISE: Enhanced Numerical Toolbox Enabling a Robust PulsaR Inference SuitE, Astrophysics Source Code Library, ascl:1912.015
Fonseca, E., Demorest, P., Ransom, S., & Stairs, I. 2019, BAAS, 51, 425
Fonseca, E., Pennucci, T. T., Ellis, J. A., et al. 2016, ApJ, 832, 167
Ford, J. M., Demorest, P., & Ransom, S. 2010, Proc. SPIE, 7740, 77400A
Foster, R. S., & Cordes, J. M. 1990, ApJ, 364, 123
Freire, P. C. C., & Tauris, T. M. 2014, MNRAS, 438, L86
Geyer, M., & Karastergiou, A. 2016, MNRAS, 462, 2587
Geyer, M., Karastergiou, A., Kondratiev, V. I., et al. 2017, MNRAS, 470, 2659
Goulding, A. D., Pardo, K., Greene, J. E., et al. 2019, ApJL, 879, L21
Hallinan, G., Ravi, V., Weinreb, S., et al. 2019, BAAS, 51, 255
Harding, A. K., Shinbrot, T., & Cordes, J. M. 1990, ApJ, 353, 588
Hassall, T. E., Stappers, B. W., Hessels, J. W. T., et al. 2012, A&A, 543, A66
Helfand, D. J., Manchester, R. N., & Taylor, J. H. 1975, ApJ, 198, 661
Hobbs, G. 2013, CQGra, 30, 224007
Hobbs, G., Dai, S., Manchester, R. N., et al. 2019, RAA, 19, 020
Hobbs, G., & Edwards, R. 2012, Tempo2: Pulsar Timing Package, Astrophysics Source Code Library, ascl:1210.015
Hobbs, G., Manchester, R. N., Dunning, A., et al. 2020, PASA, 37, e012
Hotan, A. W., van Straten, W., & Manchester, R. N. 2004, PASA, 21, 302
Hunter, J. D. 2007, CSE, 9, 90
Jaffe, A. H., & Backer, D. C. 2003, ApJ, 583, 616
Jiang, L., Li, X.-D., Dey, J., & Dey, M. 2015, ApJ, 807, 41
Jones, M. L., McLaughlin, M. A., Lam, M. T., et al. 2017, ApJ, 841, 125
Joshi, B. C., Arumugasamy, P., Bagchi, M., et al. 2018, JApA, 39, 51
Keith, M. J., Coles, W., Shannon, R. M., et al. 2013, MNRAS, 429, 2161
Kelley, L., Charisi, M., Burke-Spolaor, S., et al. 2019, BAAS, 51, 490
Kerr, M., Reardon, D. J., Hobbs, G., et al. 2020, PASA, 37, e020
Kramer, M., & Champion, D. J. 2013, CQGra, 30, 224009
Kurosawa, N., Kobayashi, H., Maruyama, K., Sugawara, H., & Kobayashi, K. 2001, IEEE Trans. Circuits Syst. I, 48, 261
Lam, M. T. 2017, PyPulse: PSRFITS Handler, Astrophysics Source Code Library, ascl:1706.011
Lam, M. T. 2018, ApJ, 868, 33
Lam, M. T., Cordes, J. M., Chatterjee, S., et al. 2016a, ApJ, 821, 66
Lam, M. T., Cordes, J. M., Chatterjee, S., et al. 2016b, ApJ, 819, 155
Lam, M. T., Cordes, J. M., Chatterjee, S., et al. 2017, ApJ, 834, 35
Lam, M. T., Ellis, J. A., Grillo, G., et al. 2018a, ApJ, 861, 132
Lam, M. T., Lazio, T. J. W., Dolch, T., et al. 2020, ApJ, 892, 89
Lam, M. T., McLaughlin, M. A., Arzoumanian, Z., et al. 2019, ApJ, 872, 193
Lam, M. T., McLaughlin, M. A., Cordes, J. M., Chatterjee, S., & Lazio, T. J. W. 2018b, ApJ, 861, 12

Lee, K. J. 2016, in ASP Conf. Ser. 502, Prospects of Gravitational Wave Detection Using Pulsar Timing Array for Chinese Future Telescopes, ed. L. Qain & D. Li (San Francisco, CA: ASP), 19
Lee, K. J., Bassa, C. G., Janssen, G. H., et al. 2014, MNRAS, 441, 2831
Lentati, L., Alexander, P., & Hobson, M. P. 2013a, arXiv:1312.2403
Lentati, L., Alexander, P., Hobson, M. P., et al. 2013b, PhRvD, 87, 104021
Lentati, L., Alexander, P., Hobson, M. P., et al. 2014, MNRAS, 437, 3004
Lentati, L., Alexander, P., & Hobson, M. P. 2015, MNRAS, 447, 2159
Lentati, L., Kerr, M., Dai, S., et al. 2017a, MNRAS, 468, 1474
Lentati, L., Kerr, M., Dai, S., et al. 2017b, MNRAS, 466, 3706
Levin, L., McLaughlin, M. A., Jones, G., et al. 2016, ApJ, 818, 166
Liu, K., Desvignes, G., Cognard, I., et al. 2014, MNRAS, 443, 3752
Lommen, A. N., & Demorest, P. 2013, CQGra, 30, 224001
Lorimer, D. R., & Kramer, M. 2005, in Handbook of Pulsar Astronomy, ed. R. Ellis et al. (Cambridge: Cambridge Univ. Press)
Luo, J., Ransom, S., Demorest, P., et al. 2019, PINT: High-precision Pulsar Timing Analysis Package, Astrophysics Source Code Library, ascl:1902.007
Luo, J., Ransom, S., Demorest, P., et al. 2020, arXiv:2012.00074
Lynch, R., Brook, P., Chatterjee, S., et al. 2019, BAAS, 51, 461
Maitia, V., Lestrade, J.-F., & Cognard, I. 2003, ApJ, 582, 972
Manchester, R. N. & IPTA 2013, CQGra, 30, 224010
McKinnon, M., Beasley, A., Murphy, E., et al. 2019, BAAS, 51, 81
Mingarelli, C. M. F. 2019, NatAs, 3, 8
Ng, C. 2018, in IAU Symp. 337, Pulsar Astrophysics the Next Fifty Years, ed. P. Weltevrede et al. (Cambridge: Cambridge Univ. Press), 179
Nice, D., Demorest, P., Stairs, I., et al. 2015, Tempo: Pulsar Timing Data Analysis v13.100, Astrophysics Source Code Library, ascl:1509.002
Ocker, S. K., Cordes, J. M., & Chatterjee, S. 2020, ApJ, 897, 124
Osłowski, S., van Straten, W., Demorest, P., & Bailes, M. 2013, MNRAS, 430, 416
Osłowski, S., van Straten, W., Hobbs, G. B., Bailes, M., & Demorest, P. 2011, MNRAS, 418, 1258
Pennucci, T. T. 2015, PhD thesis, University of Virginia, http://libra.virginia.edu/catalog/libra-oa:9384
Pennucci, T. T. 2019, ApJ, 871, 34
Pennucci, T. T., Demorest, P. B., & Ransom, S. M. 2014, ApJ, 790, 93
Pennucci, T. T., Demorest, P. B., & Ransom, S. M. 2016, Pulse Portraiture: Pulsar Timing, Astrophysics Source Code Library, ascl:1606.013
Pennucci, T. T., Possenti, A., Esposito, P., et al. 2015, ApJ, 808, 81
Perera, B. B. P., DeCesar, M. E., Demorest, P. B., et al. 2019, MNRAS, 490, 4666
Phinney, E. S. 2001, arXiv:astro-ph/0108028
Ramachandran, R., Demorest, P., Backer, D. C., Cognard, I., & Lommen, A. 2006, ApJ, 645, 303
Ransom, S., Brazier, A., Chatterjee, S., et al. 2019, BAAS, 51, 195
Rickett, B. J., & Lyne, A. G. 1990, MNRAS, 244, 68
Rosado, P. A., Sesana, A., & Gair, J. 2015, MNRAS, 451, 2417
Shannon, R. M., & Cordes, J. M. 2017, MNRAS, 464, 2075
Shannon, R. M., Lentati, L. T., Kerr, M., et al. 2016, ApJL, 828, L1
Shannon, R. M., Osłowski, S., Dai, S., et al. 2014, MNRAS, 443, 1463
Siemens, X., Ellis, J., Jenet, F., & Romano, J. D. 2013, CQGra, 30, 224015
Siemens, X., Hazboun, J., Baker, P. T., et al. 2019, BAAS, 51, 437
Stinebring, D. R., Chatterjee, S., Clark, S. E., et al. 2019, BAAS, 51, 492
Stovall, K., Freire, P. C. C., Antoniadis, J., et al. 2019, ApJ, 870, 74
Susobhanan, A., Maan, Y., Joshi, B. C., et al. 2020, arXiv:2007.02930
Taylor, J. H. 1992, RSPTA, 341, 117
Taylor, S., Burke-Spolaor, S., Baker, P. T., et al. 2019, BAAS, 51, 336
Taylor, S. R., Vallisneri, M., Ellis, J. A., et al. 2016, ApJL, 819, L6
Torres, D. F., Ji, L., Li, J., et al. 2017, ApJ, 836, 68
Vallisneri, M. 2020, libstempo: Python wrapper for Tempo2 v2.3.5, Astrophysics Source Code Library, ascl:2002.017
Vallisneri, M., & van Haasteren, R. 2017, MNRAS, 466, 4954
van Haasteren, R., & Vallisneri, M. 2014, PhRvD, 90, 104012
van Haasteren, R., & Vallisneri, M. 2015, MNRAS, 446, 1170
van Straten, W. 2006, ApJ, 642, 1004
van Straten, W. 2013, ApJS, 204, 13
van Straten, W., Demorest, P., Khoo, J., et al. 2011, PSRCHIVE: Development Library for the Analysis of Pulsar Astronomical Data, Astrophysics Source Code Library, ascl:1105.014
Verbiest, J. P. W., & Shaifullah, G. M. 2018, CQGra, 35, 133001
Vigeland, S. J., Deller, A. T., Kaplan, D. L., et al. 2018, ApJ, 855, 122